

ShadX Presents:

Chaka

**“A High-performance,
Cost-efficient,
Semi-conventional
Regional Jet Family”**





Mohammad H. Sadraey
Faculty advisor
226897



Mohammadreza Varshavi
Project advisor
1256840



Farid Rassouli
Project advisor
920911



Sam Zavaree
Chief design - Preliminary sizing
1230818



S. Amirreza S. Madani
Team lead - Market analysis
1230788



Mohsen Zahmatkesh
System engineering - S&C - Autonomy
1230786



Erfan Vaezi
Propulsion - CFD
1229626



Amirhossein Mahmoudi
Systems & components - Proposal integration
1241115



Zahra Heydari
Aerodynamics
1230072



Kimia Zahiremami
Cost estimation
1230824



Amirhossein Kariman
Performance analysis - Empennage
1230828



Kasra Eghbali
CAD - Structure - Fuselage
1230823



1 Executive Summary

“Do the impossible, because almost everyone has told me my ideas are merely fantasies.”

-Howard Hughes, pilot and successful businessman

Having experienced a few years of profitability, the worldwide airline industry is on route to being less lucrative. One radical contributor to this proclivity has been the increase in fuel prices and the accompanying unpredictability in this regard. Since the “Scope Clause” has restrained regional airline fleets in the past, and that these fleets will retire in the approaching couple of years, based upon 30-year average lifetime of an airplane, the airlines’ demand for this type of aircraft will have risen by 2030. Moreover, the COVID-19 crisis has shattered future industrial plans, especially in the aviation industry. Having struggled to survive, airlines are obliged to develop new strategies in order to prosper in the forthcoming years.

In response to the 2021 American Institute of Aeronautics and Astronautics (AIAA) graduate team aircraft design Request for Proposal (RFP), we at ShadX have the honor of introducing Chaka¹ Modern Regional Jet (MRJ) family, a novel approach to regional jet (RJ) design and resolving the need for new regional jet aircraft satisfying primarily the 50-seat portion of the market and secondarily the 76-seat portion of the market predicated upon the U.S. domestic “Scope Clause”.

At ShadX, we maintain that the Chaka MRJ family has formidably met the RFP requirements and proved to be the optimal design of the future RJ aircraft thanks to its staggering fuel burn efficiency. Not only has the Chaka-50 manifested to possess 22.32% and 27.07% abatement in fuel burn compared to its foremost current competitive aircraft (the ERJ-145XR) in terms of 500 and 1000 nmi block fuel per seat, respectively, but also the Chaka-76 derivative has demonstrated to have 21.8% and 27.21% less fuel burn compared to its finest competitive aircraft (ERJ170-100AR) in terms of the aforementioned, respectively. That is why the Chaka MRJ family is a promising design, based on systems engineering approach, to play an essential role in resolving the aforesaid quandary. Achieving this, the Chaka-50 had to undergo 4.6% propulsion improvement, 15% empty weight reduction, and 42.8% ameliorated aerodynamic efficiency with respect to its best competitor. For the Chaka-76, the corresponding figures are 8.8%, 12.1%, and 42.8%, respectively. The aerodynamic amelioration observed in the Chaka family stems from the semi-conventional configuration of truss-braced wing, providing prospective customers and passengers with superb attractiveness and prospective manufacturers with Technology Readiness Levels (TRL) fitting for the year 2030.

¹ Chaka is the Persian designation for the “blackpoll warbler”, a bird capable of conducting flights up to 2000 nmi range.

Table of Contents

1	Executive Summary.....	3
2	Abbreviations.....	5
3	Mission Specifications.....	9
4	Database Review	9
5	Market Analysis.....	10
5.1	Market Demand.....	10
5.2	Market Forecast.....	12
6	Systems Engineering	13
6.1	Systems Engineering Approach.....	13
6.2	Configuration Selection	16
6.3	Technology Readiness Level	17
6.4	Reliability.....	19
7	Preliminary Design	20
7.1	Weight Sizing & Mission Profile Analysis 21	
7.2	Matching Chart & Design Point Selection 25	
7.3	Economic Missions	26
7.4	Studying the Optimal Cruise Altitude	29
8	Fuselage Design.....	30
8.1	Determination of Fineness Ratio.....	30
8.2	Seating Arrangement Selection	31
8.3	Conventional Fuselage Assessment	31
8.4	Fuselage Conceptual Design	32
9	Propulsion System	33
9.1	RFP Study	34
9.2	Review of Propulsion Systems.....	34
9.3	Engine Type Selection	35
9.4	Number of Engines Selection.....	36
9.5	Engine Location	36
9.6	Engine Location and Orientation Installation	37
9.7	Fuel Selection.....	38
9.8	Validation of SFC Calculations.....	38
9.9	Available and Future Engines	38
9.10	Engine Conceptual Design	39
9.11	Engine Performance Calculations	40
9.12	Recommendation of engine manufacturer 42	
9.13	Special considerations.....	42
10	Aerodynamics	44
10.1	RFP Study	44
10.2	Airfoil Selection.....	44
10.3	Wing Location.....	46
10.4	Wing Geometry.....	46
10.5	High Lift Devices.....	49
10.6	Drag Polar	50
11	Empennage and Control Surfaces Design.....	52
11.1	Empennage Design.....	52
11.2	Control Surfaces Design	55
12	Weight and Balance.....	55
12.1	Weight of Components	55
12.2	Center of Gravity Calculations.....	56
13	Landing Gear Design.....	62
14	Stability and Control.....	64
14.1	Stability Analysis and Flying Quality	64
14.2	Trim Analysis and 6DOF Simulation.....	68
14.3	Autonomous Operation	70
14.3.1	A Description of the Autonomous System	71
15	Systems and Components	73
15.1	Fuel Systems	73
15.2	Hydraulic Systems	73
15.3	Avionics and Instruments Systems	73
15.4	VFR and IFR Flight Requirements	76
15.4.1	Controlled Airspace.....	76
15.4.2	Uncontrolled Airspace.....	77

15.4.3	Operating Rules and Pilot/Equipment Requirements	77	20.1	Life Cycle Cost	91
15.5	Environmental Control Systems.....	77	20.2	RDT&E Cost.....	92
15.6	Emergency Systems	78	20.3	Manufacturing and Acquisition Cost	92
15.7	Ice & Rain Protection Systems.....	78	20.4	Aircraft Price Estimation.....	93
16	Performance Analysis.....	79	20.5	Operating Cost	93
16.1	Payload Range Diagrams	79	20.5.1	Direct Operating Cost.....	94
16.2	Flight Envelope	80	20.5.2	Fuel Cost	94
16.3	Take-off and Landing Performance	80	20.6	Disposal Cost	95
16.4	Rate of Climb and Ceiling.....	81	REFERENCES		97
16.5	Performance Compliance with FAR Part 25	82			
17	Structures	82			
17.1	V-n Diagrams	83			
17.2	Material Selection	83			
17.3	Structural Design.....	83			
18	Interior Design.....	87			
19	Design Validations	89			
19.1	Validation of the CFD Tools.....	89			
19.2	Validation of FEM Tools	90			
19.3	Validation of Modal tools	91			
20	Cost Analysis.....	91			

Acknowledgements

We at ShadX would like to acknowledge Dr. M. R. Morad and Dr. M. Farahani for their warm-hearted cooperation in providing the required facilities for the team. Also, we would like to express our gratitude to Engineer Parisa Kiani, Bahar Hajipour and also Zahra Shahbazi for their benevolent support.

2 Abbreviations

Symbols

Symbol	Unit	Definition	Symbol	Unit	Definition
AOA	Degree	Angle of Attack	L	lbf	Lift Force
AR	-	Aspect Ratio	L/D	-	Lift-to-Drag Ratio
b	ft	Wingspan	MAC	ft	Mean Aerodynamic Chord
C	ft	Chord	MTOW	lb	Maximum Take-off Weight
C _D	-	Drag Coefficient	Re	-	Reynolds Number
C _{D0}	-	Zero-lift Drag Coefficient	S/S _{ref}	-	Area Ratio
C _f	-	Interference Factor	S _{ref}	ft ²	Wing Reference Area
C _L	-	Lift Coefficient	S _s	in	Landing Gear Strut Length
C _{li}	-	Ideal Lift Coefficient	S _u	ksi	Ultimate Strength
CR	-	Cruise	S _{wet}	ft ²	Wetted Area
cr	-	Critical	SFC	lb/(lbf.h)	Specific Fuel Consumption
D	lbf	Drag Force	t/c	-	Thickness-to-Chord Ratio
d _s	in	Landing Gear Strut Diameter	V	knot	Speed
			W	lb	Weight



Greek Symbols

Symbol	Unit	Definition	Symbol	Unit	Definition
α	Degree	Angle of Attack	ϕ	Degree	Lateral Ground Clearance Angle
δ	Degree	Deflection Angle	ψ	Degree	Lateral Tip-Over Angle
Λ	Degree	Sweep Angle			

Subscripts

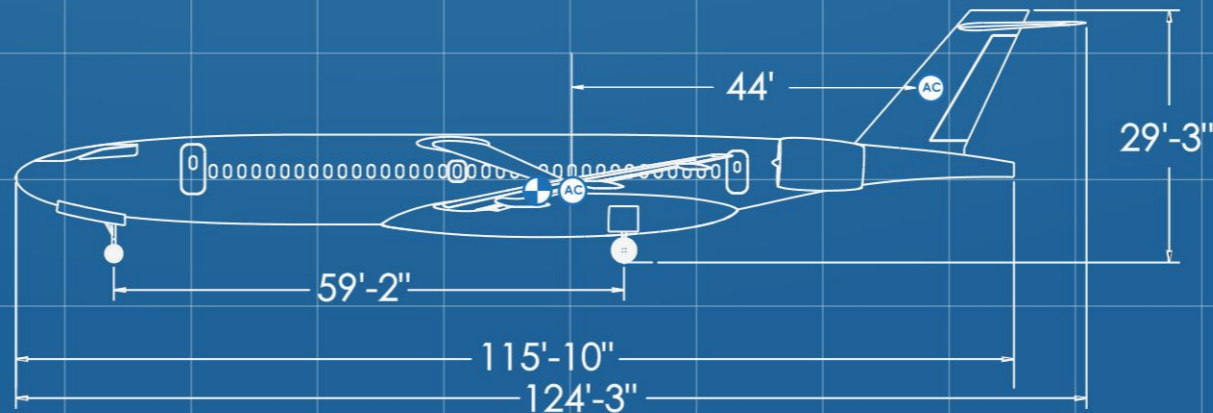
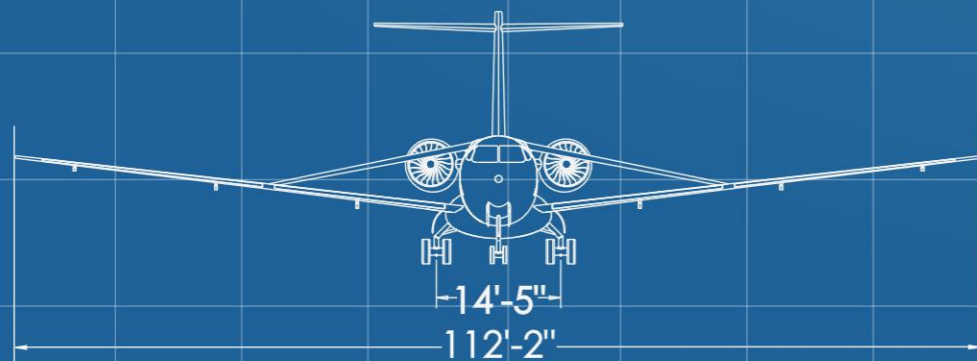
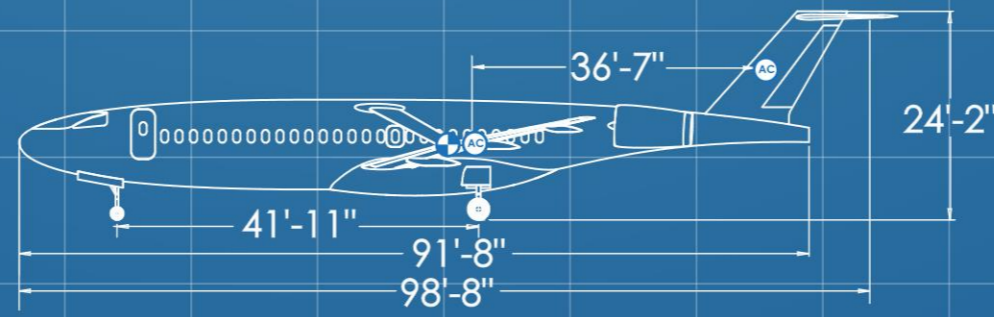
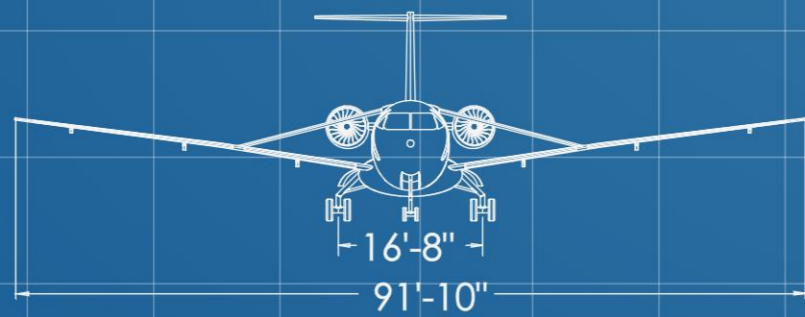
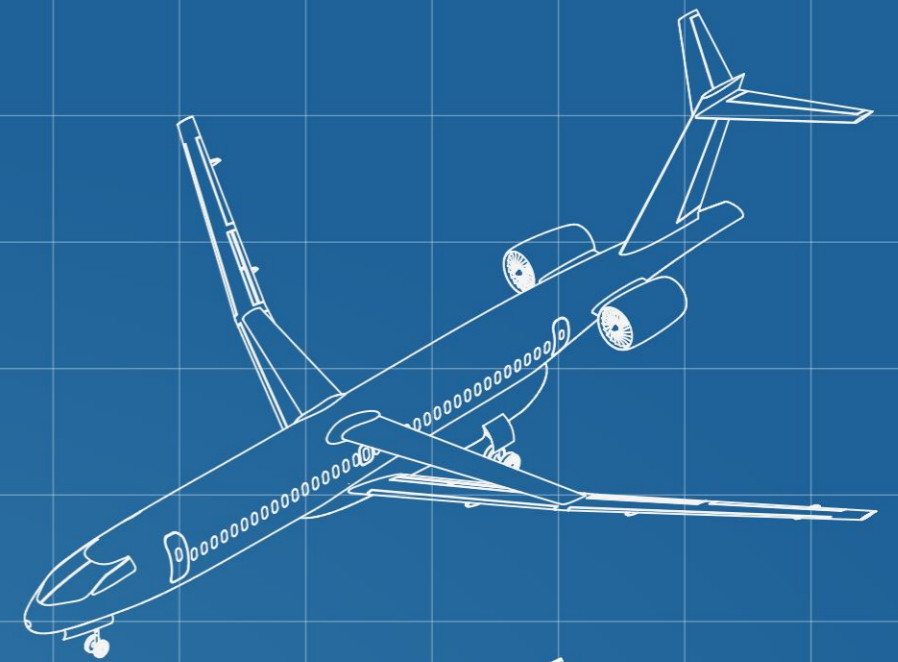
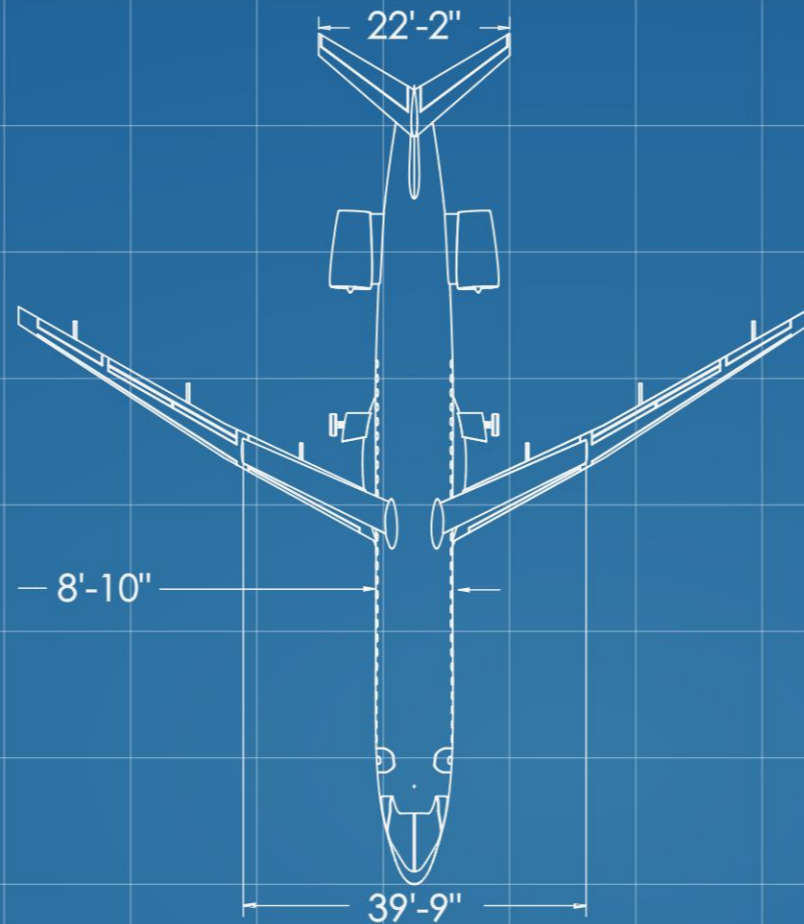
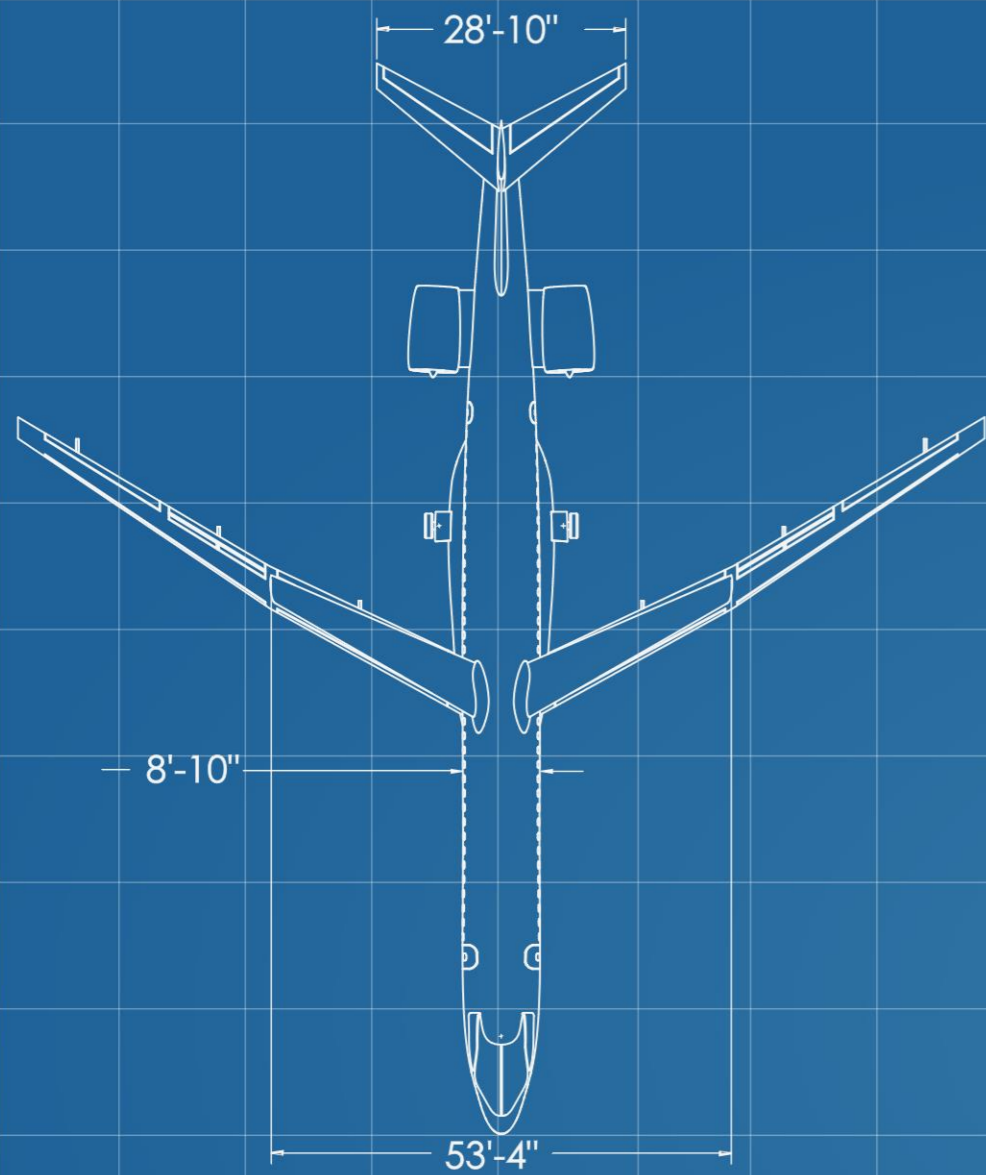
Symbol	Definition	Symbol	Definition
a	Aileron	misc	Miscellaneous
CAT	Category	PL	Payload
com	Component	ref	Reference
e	Elevator	r	Rudder
E	Empty	stall	Stall Condition
F	Fuel	TO	Take-Off
mat	Material	wet	Wetted

Acronyms

Symbol	Definition	Symbol	Definition
AC	Aerodynamic Center	ICAO	International Civil Aviation Organization
ADS-B	Automatic Dependent Surveillance–Broadcast	IECMS	Inflight Engine Condition Monitoring System
AEP	Aircraft Estimated Price	IFR	Instrument Flight Rules
AHRS	Attitude and Heading Reference System	ILS	Instrument Landing System
AMP	Aircraft Mission Planner	IOC	Indirect Operating Cost
APU	Auxiliary Power Unit	IRS	Inertial Reference System
ASTM	American Society for Testing and Materials	L&P	Leakage and Protuberance
ATC	Air Traffic Control	LE	Leading Edge
CAF	Conventional Aviation Fuel	M	Mach Number
CFD	Computational Fluid Dynamics	MHI	Mitsubishi Heavy Industries
CG	Center of Gravity	MLP	Multi-layer Perceptron
ChRJ	Chaka Regional Jet	MRJ	Modern Regional Jet
CPI	Consumer Price Index	MRL	Manufacturing Readiness Level
CRJ	Canadian Regional Jet	PBE	Protective Breathing Equipment
CTC	Company Technology Characteristic	PR	Pressure Ratio
D&R	Disposal and Recycling	PRL	Programing Readiness Level
DOC	Direct Operating Cost	Q	Skin Friction Coefficient
DSM	Design Structure Matrix	RAAS	Runway Awareness and Advisory System
EGPWS	Enhanced Ground Proximity & Warning System	RDT&E	Research, Development, Test and Evaluation
EIS	Entry into Service	RFP	Request for Proposal
EMB	Embraer	RJ	Regional Jet
EoLS	End of Life Solution	ROC	Rate of Climb
ERJ	Embraer Regional Jet	ROS	Robot Operating System
FEM	Finite Element Method	RPK	Revenue Passenger Kilometers
FF	Form Factor	RVSM	Reduced Vertical Separation Minimum
FMS	Flight Management System	S&C	Stability & Control
GDP	Gross Domestic Product	SAF	Sustainable Aviation Fuel
GE	General Electric	SC	Super-Critical
GPWS	Ground Proximity & Warning System	TAWS	Terrain Avoidance and Warning System
GS	Guidance System	TCAS	Traffic Collision Avoidance System
GTP	Global Traffic Planner	TCAS/ ACAS	Traffic/Airborne Collision Avoidance Systems
HGS	Head-up Guidance System	TE	Trailing Edge
HLD	High-lift Device	TRL	Technology Readiness Level
IATA	International Air Transport Association	VFR	Visual Flight Rules



Description	Requirement		Compliance	
	50 Pax	76 Pax	Chaka-50	Chaka-76
Cruise Mach Number	0.78 – 0.8	0.78 – 0.8	0.8	0.8
Range	2000 nmi	At least 1500 nmi	2251 nmi	2251 nmi
Cruise Ceiling	At least FL320	Not mentioned	FL350	FL350
Maximum Take-off Field Length	4000 ft	6000 ft	3824.8 ft @ FL50 + 18°F 3721.6 ft @ Sea lvl + 18°F	5150.7 ft @ FL50 + 18°F 5064.2 ft @ Sea lvl + 18°F
Maximum Landing Field Length	4000 ft	6000 ft	3966.2 ft @ FL50 + 18°F 3769.4 ft @ Sea lvl + 18°F	5588.5 ft @ FL50 + 18°F 5209.7 ft @ Sea lvl + 18°F
Maximum Wingspan	24 m or 36 m	24 m or 36 m	28 m	34.2 m
Climb Gradient	CFR 25.121	CFR 25.121	2.88 % - 12%	2.88% - 12%
Approach Speed	<141 knots	<141 knots	139.72 knots	134.88 knots
Fuel Burn Reduction In 500 nmi	At least 20%	Not mentioned	22.32 %	21.8 %
Fuel Burn Reduction In 1000 nmi	Not mentioned	Not mentioned	27.07 %	27.21 %
Seat Width	17.2"-18"	17.2"-18"	18"	18"
Aisle Width	18"	18"	20"	20"
Seat Pitch	30"	30"	30"	30"
Baggage (50/76 pax)	2000 lb 250 ft ³	3040 lb 380 ft ³	Bag = 1500 lb, 187.5 ft ³ Carry on = 500 lb, 62.5 ft ³	Bag = 2280 lb, 285 ft ³ Carry on = 760 lb, 95 ft ³



**CHAKA MRJ FAMILY
TECHNICAL SKETCH**



3 Mission Specifications

As it has been prognosticated by the industry that there will be demand for as many as 2,000 new regional aircraft in the following 20 years, the RFP has put forward the opportunity to develop a modern regional jet family, comprising a 50-seat RJ and a 76-seat stretch derivative of the aforementioned. The principal objective, for the 50-seat RJ, is to enjoy ameliorated fuel burn efficiency of at least 20% compared to the existing 50-seat RJs, in terms of 500 nmi block fuel per seat, with a comparable cost to build.

Table 1- Mission specifications

RFP	50-seat	76-seat
Entry Into Service (EIS)	2030	2031
Passenger capacity	50 +0/-4	76 +0/-4
Design range with full passengers	2000 nmi	At least 1500 nmi
Cruise Mach number	Minimum: 0.78, Target: 0.8	
Seat Width	Minimum: 17.2", Target: 18"	
Aisle width	Minimum: 18"	
Wingspan	Objective: Maximum of ICAO Code B Requirement: Maximum of ICAO Code C	
Approach speed	Category C (<141 knots)	
Maximum takeoff field length	4,000' over a 50' obstacle	6,000' over a 50' obstacle
Maximum landing field length	4,000' over a 50' obstacle	6,000' over a 50' obstacle
Distance to climb up to initial cruising altitude	Less than 200 nmi	Not mentioned
Initial cruising altitude	At least FL320	Not mentioned

Design Objectives:

- Maximizing structural and systems commonality between the 50- and 76-seat aircraft in order to minimize the development and production cost
- Making the aircraft visually appealing, so it will be marketable, and identifying what features are essential to the operators for different missions
- Making the aircraft's reliability equal to or better than that of comparable aircraft
- Making the aircraft maintenance equal to or better than that of comparable aircraft

4 Database Review

Embraer ERJ-145: ERJ-145 is a regional jet produced by the Brazilian aerospace company Embraer. The 45–48 seat EMB145 was launched in 1989 as a turboprop-powered stretch derivative of the EMB 120 Brasília turboprop. The ERJ-145 family of aircraft, by and large, comes equipped with two Rolls-Royce AE 3007 series turbofan engines.



Bombardier CRJ200: CRJ200 is a RJ designed and manufactured by Bombardier Aerospace between 1991 and 2006, the first of the Bombardier CRJ family. It is identical to the CRJ100 except for its engines, which were upgraded to the CF34-3B1 model, offering improved efficiency.

Embraer E-170: E-170 is a narrow-body short- to medium-range twin-engine jet carrying 66 to 78 passengers, manufactured by the Embraer. E-170 is the smallest aircraft in the E-Jet family and was the first to have entered revenue service by March 2004. It is powered by CF34-8E engines of each delivering 14,200 lbf of thrust.

Bombardier CRJ700: CRJ700 is a RJ airliner designed by the Bombardier and is a part of the CRJ aircraft family; The CRJ700 is a stretch derivative of the CRJ200. The CRJ700 features a new wing with leading-edge slats and a stretched and slightly widened fuselage, comprising a lowered floor.

Mitsubishi M100: M100 is a regional jet developed by the Mitsubishi Aircraft Corporation (MAC), a Mitsubishi Heavy Industries (MHI) subsidiary. The low-wing twinjet is powered by two underwing Pratt & Whitney PW1000Gs and was the first program to have selected the geared turbofan.

Table 2- Database review matrix, including RFP requirements

Parameter	50-seat			76-seat		
	ERJ-145 XR	CRJ200 LR	RFP Requirement	E-170 100AR	CRJ700 LR	RFP Requirement
Passenger Capacity	50	50	50 +0/-4 @30"	72-78 @30-33"	66 to 78	76 +0/-4 @30"
Range with full PAX	2,000 nmi	1,700 nmi	2,000 nmi	2,100 nmi	2,037 nmi	At least 1,500 nmi
Cruise Mach Number	Mach 0.8	Mach 0.74	Target Mach 0.8	Mach 0.75	Mach 0.78	Target Mach 0.8
Wingspan	21.00 m	21.21 m	[R] Maximum of ICAO Code C	26.00 m	25.84 m	[R] Maximum of ICAO Code C
Maximum takeoff field length	6,854 ft	6,290 ft	4,000 ft over a 50' obstacle	5,394 ft	6,380 ft	6,000 ft over a 50' obstacle
Maximum landing field length	4,692 ft	4,850 ft	4,000 ft over a 50' obstacle	4,072 ft	5,325 ft	6,000 ft over a 50' obstacle
MTOW	53,131 lb	53,000 lb	-	85,098 lb	75,000 lb	-
Empty Weight	27,734 lb	29,195 lb	-	46,572 lb	47,250 lb	-
Fuel Weight	13,298 lb	14,305 lb	-	20,580 lb	19,450 lb	-
Payload Weight	13,051 lb	13,500 lb	12,000 lb	21,550 lb	18,800 lb	18,240 lb

5 Market Analysis

In every successful industrial project, the first step to be taken into consideration is the recognition of market demand. Coming up with a business plan for the future is the second measure to be taken into account.

5.1 Market Demand

The first step toward studying the 50- and the 76-seat regional jet market is going through the manufacturers' delivery data of the purchased aircraft. Using [1] databases, in accordance with the RFP's request for meeting the Scope Clause, the aircraft listed in Table 3 were selected in order to study the market of 50- and 76-seat regional jets.



Table 3- Selected Regional Jets to study the market

50-seat	76-seat
Embraer E145	Embraer E170
Bombardier CRJ100/200	Bombardier CRJ700

According to Figure 1, from 1991 through 2001, regional airlines demonstrated a marked tendency toward buying 50- and 76-seat regional jets; the aforementioned experienced a downward trend from 2001 to 2021. In recent years, the market has witnessed the lack of desire for ordering 50- and 76-seat regional jets. The pilot shortage in the Scope Clause area and the rules imposed on airlines by the Scope Clause, severely confining the regional jet fleets, constitute the underlying disrelish observed in airlines.

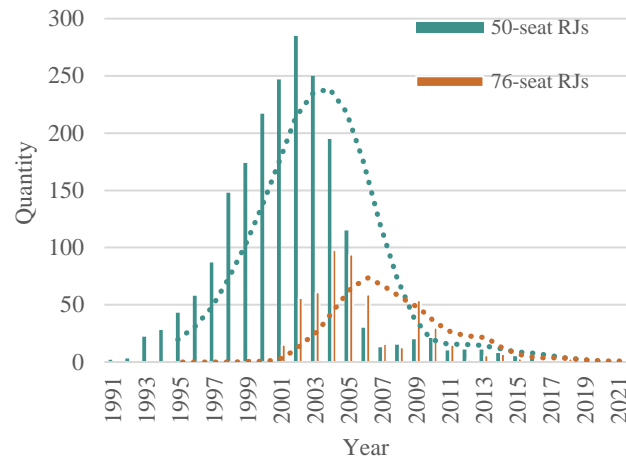


Figure 1- 50- and 76-seat RJ Deliveries in terms of quantity and moving average since 1991

Since the Scope Clause has limited regional airline fleets and that the fleets will be retired in the approaching couple of years, based upon 30-year average lifetime of an airplane, the airlines’ demand for this aircraft category will have risen by 2030. The RFP has also mentioned that, by 2040, the market will have required as many as 2,000 regional jet aircraft. Therefore, the demand for regional aircraft will continue growing during the next 20 years.

Another vital measure to be taken in terms of market analysis is customer recognition. Table 4 illustrates major regional jet customers.

Table 4- Major regional jet fleet customers in the North America

Airline	37-49 Seat	50 Seat		76 Seat		77-124 Seat		Total
	ERJ-135	ERJ-145	CRJ-200	ERJ-170	CRJ-700	ERJ-175	CRJ-900	
American Eagle	7	115	-	-	127	184	126	559
United Express	-	65	193	38	-	194	-	490
Delta Connection	-	-	82	22	24	112	164	404
SkyWest Airlines	-	-	211	-	116	193	44	564
Republic Airlines	-	-	-	62	-	161	-	223

As shown in Figure 2, having experienced a few years of profitability, the worldwide airline industry is on route to being less lucrative. In the North America, since a peak presented in 2017, the margins are systematically falling [2]. One major contributor to this has been the increase in fuel price and its unpredictability. At this point, Chaka regional jets can play an essential role in resolving the aforesaid quandary, as they are remarkably more fuel-efficient.

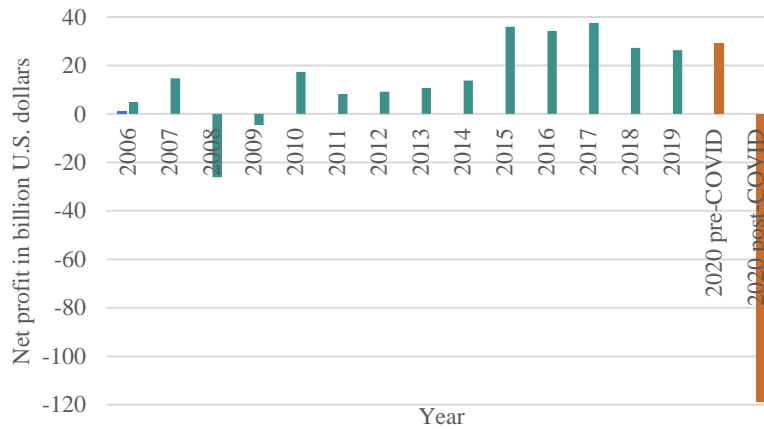


Figure 2 Net profit gained by worldwide commercial airlines, 2006-2020

The COVID-19 crisis has obliterated future industrial plans, especially in the aviation industry. Having struggled to survive, airlines are obliged to develop new strategies in order to thrive in the coming years

According to Embraer [3], only by 2024 are RPKs expected to have returned to levels observed in 2019. Domestic traffic will bounce back about a year prior to international traffic. RPKs will grow at a rate of 2.6% a year on average over the next decade, leading into a 19% reduction in the overall volume by the end of the period.

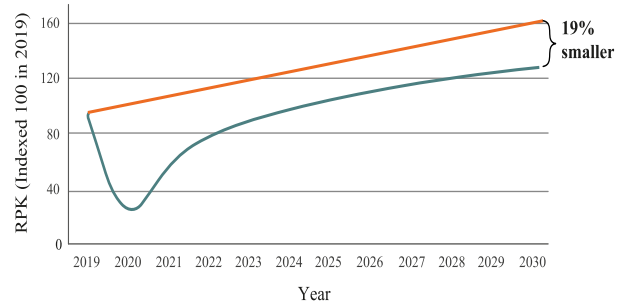


Figure 3- RPK growth projection, Reproduced from [3]

Due to sedate growth experienced through the next decade, offering cost-efficient multi-mission aircraft will be in airlines' best interest. A fleet of versatile, small, narrow-body jets is an optimal solution. Cost-efficient aircraft generating higher profits, such as the Chaka RJ family, are preferable to long- and short-haul missions conducted by mainline and regional airlines. Not only will the Chaka regional jets be more fuel-efficient than their antecedents, but also they will possess operational cost merits. That is because they can reach 10-35% less flight crew pay costs in comparison with mid-size narrow bodies [2].

5.2 Market Forecast

Owing to the lack of economic data until 2050, in order for the market performance of Chaka to be forecast, deep learning is exploited as a principal methodology to assess the economic and financial factors [4]. For the aforementioned to be implemented, market performance ought to be defined as a time series problem with the purpose of deducing market trends based upon relevant inputs [5]. Several parameters could affect the airlines' demand for new aircraft. Some of the essentials, in this regard, are the world's RPK and GDP per capita, USA's GDP per capita, PAX Load Factor, global crisis, and total passengers traveling by airplanes during a year. The data covering the



interval between the years 1997 and 2020, in Figure 4, has been obtained from [6]. It can be observed that, due to the COVID-19 global crisis, the growth rate of the airline market is 19% behind that of the pre-COVID-19 [3], and the market will commence its stable trend from 2024. At this point, the future tendency from 2021 through 2050 could be prophesied, as shown in Figure 5.

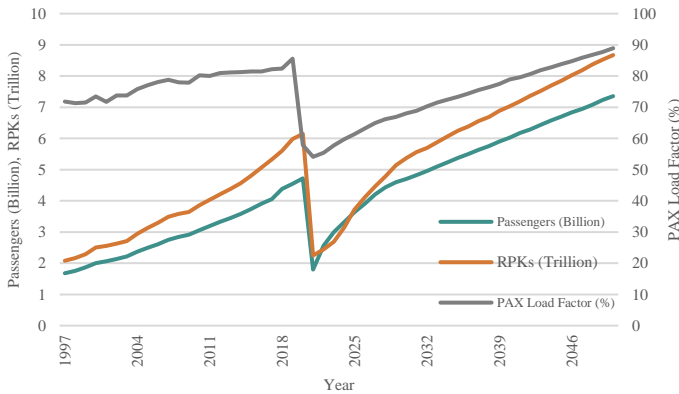


Figure 4- Number of Passengers, RPKs, and PAX Load Factor from 1997 through 2050

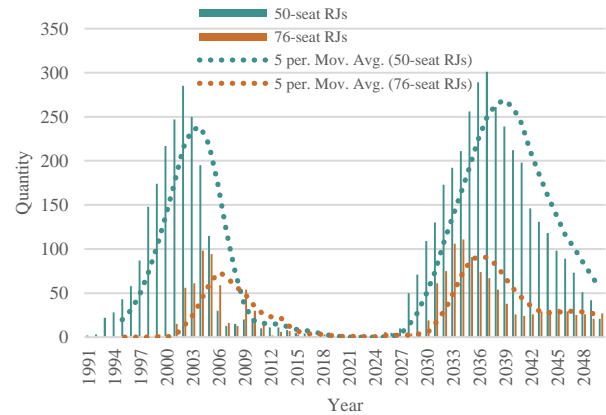


Figure 5- Observed and conjectured trend of 50- and 76-seat RJ deliveries, having assumed continuation of the Scope Clause until 2050

Assuming that the Chaka MRJ family could dominate 50% of the RJ Market, Table 5 provides information about the entire production plan of the Chaka MRJ family as well as its average production rate per month.

Table 5- Chaka MRJ family production plan

Aircraft type	Total production plan	APR (per month)
Chaka-50	1670	6.62
Chaka-76	486	2.03

6 Systems Engineering

In every design process, one of the most crucial design stages to be pursued is the conceptual design phase. In this phase, taking into account design changes and corresponding impacts of aforementioned on the system’s components is of paramount importance. Minor and organized changes will result in further reductions in terms of development and design costs. The project’s DSM, exploited in the overall design procedure, has been presented in this section, including the team’s structure, communication, activities, and design patterns.

6.1 Systems Engineering Approach

The approach is in charge of conducting Work Breakdown Structure (WBS), determining the direction of the project and its development accompanied by monitoring communication and integrating the overall plan. The discipline is also responsible for leading the project in terms of configuration analysis and selection, technology level



assessment, and design risk determination. The principal activities this group is concerned with are comprised of the following:

- 1- Determination of interrelations and design patterns
- 2- Opting for the operational design concept
- 3- Analyzing the design reliability and technology
- 4- Breaking down of the system into subsystems

The Design Structure Matrix is an organized, networked methodology used so as to identify the pivotal elements of the design process and the interrelations existent in between [7]. Various forms of the matrix are exploited to interrelate sub-design teams, design parameters, design activities, and physical elements. In this project, the DSM matrix pertinent to design activities has been utilized.

In general, this matrix is a square, and any marks outside of its main diameter indicates a connection between the two elements. One of the merits of utilizing the DSM is the finer understanding of the system and its components. The other advantage is the possibility of clustering the components which possess more interrelations in between them.

The required design activities were excerpted from the RFP, and, afterward, they were divided into 33 different classifications, placed in the rows and columns of the DSM. Subsequently, the connections between every single classification and the others were examined, marking the relationship every time there was any. In the next step, utilizing an innovative optimization algorithm, the team transformed the matrix into a lower triangular one so that independent activities could be placed on top of the matrix and paid attention to at the beginning of the design procedure. In this manner, the activities located on lower rows could utilize the outputs of those independent activities as their inputs [8]. Table 6 provides an overview of the DSM utilized in this project.

Chaka Regional Jet Design Structure Matrix





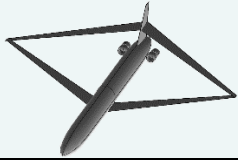
Task	#	1	2	3	4	5	6	7	8	9	10	11	12	13	14	15	16	17	18	19	20	21	22	23	24	25	26	27	28	29	30	31	32	33				
Market analysis, Customer demand	1	•																																				
Technology Readiness Level	2	•	•																																			
Mission profile	3	•		•																																		
Configuration selection matrix and concept selection	4		•	•	•																																	
Evaluation of standards in terms of mission profile	5		•			•																																
Estimation of the MTOW and sensitivity factors	6		•		•		•									•	•																					
Estimation of the aircraft's C_{D_0} and $C_{L_{max}}$	7				•		•	•																														
Calculation of S_{ref} and engine thrust	8					•	•	•	•																													
Preliminary design review	9		•		•	•		•	•	•		•				•					•		•															
Analysis and selection of the aerodynamic configuration	10		•	•	•		•	•	•	•	•		•																									
Aircraft performance analysis	11			•			•	•	•	•		•													•													
Engine selection matrix and analysis	12											•	•																									
Analysis and selection of subsystems germane to the engines	13												•	•																								
First evaluation of the components' weights and their disposition	14						•				•		•	•	•							•																
CAD, calculations in terms of CG and moment of inertia	15									•	•		•	•	•	•																						
Analysis of propulsion system's performance in the mission profile	16			•								•	•				•																					
Selection and analysis of control system	17					•				•					•	•					•	•																
Compatibility of propulsion with structures and aerodynamics	18							•		•			•	•	•	•				•	•	•	•															
Maintainability	19												•	•	•	•				•	•	•	•															
CFD	20			•						•	•	•	•	•	•	•				•	•	•	•	•														
Stability analysis and trim diagram	21									•							•	•	•		•	•	•	•														
Material selection and structural analysis	22		•							•	•		•	•	•	•				•	•	•	•	•														
Aircraft weight of components breakdown matrix	23											•	•	•	•	•				•	•	•	•	•														
6 DOF Simulation	24											•					•					•	•	•	•													
Weight and balance charts	25					•																•	•	•	•													
Flight envelope and V-n diagram	26			•								•					•				•	•	•	•														
Autonomous flight system	27			•		•																•	•	•	•													
Flight quality analysis	28					•						•					•	•			•	•	•	•														
Performance analysis in VFR, IFR, and Icing conditions	29		•							•	•		•				•	•																				
Reliability	30			•		•				•	•		•							•	•		•	•														
Safety management system	31									•		•	•	•						•	•	•		•														
Cost estimation	32	•	•							•	•									•	•		•	•														
Disposal plan	33		•		•							•	•							•	•		•	•														

Table 6 The DSM used for Chaka aircraft design

6.2 Configuration Selection

In this section, based upon RFP requirements, according to Table 7, the advantages and disadvantages of the selected configurations are studied [9-19].

Table 7- Configuration trade-off study matrix

	Configuration	Advantages	Disadvantages
Conventional		<ul style="list-style-type: none"> - High TRL - Low R&D cost - High maintenance capability - Certification convenience 	<ul style="list-style-type: none"> - Heavy wing - Low L/D - High fuel consumption - Increased possibility of engine FOD
Hybrid wing-body		<ul style="list-style-type: none"> - High L/D - Low fuel consumption - Landing gear convenient placement - Decreased possibility of engine FOD 	<ul style="list-style-type: none"> - High R&D cost - High maintenance cost - Low stability - Passenger discomfort - Low TRL
Truss-braced wing		<ul style="list-style-type: none"> - High AR and L/D - Low induced drag - Similarity to the conventional configuration in terms of TRL and R&D cost - High lateral stability 	<ul style="list-style-type: none"> - Decreased rigidity of the wing's structure - Difficult engine and landing gear placement
Double bubble		<ul style="list-style-type: none"> - Increased cabin capacity - Increased body lift - Decreased wing weight due to landing gear placement in the fuselage - Efficient passenger embarking and disembarking 	<ul style="list-style-type: none"> - Low fuselage TRL & MRL - Low controllability - Suitable for freighter aircraft due to cabin pressurization difficulties - Increased stress on the engines
Joined wing		<ul style="list-style-type: none"> - Low induced drag - High L/D - High CG excursion (High longitudinal Controllability) 	<ul style="list-style-type: none"> - High interference drag - Low wing MRL - Low wing maintenance

The configuration selection matrix is one of the conventional tools for decision-making in terms of aircraft configuration. Therefore, this matrix is formed, and its evaluation criteria are determined according to the RFP requirements. Then, the significance of each criterion is rated using a number between 0 and 10, and, lastly, for every single configuration, the importance of each criterion is scored, using the same figures. The team could prioritize each configuration in terms of undergoing careful study.

According to Table 8 and the RFP requirements, the Conventional aircraft received the highest score and is the priority of analysis. Thanks to RFP requirements, the “Low Fuel Consumption” and “Low Cost to Design and Develop” evaluation criteria play major roles in terms of decision making and have the score of 10.



Table 8- Configuration selection matrix

Factor	Significance	Conventional	Truss-braced wing	Hybrid wing-body	Double bubble	Joined wing
Low fuel consumption	10	5	8	9.6	6.8	6.2
TRL	6.4	10	7.4	6.6	6.4	3.8
How common is it?	2	10	4	4.8	3	1.6
R&D cost	10	9.4	7	4	5.4	4.8
Maintainability	7	6.8	6	4	6	4.4
Appearance	6.5	4.4	5.6	8.2	3.2	5
Noise and environmental pollution	6	5.4	8	8	6.2	7
Total score	-	336.6	331.76	317.14	268.96	242.82
Ranking	-	1	2	3	4	5

It is also observed that the Truss-braced configuration has gained close score when compared to the conventional configuration. Therefore, considering all the upsides and downsides collectively and neglecting criteria such as being exquisitely attractive, the Truss-braced wing configuration will be implemented.

6.3 Technology Readiness Level

In order to analyze the proposed design technology, the parameter TRL has been used as an accepted criterion for assessing the level of technological readiness. According to such criterion, each system or subsystem, in terms of technology readiness, receives a value between 1 to 9, as defined in Table 9. The average excess cost to be undergone, using each level of technology, has also been specified, indicating a decrease in cost as the TRL increases.

Table 9- Definitions of technology readiness levels (TRLs)

TRL Level	Definition	Cost
1	Basic principles are observed and reported.	> 25%
2	The technology concept and/or application is formulated.	> 25%
3	Essential functions are studied analytically or experimentally.	20-25%
4	Components or subsystems are validated in the laboratory.	15-20%
5	Components or breadboards are validated in the appropriate environment.	10-15%
6	Systems or subsystems' performance is established in the relevant environment.	< 10%
7	The prototype's performance is proven in the operational environment.	< 10%
8	Completing the actual system, proving performance, and verifying quality by performing tests.	< 5%
9	The system's performance is finally proved during a real mission.	0%

In the following, the manufacturing readiness level of each design is examined. This criterion demonstrates the level of being ready and capable in terms of manufacturing a design. A summary of the MRLs is given in Table 10.

Table 10- Definitions of manufacturing readiness levels (MRLs)

MRL Level	Definition	Min. TRL Level
1	Concepts and the possibility of basic production at a high level are identified.	-
2	Manufacturing concepts are applied, and concepts' abilities to meet requirements are studied.	-



3	The possibility of making production concepts in the laboratory is evaluated.	-
4	The ability to produce the technology in the laboratory is studied, and the equipment and materials required for production are determined.	TRL 4
5	The ability to produce prototype components in the production environment is studied, and safety management systems are reviewed.	-
6	The capability to produce a prototype system or subsystem in the production environment, with the probability of some future corrections, is studied.	TRL 6
7	The ability to produce a system, subsystem, or component of the prototype in an environment close to production is studied. Also, detailed design is finished, and productivity is evaluated.	On the way to TRL 7
8	Production line capability to produce early prototypes at a low rate is tested.	TRL 9
9	A high rate of production is achieved. All engineering, performance, quality, and reliability requirements are met.	TRL 9

In this project, the NASA TRL Calculator Microcode [20], in Excel, has been exploited in order to calculate the TRL for various configuration technologies. The microcode is a checklist that calculates the TRL value by specifying the percentage of progress. To calculate the TRL at a system level, firstly, the TRL of each subsystem is to be determined. Then, the lowest level of system technology is expressed as the system’s TRL. Figure 6 provides an illustration of completed tables in terms of TRL calculations for a conventional configuration.

Figure 6- A sample of performed TRL calculations for the conventional configuration

As shown in Figure 6, the calculations related to technology, manufacturing, and programming readiness levels are performed simultaneously. These calculations refer to the hardware and software issues of the design. It is assumed that the designer wants to reach TRL 9, for which they select the highest option available in the “Top Level View”. Table 11 shows results of TRL, MRL, and PRL calculations for the three candidate configurations. According to Table 8, the TRL, MRL, and PRL of the three configurations receiving the highest scores are calculated and compared.

Table 11- Results of TRL, MRL, and PRL calculations for three candidate configurations

Configuration	TRL	MRL	PRL
Conventional	9	9	9
Hybrid-wing body	3	3	3
Truss-braced wing body	8	7	8



As can be seen, for the conventional configuration, the technology, production, and planning capabilities are at the highest level; however, using this configuration, in practice, will make it impossible to achieve RFP requirements. Therefore, further calculations with respect to this layout are disregarded.

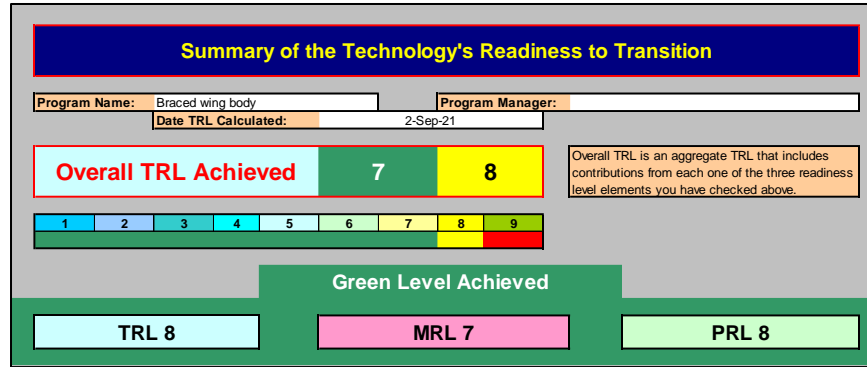


Figure 7- A sample of performed TRL calculations for the Truss-braced wing configuration

As shown in Figure 7, the readiness level, as regards technology and planning, of the Truss-braced wing configuration is at level 8, also the MRL of the configuration is at level 7. This difference is due to the fact that parts of the wing and fuselage need to be modified in comparison with the conventional aircraft production line. The team is convinced that these levels of Truss-braced wing configuration is at acceptable level according to EIS stated in RFP.

6.4 Reliability

Fault Tree Analysis (FTA) is one of the most practical approaches in terms of systems reliability analysis. The fault tree is a graphical model comprising a combination of serial and parallel defects causing a predefined final event to occur. Figure 8 provides an overview of the fault tree concerning this project.

It is worthwhile mentioning that the tree is presented at a system level, and, as can be seen, from the operational vantage point, six principal modes of fault have been determined, namely:

1. Start and warm-up
2. Take-off
3. Flight altitude
4. Flight range
5. Cruise speed
6. Landing

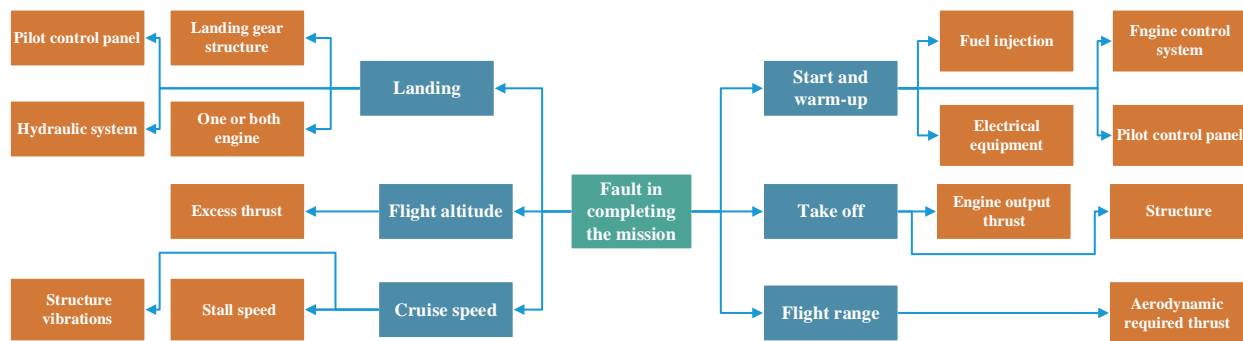


Figure 8- Fault Tree analysis of the project



According to Figure 8, events leading to faults, from a functional point of view, are determined. Given that the fault tree is a tool used to calculate risk and exercise reliability, following the project, it would be necessary that the probability associated with each fault be identified—the aforementioned required specialized meetings with the design teams as well as industry experts, as shown in Table 12.

Table 12- Risk assessment

Mission Hazards	Severity	Likely hood	Risk Mitigation	Severity	Likely hood
One engine failure	Low	Moderate	Redundant engine	Low	Low
two engine failure	High	Very low	Gliding	Moderate	Very low
Electrical system failure	Moderate	Low	APU	Low	Low
Landing gear failure	High	Low	Airport emergency equipment	Moderate	Low
Hydraulic system failure	Moderate	Low	Redundant system and fly-by-wiring	Very low	low
Bird Strike	Moderate	Low	Airport equipment	Low	Low
Mid-air collision	Extreme	Very low	ATC and ADSP	Low	Very low

7 Preliminary Design

Following through the systems engineering approach, in which an airplane is designed during three predominant phases, namely conceptual design, preliminary design, and detail design, the preliminary design phase of Chaka MRJ family has been carried out based upon a systematic calculation procedure. There will be three principal parameters of the two airplanes to be determined during this phase, scilicet MTOW, S_{ref} , and engine thrust. Needless to say, some other pivotal parameters such as the airplanes' C_{D0} , C_{Lmax} etc. will be established in the process. In order for the wing reference area and engine thrust to be determined, the technique utilized is referred to as “matching chart” methodology. It is worth mentioning that the methodology and equations exploited in calculations are all based upon [21, 22]. Figure 9 represents the overall road map followed in this phase.

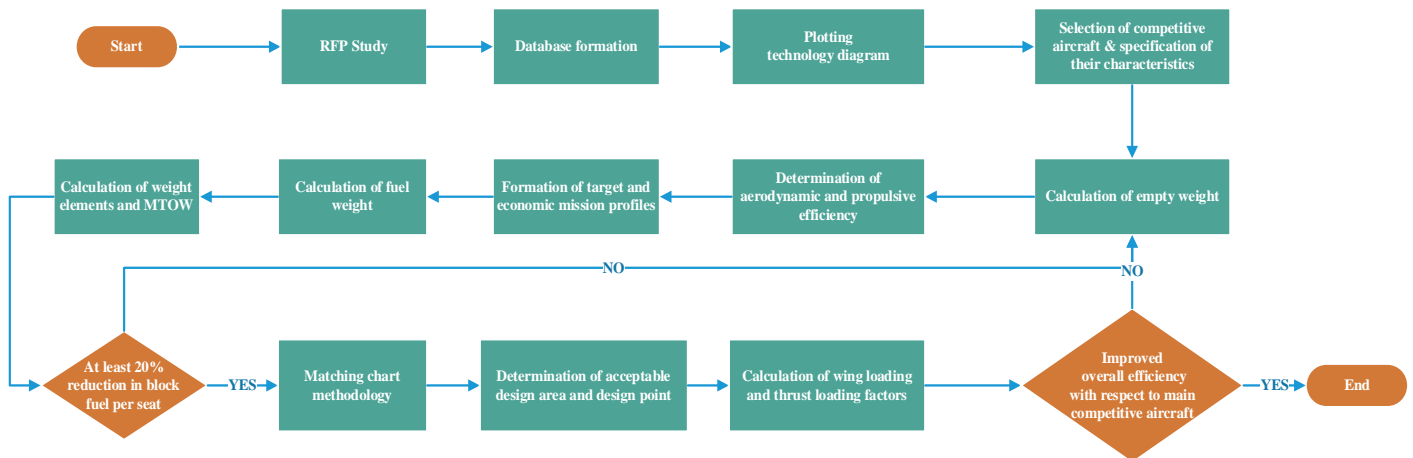


Figure 9- Preliminary design phase road map



7.1 Weight Sizing & Mission Profile Analysis

The technique utilized in order to estimate the MTOW is predicated upon past history as the primary source of information. Nonetheless, after having concluded the first design loop in which all airplane components have been thoroughly designed, and their geometry, dimensions, and the density of the materials from which they are manufactured are known, the team calculates the airplanes' weights using more accurate techniques. Considering the iterative nature of aircraft design, the general design team travels the loop several times until the discrepancy between the two figures is lower than 3%. It is worthwhile mentioning that the figures demonstrated in the following are the outcome of such an iterative process. The overall take-off weight is comprised of the following constituents:

- Payload weight (W_{PL})
- Fuel weight (W_F)
- Trapped fuel and oil weight (W_{TFO})
- Crew weight (W_C)
- Empty weight (W_E)

Some of these constituents hinge upon statistics; others are established using performance equations. Payload and crew weight are determined using the data provided by the RFP. They are not dependent upon the airplane's all-up weight. Quite the contrary, the other three components are functions of the airplane's all-up weight, and, in this regard, they will mostly be considered as fractions of the airplane's MTOW during the calculation procedure. Equation 1 is used to ascertain the MTOW of the airplane.

$$\text{Equation 1: } W_{TO} = W_{PL} + W_{Crew} + W_F + W_E + W_{TFO}$$

As regards the payload weight, in accordance with the RFP, for the 50-seat and 76-seat airplanes, respectively, 50 and 76 passengers of each weighing 200 lb accompanied by 40 lb of baggage weight are taken into consideration.

In terms of the crew weight, in accordance with the RFP, for the 50-seat and 76-seat airplanes, two pilots and one cabin crew member, and two pilots and two cabin crew members are considered respectively, with each having a weight of 190 lb accompanied by 30 lb of baggage weight. Regarding determination of the fuel weight, the first step is to define the preponderant mission profile of the two airplanes. According to market analyses conducted [23], taking into account the U.S. airports possessing large quantities of passengers as well as flight routes for which airline companies are fiercely competitive, several routes complying with the RFP were chosen. Having concluded that the domestic market of the future requires multi-mission airplanes capable of performing well over the gamut of 500, 1000, and 2000 nmi missions, the market team downselected the following mission profiles. Of the four mission profiles, 3 of them are 1-legged and one of them is 2-legged. Table 13 and Figures 10-13 delineate the aforementioned.



Table 13- Final downselected mission profiles

#	Mission type	Route	From	To	Range (nmi)
1	2-legged (2000 nmi)	LAX to ORD	Los Angeles	Chicago O'Hare	1516 + 637 = 2153
		ORD to LGA	Chicago O'Hare	New York LaGuardia	
2	1-legged (2000 nmi)	JFK to LAX	New York JFK	Los Angeles	2151
3	1-legged (1000 nmi)	DFW to LAX	Dallas/Fort Worth	Los Angeles	1073
4	1-legged (500 nmi)	ATL to FLL	Atlanta	Fort Lauderdale/Hollywood	505



Figure 10- The 2-legged 2000 nmi mission profile



Figure 11- The 1-legged 2000 nmi mission profile



Figure 12- The 1-legged 1000 nmi mission profile



Figure 13- The 1-legged 500 nmi mission profile

In mission profiles like the ones shown above, the main feature of the flight is the cruise segment measured by the performance parameter of range. For the analysis to be carried out, the airplanes' weights at each mission segment are numbered. In order to estimate the weight fractions pertaining to the airplanes' weight at the end of flight operation over their initial weight (M_{ff}), weight fractions for each segment are ascertained and subsequently multiplied by one another. The following principal equation is used to find the overall fuel weight.

$$W_F = (1 - M_{ff}) \times W_{T0}$$

Moreover, in order to observe airworthiness standards, reserve fuel is considered in case the airplane is obliged to land at an alternate airport in the vicinity of 100 nmi.



In terms of the cruise weight fraction, during which the weight of the burnt fuel is substantial, mathematical calculations predicated upon the Breguet range equation and “constant airspeed, constant lift coefficient” flight program are utilized. The following delineates the final equation in this regard.

$$\left(\frac{W_{final}}{W_{initial}}\right)_{Cruise} = e^{\frac{-R \cdot C}{V \times (L/D)_{cruise}}}$$

In the above formula, R, C, V, and $(L/D)_{cruise}$ stand for the cruise range of the airplane, engine’s SFC, cruising speed of the airplane, and airplane’s cruise L/D, respectively. The amounts of these parameters are determined using the downselected mission profiles, powerplant studies carried out by the propulsion team, RFP, and aerodynamic studies carried out by the aerodynamics team, respectively. In this regard, it is worthwhile mentioning that the 50-seat airplane was sized based upon all of the four mission profiles, and it was concluded that the most challenging mission profile to be fulfilled is the 2-legged 2000 nmi mission; hence, for the Chaka-76, just the 2-legged 2000 nmi mission profile was deemed acceptable for its corresponding design loop.

Regarding estimation of the empty weight for the Chaka-50 and Chaka-76, knowing the overall configuration and type of the target airplane to be designed, the team exploited past history and statistics embedded in a series of empirical equations, found in [22], as well as technology diagrams, plotted by the general design team based upon similar aircraft, for the first design loop. Traveling the design loop a number of times using more accurate techniques [7, 8, 10], the team was able to extract the final empty weights with the accuracy of less than 3 percent discrepancy between the initial and eventual figures input to and output from the design loop. It is worthy to mention that studying the upper left portions (high technology portions) of the plotted technology diagrams showed that the utmost competitive aircraft for the Chaka-50 and Chaka-76 are ERJ-145XR and ERJ-170-100AR, respectively. Equation 2 is used to calculate the empty weight.

$$\text{Equation 2: } W_E = \text{inv. log} \left(\frac{\log(W_{TO}) - \gamma_{Tech}}{x_{Tech}} \right)$$

The trapped fuel and oil weight is estimated to be equal to 0.5 percent of the MTOW, as shown in Equation 3.

$$\text{Equation 3: } W_{TFO} = 0.005 \times W_{TO}$$

Tables 14 and 15 provide a detailed account of the mission profiles upon which the Chaka-50 and Chaka-76 are designed, respectively.



Table 14- Detailed account of the designed Chaka-50 mission profile

Mission segment	Speed (ft/sec)	Time interval (min)	Range (nmi)	Weight fraction	Eventual weight (lb)
1. Engine Start and warm-up	-	-	-	0.99	45455.4
2. Taxi	-	-	-	0.99	45000.9
3. Take-off	-	-	-	0.995	44775.9
4. Climb	300.86	15.9	46.91	0.98	43880.3
5. Cruise	778.45	182.5	1403.25	0.9273	40690.2
6. Descent	286.84	23.3	65.84	0.99	40283.3
7. Landing, Taxi, shutdown	-	-	-	0.992	39961.1
8. Engine start and warm-up, taxi, take-off	-	-	-	0.9751	38970.05
9. Climb	300.86	15.9	46.91	0.98	38190.6
10. Cruise	778.45	68.2	524.25	0.9722	37128.9
11. Descent	286.84	23.3	65.84	0.99	36757.6
12. Landing, taxi, shutdown	-	-	-	0.992	36463.6

Table 15- Detailed account of the designed Chaka-76 mission profile

Mission segment	Speed (ft/sec)	Time interval (min)	Range (nmi)	Weight fraction	Eventual weight (lb)
1. Engine Start and warm-up	-	-	-	0.99	75294.9
2. Taxi	-	-	-	0.99	74541.9
3. Take-off	-	-	-	0.995	74169.2
4. Climb	300.86	15.9	46.91	0.98	72685.9
5. Cruise	778.45	182.5	1403.25	0.9273	67401.6
6. Descent	286.84	23.3	65.84	0.99	66727.6
7. Landing, Taxi, shutdown	-	-	-	0.992	66193.8
8. Engine start and warm-up, taxi, take-off	-	-	-	0.9752	64552.15
9. Climb	300.86	15.9	46.91	0.98	63261.1
10. Cruise	778.45	68.2	524.25	0.9722	61502.45
11. Descent	286.84	23.3	65.84	0.99	60887.4
12. Landing, taxi, shutdown	-	-	-	0.992	60400.3

Observing the calculation procedure delineated above along with considering a ROC of 2200 feet/min, a climb angle of 7 degrees, a ROD of 1500 feet/min, a descent angle of 5 degrees, and a cruise ceiling of 35000 feet, Figure 14 and 15 demonstrate the final significant results yielded for the Chaka-50 and Chaka-76, respectively.

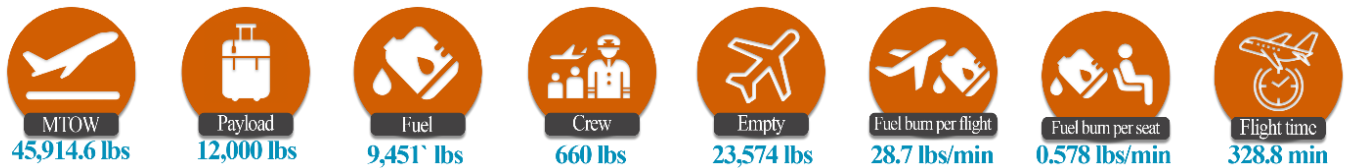


Figure 14- Output data of the Chaka-50

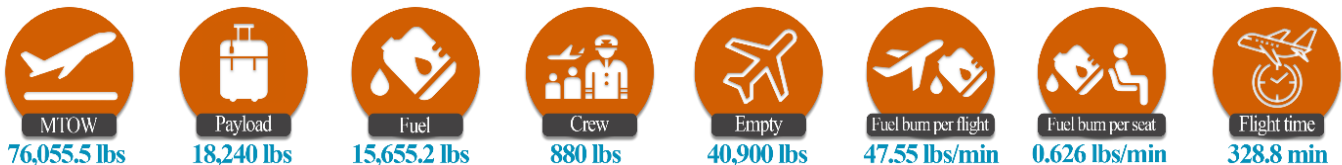


Figure 15- Output data of the Chaka-76



7.2 Matching Chart & Design Point Selection

This step of the airplane's preliminary design process is solely dependent upon flight mechanics theories and the airplanes' performance characteristics required by the RFP and also the general design team.

The equation derived for each performance requirement is expressed in terms of Thrust Loading (T/W) as functions of Wing Loading (W/S). Subsequently, these equations will be collectively plotted in one diagram, the matching chart, with the vertical and horizontal axes representing the thrust loading and wing loading, respectively. Afterward, the acceptable region meeting all of the target airplane's requirements, and, hence, the final design point will be derived, culminating with the desirable wing reference area and engine thrust. It is worthwhile mentioning that the matching chart technique has been implemented in both *sea level ISA + 18°F* and *FL50 ISA + 18°F* conditions for each of the Chaka-50 and Chaka-76, and it was established that the *FL50 ISA + 18°F* condition is of more criticality; hence chosen as the preponderant design condition. Furthermore, the team concluded that the design point ought to be opted for the least S_{ref} (i.e., the least wing wetted area), the points possessing the highest amount of wing loading within the acceptable region, and also the smallest engine (i.e. the lowest cost) among the aforesaid points.

Tables 16 and 17 show the coordinates corresponding to the design point of the 50-seat and 76-seat airplanes in turn. The consequent wing reference areas and engine thrust are presented succeedingly.

Table 16- Output data of the matching chart for the Chaka-50

Parameter	Value
Wing loading in lb/ft^2	98.27
Wing reference area in ft^2	467.18
Total thrust in lb_f	16070
Thrust loading in lb_f/lb	0.35

Table 17- Output data of the matching chart for the Chaka-76

Parameter	Value
Wing loading in lb/ft^2	97.14
Wing reference area in ft^2	781.12
Total thrust in lb_f	18742
Thrust loading in lb_f/lb	0.247

Figure 16 and 17, in the following, illustrate the matching charts corresponding to the Chaka-50 and Chaka-76 in turn. Not only do these charts incorporate the design point of the target airplane under study, but also they have been superimposed by the design points of similar competitive aircraft.

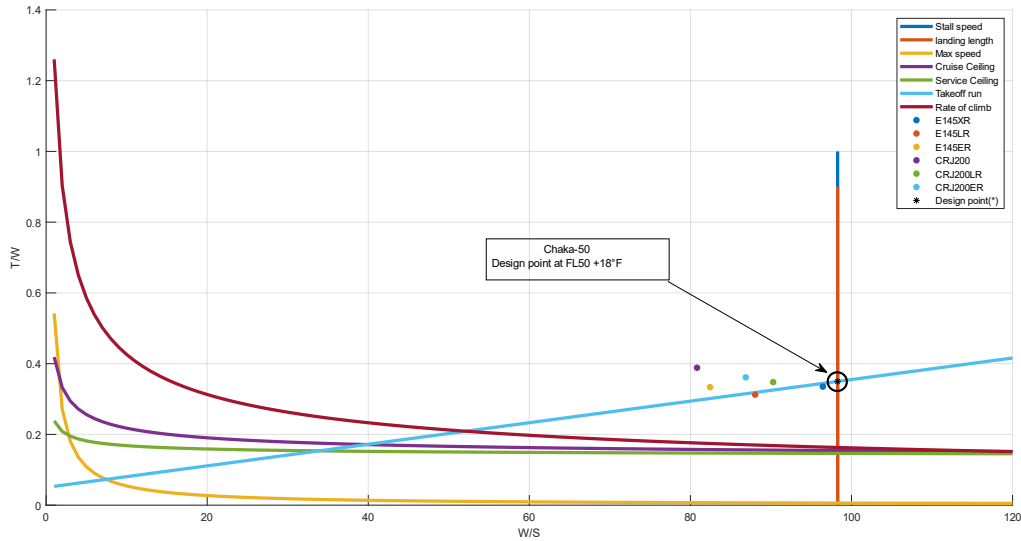


Figure 16- Matching plot of the Chaka-50

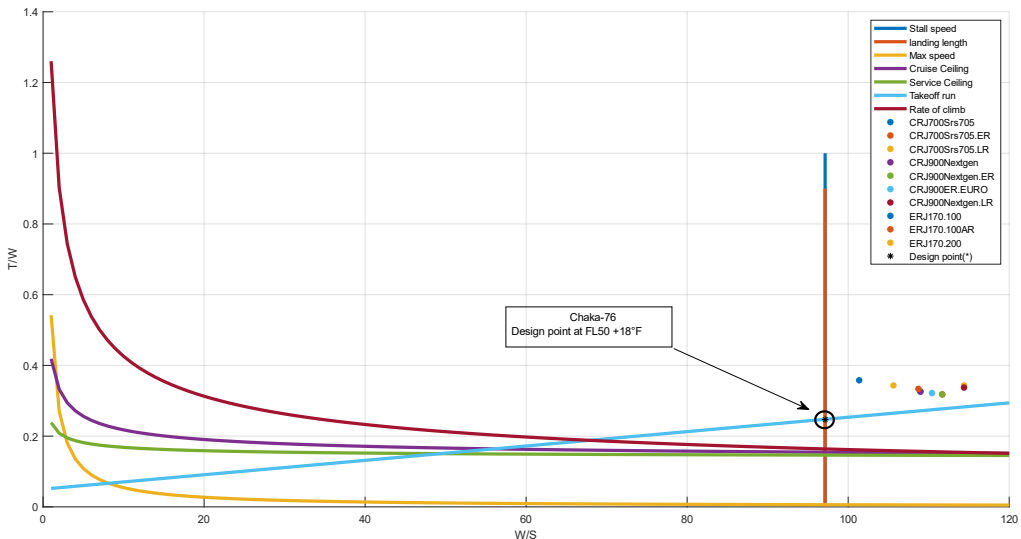


Figure 17- Matching plot of the Chaka-76

7.3 Economic Missions

Now that the Chaka MRJ family has iteratively undergone the preliminary design phase and the endmost results have been yielded, it is time to examine closely whether the two airplanes are capable of fulfilling the economic missions proposed by the RFP: showing the fuel burn performance per trip and per seat and comparing that with the appropriate competitive aircraft at 500 and 1000 nmi.

Running the preliminary design code, written by the general design team, for the Chaka-50, the following results, shown in Table 18, Figure 18, Table 19, and Figure 19, are yielded:



Table 18- Detailed account of the 500 nmi economic mission performed by the Chaka-50

Mission segment	Speed (ft/sec)	Time interval (min)	Range (nmi)	Weight fraction	Eventual weight (lb)
1. Engine Start and warm-up	-	-	-	0.99	40574.26
2. Taxi	-	-	-	0.99	40168.51
3. Take-off	-	-	-	0.995	39967.67
4. Climb	300.86	15.9	46.91	0.98	39168.32
5. Cruise	778.45	50.3	387.24	0.9794	38361.45
6. Descent	286.84	23.3	65.84	0.99	37977.84
7. Fly to alternate and descend	422	23.99	100	0.9672	36732.16
8. Landing, Taxi, shutdown	-	-	-	0.992	37674.01



Figure 18- Main output data of the 500 nmi economic mission performed by the Chaka-50

Table 19- Detailed account of the 1000 nmi economic mission performed by the Chaka-50

Mission segment	Speed (ft/sec)	Time interval (min)	Range (nmi)	Weight fraction	Eventual weight (lb)
1. Engine Start and warm-up	-	-	-	0.99	41686.66
2. Taxi	-	-	-	0.99	41269.79
3. Take-off	-	-	-	0.995	41063.45
4. Climb	300.86	15.9	46.91	0.98	40242.18
5. Cruise	778.45	115.4	887.2	0.9534	38366.89
6. Descent	286.84	23.3	65.84	0.99	37983.22
7. Fly to alternate and descend	422	23.99	100	0.9672	36737.37
8. Landing, Taxi, shutdown	-	-	-	0.992	37679.36



Figure 19- Main output data of the 1000 nmi economic mission performed by the Chaka-50

Running the preliminary design code, written by the general design team, for the Chaka-76, the following results, shown in Table 20, Figure 20, Table 21, and Figure 21, are yielded:

Table 20- Detailed account of the 500 nmi economic mission performed by the Chaka-76

Mission segment	Speed (ft/sec)	Time interval (min)	Range (nmi)	Weight fraction	Eventual weight (lb)
1. Engine Start and warm-up	-	-	-	0.99	67209.45
2. Taxi	-	-	-	0.99	66537.35
3. Take-off	-	-	-	0.995	66204.67
4. Climb	300.86	15.9	46.91	0.98	64880.57
5. Cruise	778.45	50.3	387.24	0.9794	63544.03
6. Descent	286.84	23.3	65.84	0.99	62908.59
7. Fly to alternate and descend	422	23.99	100	0.9672	60845.19
8. Landing, Taxi, shutdown	-	-	-	0.992	62405.33



Figure 20- Main output data of the 500 nmi economic mission performed by the Chaka-76

Table 21- Detailed account of the 1000 nmi economic mission performed by the Chaka-76

Mission segment	Speed (ft/sec)	Time interval (min)	Range (nmi)	Weight fraction	Eventual weight (lb)
1. Engine Start and warm-up	-	-	-	0.99	69052.1
2. Taxi	-	-	-	0.99	68361.58
3. Take-off	-	-	-	0.995	68019.77
4. Climb	300.86	15.9	46.91	0.98	66659.37
5. Cruise	778.45	115.4	887.2	0.9534	63553.05
6. Descent	286.84	23.3	65.84	0.99	62917.52
7. Fly to alternate and descend	422	23.99	100	0.9672	60853.82
8. Landing, Taxi, shutdown	-	-	-	0.992	62414.18



Figure 21- Main output data of the 1000 nmi economic mission performed by the Chaka-76

Comparing the fuel burn of the Chaka-50 and Chaka-76 to that of their utmost competitive aircraft (pertinent data can be found in [24-30]), ERJ-145XR and ERJ-170-100AR respectively, Table 22 provides the amounts with which fuel burn performance for the 500 and 1000 nmi missions has been ameliorated by the Chaka MRJ family.

Table 22- Improvement in fuel burn performance procured by Chaka MRJ family

Aircraft type	Fuel burn in 500 nmi mission (lb/min)	Abatement percentage in fuel burn (%)	Fuel burn in 1000 nmi mission (lb/min)	Abatement percentage in fuel burn (%)
Chaka-50	51.51	22.32	43.45	27.07
ERJ-145XR	40.01		31.69	
Chaka-76	84.73	21.80	72.13	27.21
ERJ170-100AR	66.26		52.50	

As can be seen in Table 22, not only has the Chaka MRJ family design been able to achieve the RFP’s overall aim of being at least 20% better in terms of fuel burn compared to the existing 50-seat regional jets, but also it has fulfilled the aforementioned compared to the existing 76-seat regional jets. To do so, developments in three crucial disciplines of aircraft design, namely aerodynamic efficiency, empty weight, and powerplant, had to be implemented. The disciplines, by and large, can be designated by the airplane’s cruise L/D, overall structural weight, and the engine’s cruise SFC, respectively. In accordance with the available data germane to such disciplines for the two competitive aircraft [24, 31, 32] and the data yielded by the MRJ Family design, it can be said that the ShadX team has been able to produce percentage improvements such as the ones shown in Figures 22-23, for the Chaka-MRJ family.



Figure 22- Amelioration occurred in terms of the three disciplines for the Chaka MRJ family compared with competitive RJs

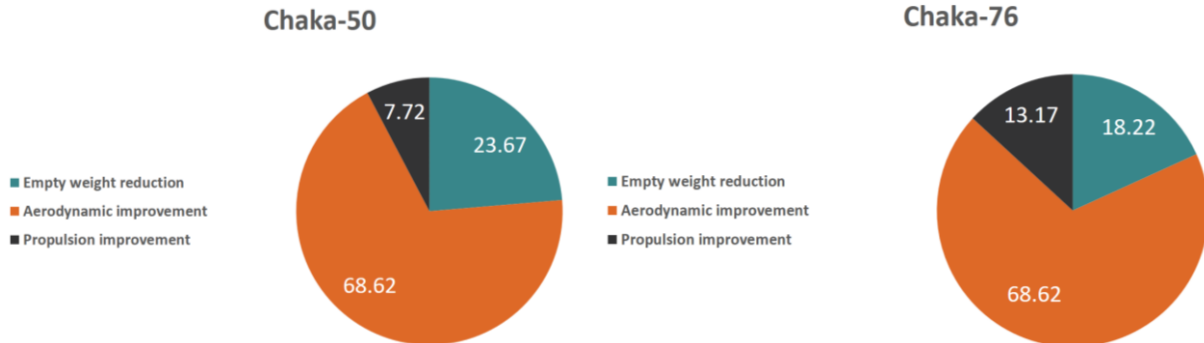


Figure 23- The percentage of three ameliorating factors

7.4 Studying the Optimal Cruise Altitude

Utilizing the Breguet range equation, the general design team has extracted the optimal cruise altitude for the 500 and 1000 nmi missions. While evaluating the aforementioned, the main challenge would be to calculate the precise amounts of SFC and L/D simultaneous to altitude change.

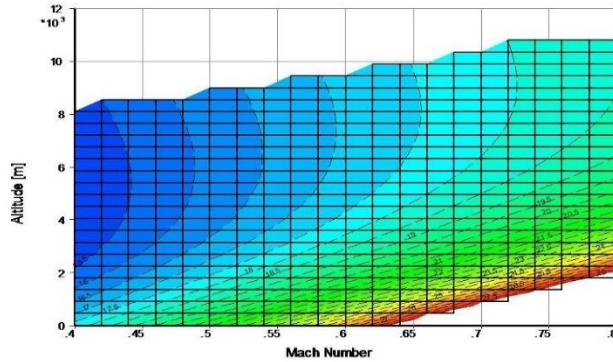


Figure 24-SFC Change of the proposed engine

GasTurb has been used to calculate the SFC change of the proposed engine for the Chaka MRJ, going through the elevations up to 60,000 ft while the Mach varies between 0.7 and 0.9. Figure 24 presents the SFC change.

In terms of the L/D , it has been assumed that the average cruise weight is equal to the lift force, and also the drag data of the designed components have been utilized in order to estimate the parasitic and induced drag forces. In the code, written by the general design team, the density and speed of sound vary based upon altitude change; hence, the exact values of L/D and cruising speed are calculated simultaneous to altitude change.



The analysis showed that the engine’s *SFC* will remain constant above 45,000 ft and that the *L/D* change will be negligible above 50,000 ft. It is obvious that as the altitude increases and the speed decreases, the amount of fuel consumption decreases. For the general design team, the significant points to consider were the engine’s capability to reach the desired altitude and the amount of fuel consumption while climbing to the desired altitude.

Regarding all the points mentioned above and analyzing the output data, the team concluded that the elevation of 35,000 ft is the optimal cruise altitude for Mach 0.8 when the focus is on both the aircraft’s performance and cost.

Figure 25 and 26 delineate the concept for the Chaka-50 in terms of the 500 and 1000 nmi missions.

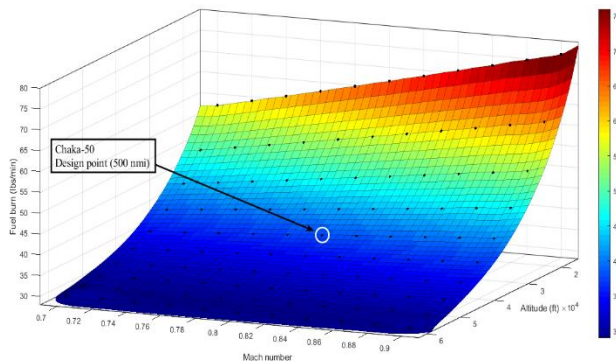


Figure 25- Optimum cruise altitude for the Chaka-50 in 500 nmi mission

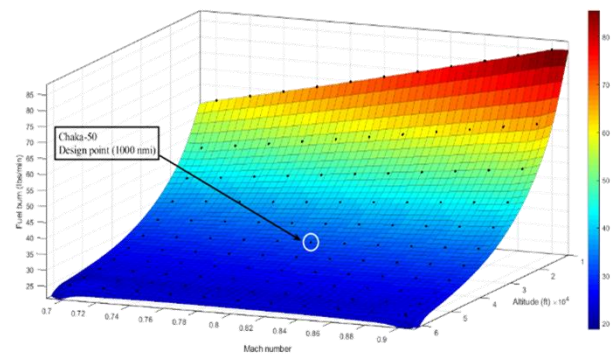


Figure 26- Optimum cruise altitude for the Chaka-50 in 1000 nmi mission

8 Fuselage Design

In this section, the fuselage design procedure of the Chaka MRJ family is presented. Based on the preliminary design phase, both aircraft must generate considerably higher values of aerodynamic efficiency parameter (*L/D*) compared to the competitive aircraft. The fuselage is responsible for generating a noticeable portion of this *L/D*; therefore, the fuselages are designed for this purpose. Figure 27 presents the road map of fuselage design.

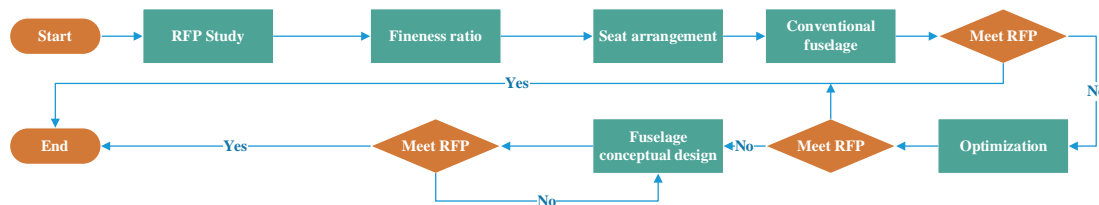


Figure 27- Fuselage design road map

8.1 Determination of Fineness Ratio

There are various inconsistent diagrams in terms of fuselage fineness ratio versus its overall drag coefficient in the literature, making the selection of fineness ratio challenging. To overcome this problem, a 2-D conventional fuselage, possessing various slenderness ratios, was numerically simulated at cruise condition, using the Fluent. Consequently, an original diagram, in this regard, was obtained in order to design the RJs’ fuselages.



Figure 28 represents the change occurred in terms of overall C_D and area-weighted average Vorticity, influencing the aerodynamic and acoustic performance, versus fineness ratio. Designing two RJs with different passenger capacity required determination of optimum fineness ratios in favor of both aircraft's C_D and area-weighted average Vorticity. Analyzing the output in this regard, the team came up with the values of 12.5 and 15.8 for the Chaka-50 and -76, respectively.

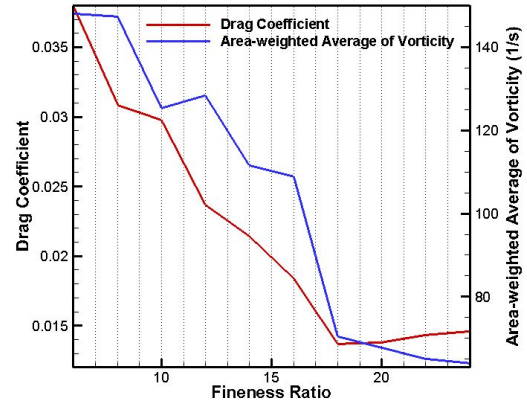


Figure 28- Drag coefficient and area-weighted average Vorticity vs. fuselage fineness ratio

8.2 Seating Arrangement Selection

Having determined the appropriate fineness ratio, the team could decide on the proper seating arrangement. Figure 29 provides an overview of the drag force generated in terms of 1+1, 2+1, and 2+2 seating arrangements. According to the figure, the minimum drag force is generated by the 1+1 arrangement. Nonetheless, due to high aircraft length increment and based upon structural and W&B analysis, the 1+1 arrangement was not practical; hence, the 2+1 arrangement was selected for the Chaka.

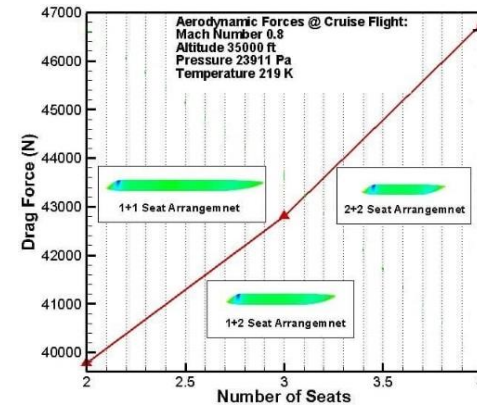


Figure 29- Generated drag vs seating arrangements

8.3 Conventional Fuselage Assessment

Firstly, the four competitive aircraft's fuselages were studied numerically. The overall drag coefficient of each fuselage was calculated using the Fluent software in order to study their aerodynamic performance. Table 23 presents the corresponding C_D of each fuselage, showing that the minimum C_D belongs to E170.

Table 23- Rankings of competitive aircraft's fuselage C_D

Aircraft	C_D	Ranking
Embraer E170	0.04867	1
Bombardier CRJ200	0.06971	2
Mitsubishi M100	0.07925	3
Embraer E145	0.09331	4

However, due to lack of essential aerodynamic performance, even this design is not suitable for the Chaka family. The numerical simulations of the flow around competitive RJs' fuselages demonstrated that about 70% of the fuselage drag is generated near the nose, which could be diminished to some degree using geometric optimization tools. Figure 30 shows the pressure and laminar viscosity contours around the nose, which are the main factors in generating drag.

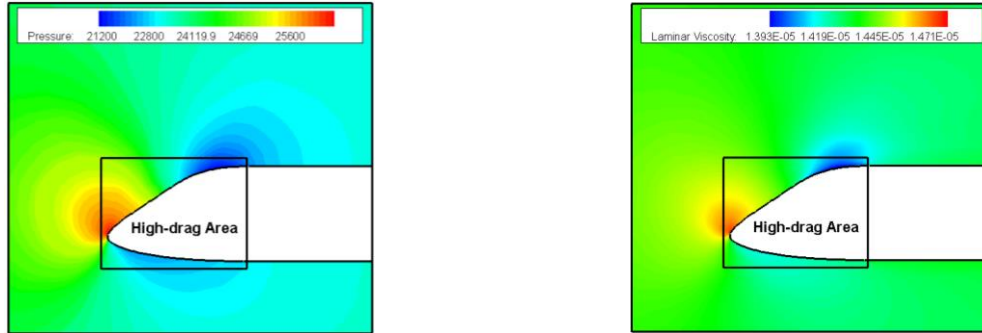


Figure 30- High-drag area on the contour of static pressure (left) and laminar viscosity (right) for E170 fuselage cross-section

In order for the nose to be optimized, E170's geometry, having the least amount of C_D based on Table 23, was used.

The optimization procedure was carried out by coupling genetic optimization algorithms and the Fluent in 30 steps.

Figure 31, shows the C_D change in this regard, yielding that the 26th point is the optimal geometry. According to the

figure, the optimization process reduced nose drag by 30%; however, the aerodynamic performance was still not adequate, and too much drag was generated. The time lapses of the optimization procedure are represented in [the link](#).

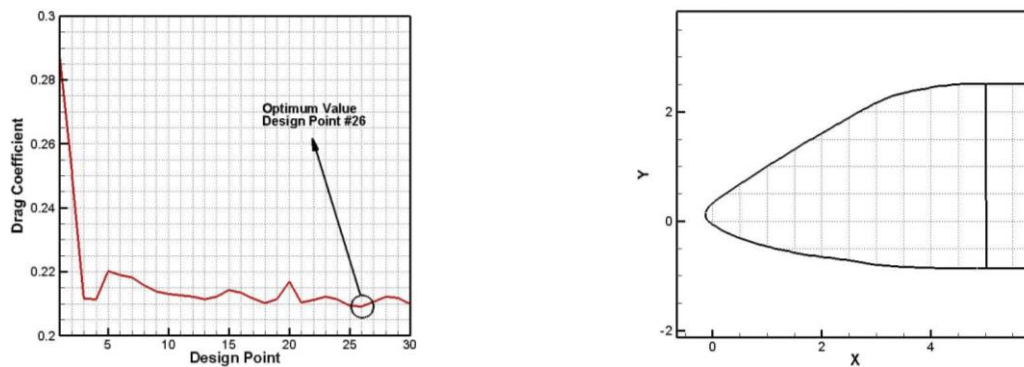


Figure 31- Drag coefficient of nose versus design point (left) and optimum nose geometry (right)

8.4 Fuselage Conceptual Design

As was shown above, in spite of the fact that optimization were implemented on the competitive RJs' fuselages, the amount of C_D reduction was not satisfying; hence, it is necessary to exploit unconventional design configurations.

The idea is to use an airfoil-shaped geometry for the fuselage, ameliorating the aerodynamic performance of the fuselage. Figure 32 depicts schematic views of the conventional and airfoil-shaped fuselage geometries.



Figure 32- Conventional fuselage (left) and airfoil-shaped fuselage (right)

Table 24 presents comparison between conventional and airfoil-shaped fuselages. According to the table, the airfoil-shaped, while having high R&D and manufacturing cost, aerodynamically satisfies the needs of aircraft.

Table 24- Qualitative comparison between different fuselage geometries

Fuselage design designation	Structural consideration	Performance	R&D	Production cost	Aerodynamic efficiency
Conventional (sharp-nose)	Low	Low	Enough	Low	Medium
Conventional (round-nose)	Low	Medium	Enough	Medium	Medium
Airfoil-shaped	Medium	High	Not enough	High	High

In accordance with the airfoil selection process, NASA SC(2) 0712 airfoil was used for the fuselage design; however, some changes have been applied to the original airfoil in order to adapt its geometry to fuselage application. Figure 33 displays the view of the designed fuselage and its differences with the original airfoil. According to the figure, some modifications have been made to the tail region, preventing structural vulnerability in the aft section.

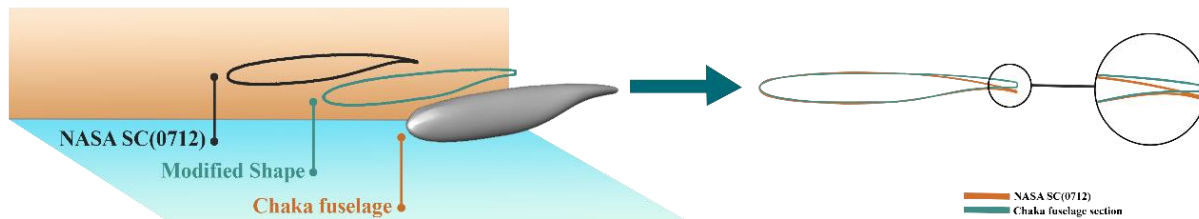


Figure 33- Comparison between the NASA SC(2) 0712 airfoil and Chaka MRJ fuselage configuration

Table 25 presents the comparison between conventional and airfoil-shaped fuselages in terms of the following parameters: Acoustic power level, L/D, Vorticity magnitude, and pressure fluctuations. According to the table, not only will the airfoil-shaped fuselage improve aerodynamic performance, but also it will reduce the amount of noise.

Table 25- Performance enhancement of the airfoil-shaped fuselage with respect to the conventional fuselage

Parameter	Enhancement (%)
Lift-to-drag ratio	+70%
Total acoustic power level (dB)	-25%
Vorticity magnitude (m^2/s^2)	-20%
Pressure fluctuations	-30%

Figure 34 depicts the pressure contour for the airfoil-shaped fuselage. According to the figure, using airfoil geometry reduces the high-drag area and also retains uniform pressure distribution along the fuselage, showing no indications of adverse pressure gradient.

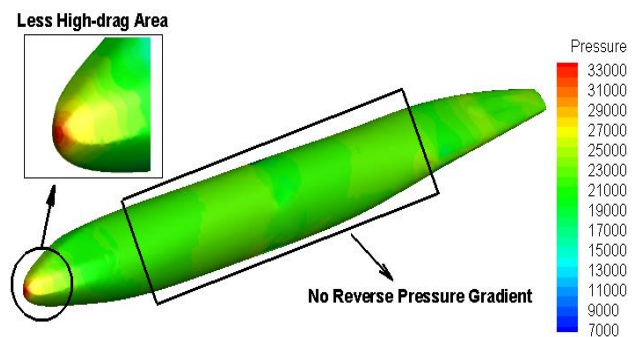


Figure 34- Static pressure contour on the Chaka-50 airfoil-shaped fuselage

9 Propulsion System

Possessing ameliorated fuel burn of at least 20% in 500 nmi block fuel per seat has been declared as the objective of the RFP. A systematic approach is used to design the propulsion system, as depicted in Figure 35 [21, 33, 34].

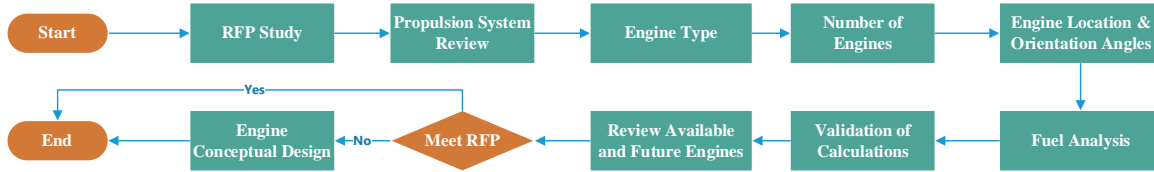


Figure 35- Road map of the Propulsion System

9.1 RFP Study

The 1st step toward designing the aircraft’s propulsion system is to excerpt RFP requirements and priorities. In accordance with the preliminary design and RFP study carried out, the following focal points are identified:

- Generation of the aircraft’s required thrust
- Possessing competitive SFC, weight, and cost
- Maximum freestream Mach number to be 0.9
- Provision of evidence in terms of EIS by 2029

9.2 Review of Propulsion Systems

Figure 36 delineates the classification of common powerplants exploited in civil aviation. The following subsections present descriptions of each class briefly.

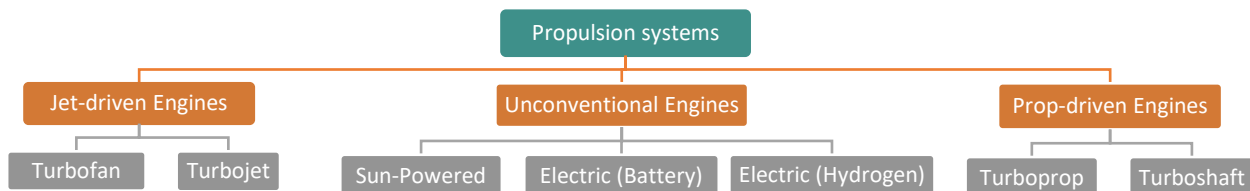


Figure 36- Classification of applicable propulsion systems to civil aviation

Sun-powered propulsion systems: Solar engines are to be utilized in high-endurance flights [35], which is not an essential with regard to regional jets [36].

Electric propulsion systems comprised of batteries: In spite of the aviation movement toward electricity, Lithium batteries can generate 200 W.h/kg of energy whereas jet fuel does the same 60 times as much [37], [38].

Electric propulsion systems comprised of hydrogen: In this type of electric engines, electricity is supplied by hydrogen. The product of hydrogen combustion is vapor, having no environmental pollution at all [39]; however, risk of low TRL along with airport considerations and auxiliary equipment does not guarantee the profitability [40].

Turboprop propulsion systems: Turboprop engines have a background in civil aircraft performing subsonic flights of not greater than Mach 0.6 at medium flight altitudes [21].

Turboshaft propulsion systems: This type of engine is used in helicopters and aircraft APU systems [41].

Turbojet propulsion systems: These engines are capable of flight at high speeds and altitudes, so they were widely used in civil aviation germane to the 20th century [21]. Thus, it is possible to use turbojet engines in RJs.



Turbofan propulsion systems: Turbofan engines are the most widely used powerplant systems used in civil aviation and can be used in RJs thanks to ability to fly at high speeds and altitudes with less SFC than turbojets [21].

Table 26 briefly illustrates the feasibility analysis, carried out by the propulsion team.

Table 26- Feasibility analysis of conventional and unconventional propulsion systems with respect to regional jets

System type	TRL	Performance	R&D level	Risk assessment	Maintenance cost
Sun-powered	5	Low	Not enough	Low	High
Electric-battery	4	Low	Not enough	Low	Medium
Electric-hydrogen	7	Enough	Not enough	High	High
Ramjet/Scramjet	9	Low	Appropriate	Low	Low
Turboprop	9	Low	Appropriate	Low	High
Turbofan	9	Enough	Appropriate	Low	High
Turbojet	9	Enough	Appropriate	Low	Medium

9.3 Engine Type Selection

In order to opt for an appropriate engine type, first, it is necessary to define the parameters of the selection process. The parameters were prioritized based upon a survey conducted using 30 aeronautical experts' standpoints. Figure 37 provides information of the experts, including the discipline they work at, academic degree and expertise they possess.

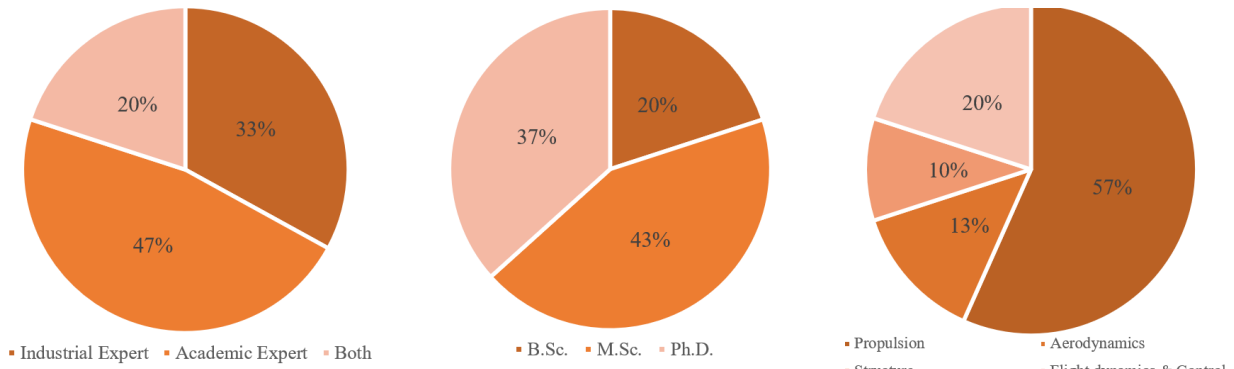


Figure 37- Employment discipline (left), Academic degree (middle), and Expertise (right) distribution of the pundits

Assigned weights to the parameters, based upon survey analysis, are shown in Table 27.

Table 27- Engine type selection parameters, significance percentage

Factor	Weight	Best
Prevalence in RJs	9%	Turbofan
Pax comfort and appeal	8%	Turbofan
Speed capability	11%	Turbojet
Ceiling	6%	Turbojet
Maintainability	5%	Turbojet
Propulsive efficiency	15%	Turbofan
Specific weight	10%	Turbojet
Noise	7%	Turbojet
Cost	9%	Turbojet
SFC	20%	Turbofan

The final score and ranking are shown in Table 28, stating that the appropriate engine type for the Chaka MRJ Family is turbofan.

Table 28- Final scores and rankings of the candidate engines

Engine Type	Ranking	Score
Turbofan	1	52
Turbojet	2	48



9.4 Number of Engines Selection

Initially, probable choices with regard to number of engines are examined, according to literature [21, 33, 34, 42-44]. In this regard, Table 29 provides an overview of the scores allocated to various number of engine choices.

Table 29- Scores with regard to number of engine choices, based upon selected criteria

Number of engines	Prevalence in RJs	Reliability	Controllability	Operational Cost	Weight	Cost	Safety	Score
One engine	1	1	1	5	5	5	1	19
Two engines	5	2	2	4	4	4	2	23
Three engines	2	3	3	3	3	3	3	20
Four engines	2	4	4	2	2	2	4	20
Distributed engines	0	5	5	1	1	1	5	18

The results are shown in Table 29. According to the table, the twin-engine configuration is the best choice, offering apt cost and reliability.



9.5 Engine Location

According to even number of engines, two approaches with regard to engine location are available:

- 1) Podded beside the rear section of the fuselage
- 2) Podded under the wing

Table 30 provides an analysis in terms of installation locations. For the Chaka RJ family, the former is selected, bringing about longitudinal stability enhancement and less engine heat and noise transfer to the cabin.

Table 30- Summary analysis of the two applicable engine locations

	Podded beside the rear section of the fuselage	Podded on the wing
Sample figure		
Aerodynamic features	- No limitations in low-wing region - Possible use of all wing area - Nose down moment production	- Occupying the Local wing area - Nose-up moment production - Engine wake effect on the empennage
Acoustic characteristics	- More distance from cabin	- Probable noise transfer to the cabin
Heat transfer effect	- No engine heat transfers into the cabin - Negligible effect on aircraft components	- Probable engine heat transfer to the cabin - Lifetime reduction of components
Stability impression	- Smaller thrust moment arm - Enhance longitudinal stability	- Bigger thrust moment arm - Small effect on aircraft CG
Structural consideration	- Lower pylon weight - Possible uniform wing main spar design - Smaller required landing gear	- Higher pylon weight - Necessity of wing main spar separation - More complexity in wing structural design
Maintainability	- Hard engine accessibility for maintenance	- Easy engine accessibility for maintenance
Engine-out control	- Less effect on yaw stability	- Possible negative effect on yaw stability
Fire hazard	- Appropriate distance between tankers and cabin	- Proximity of tankers to cabin
Foreign object ingestion	- More distance from the ground	- Higher risk of object ingestion



9.6 Engine Location and Orientation Installation

Since the performance of jet engines depends on quality and mass flow rate of the incoming air, it is of paramount importance to find the optimum installation point of the engines. In this section, the optimal location and length of the pylons are examined using CFD. Table 31 shows fuselage boundary layer thicknesses in various sections. According to the Table, Section 6 is the optimal section to be used in order for the pylons to retain the least length possible.

Table 31- Fuselage sections taken into account for the numerical simulations to be carried out

Section No.	1	2	3	4	5	6	7	8	9	10	11
Distance ratio from fuselage top point	0.05	0.1	0.15	0.2	0.25	0.3	0.35	0.4	0.45	0.5	0.55
BL Thickness (in)	7.4	6.2	5.8	5.4	4.3	3.5	5.8	5.1	5.5	5.1	8.6

Figure 38 illustrates the velocity magnitude contour around section 6. As the figure shows, it is possible to mount the engines on the allowed area. It goes without saying that the exact location in the box will be selected based upon weight and balance calculations.

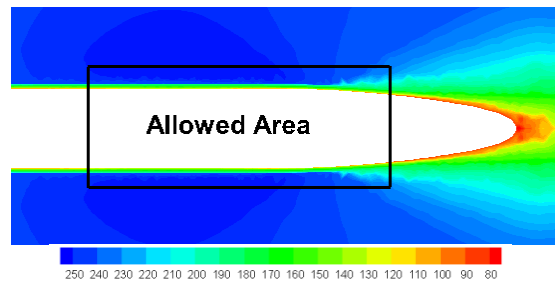


Figure 38- Velocity magnitude contour of the optimal section

According to literature, two angles, namely nose-up pitch (normally about 2° to 5°) and nose-outward (normally about 1° to 3°), are of significance in terms of engine installation [21]. In order to minimize engine’s SFC and efficiency loss, optimum values of the aforesaid angles must be determined. Table 32 provides an overview of 12 numerical simulations, run at cruising condition, where run 7 represents the optimal orientations.

Table 32- Various numerical simulations carried out in order to find out optimum engine orientations

Run number	1	2	3	4	5	6	7	8	9	10	11	12
Nose-up pitch angle (°)	5	5	5	4	4	4	3	3	3	2	2	2
Nose-outward angle (°)	3	2	1	3	2	1	3	2	1	3	2	1
Flow rate (lb/s)	196.2	196.5	197	197.2	197.8	199.3	200.1	198.2	197.5	197.1	196.5	196
Vorticity (lb ² /s ²)	1264	1262	1258	1253	1248	1242	1237	1241	1245	1249	1260	1264

Figure 39 illustrates temperature contour of engine outlet flow which shows flow has enough distance from the ground and fuselage skin.

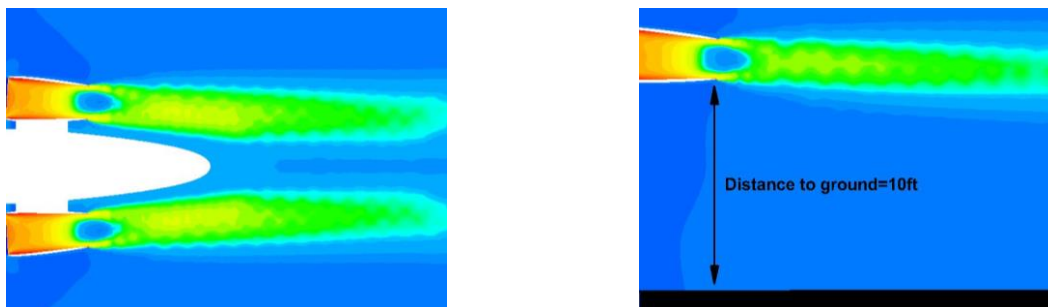


Figure 39 Temperature contour of engine outlet flow



9.7 Fuel Selection

One way to reduce pollution is to use SAFs, which are approved by IATA and ICAO based on ASTM standards. 3 categories of SAFs have satisfied the standards, including Hydro-treated Esters and Fatty Acids, Alcohol-to-jet, and Fischer-Tropsch [45]. As the RFP emphasizes economic aspects and rapid profitability, it is necessary to analyze the fuel in this perspective. To do so, economic effects of alternative fuels on airlines and airports are shown in Table 33 [45]. According to the table, SAFs increase the operational costs [46], so CAF is recommended to be used for the Chaka MRJ family.

Table 33- Economic effects of using SAFs in aviation

Field	Factor	Effect	Result
Commercial airlines	Economic burden	-	Should be shared between the society & passengers
	Cost compared with CAF	-	Should be shared between the society & passengers
	Aviation emission taxes	+	Will be reduced thanks to less environmental emission
	Fuel efficiency	+	Less expense
Commercial airports	Economic burden	-/+	Share between passengers, and reduce transportation costs
	Self-supplied	+	Decentralized production
	Less CO ₂ emission	+	Enhanced local air quality and cost reduction

9.8 Validation of SFC Calculations

This section examines the engine performance of 50 and 76-seat utmost competitive aircraft, including E145XR and E170. To do so, GasTurb software is used to carry out simulations with regard to thermodynamic cycles and fuel consumption. Table 34 sets forth general information corresponding to competitive aircraft’s engines.

Table 34- General specifications of the available RJ engines

Engine name	Bypass ratio	Engine thrust	Cruise SFC	Dry weight	Length	Height	Width
AE 3007-A1E	5:1	7339 lbf	0.65 lb/(lbf.h)	1657 lb	115.1 in	55.7 in	46.1 in
CF 34-8E	5:1	13500 lbf	0.68 lb/(lbf.h)	3147 lb	121 in	53 in	46.2 in

In the first place, it is of vital importance to validate the simulations using sea level test data. For this to happen, the comparison study will take into account the values of output thrust and SFC for the corresponding engines. In Table 35, collected data using the data sheets [47-50], accompanied by the simulation results are presented.

Table 35- Validation of results output by GasTurb 10 using the available RJ engines data

Engine Name	Calculated Thrust	Reported Thrust	Error	Calculated SFC	Reported SFC	Error
AE 3007-A1E	7290 lbf	7351 lbf	0.83 %	0.365 lb/(lbf.h)	0.361 lb/(lbf.h)	1.2 %
CF 34-8E	13596 lbf	13520 lbf	0.56 %	0.356 lb/(lbf.h)	0.354 lb/(lbf.h)	0.51%

9.9 Available and Future Engines

Firstly, available and future engines were examined. Reviews demonstrated that there would be no products possessing ameliorated SFC compared to current engines. It is worthy to mention that, among future products, the



small-medium turbofan of the ENOVAL project can be used in 76-seat aircraft; which despite having low SFC, due to high weight, is not well-qualified for the Chaka MRJ family.

Considering the fact that the ENOVAL project does not offer a promising design in terms of engines apt for RJ aircraft (due to excessive heft originated with the ultra-high bypass design), and that other engine corporations have not provided befitting designs in this regard, the ShadX propulsion team decided that, thanks to growing market demand for RJs in the upcoming years, it is better they come up with a brand-new family design in terms of turbofan engines. The family encompasses thermodynamic and performance characteristics determined using the technology level which will have been procured by 2022. The principal objective is to provide ample improvements and adequacy with regard to manufacturing technology of the proposed engine family by the year 2029.

9.10 Engine Conceptual Design

Predicated upon the level and trend of the technology, a family of turbofan engines is proposed for the Chaka RJs according to Table 36. The table provides an overview of chief specifications possessed by the proposed engines, classified into two general categories: primary data, and components' efficiency.

Table 37 provides information about the performance of the proposed engines in terms of static sea level and cruise conditions, accompanied by comparison with the competitive engines. It can be seen that the proposed engines enjoy ameliorated SFC, propulsive efficiency, and emission.

Table 36- Thermodynamic details of the proposed turbofan engines

	Parameter	Chaka	Value	TRL
Primary data	Intake pressure ratio	50	0.99	9
		76	0.99	9
	Outer fan pressure ratio	50	1.45	9
		76	1.5	9
	Bypass duct pressure ratio	50	0.975	9
		76	0.98	8
Design bypass ratio	50	8	8	
	76	10	9	
Efficiency of components	Low-pressure compressor	50	87 %	8
		76	88 %	8
	High-pressure compressor	50	87 %	8
		76	88 %	8
	Low pressure turbine	50	89 %	8
		76	90 %	7
	High-pressure turbine	50	90 %	7
		76	90 %	7

Table 37- General performance of the proposed turbofan engines

Aircraft Type	Parameter	Value	Comment
Chaka-50	Static sea level SFC	0.327 lb/(lbf.h)	9.42% reduction compared to AE3007-A1E
	Cruise SFC (35000 ft-Mach 0.8)	0.62 lb/(lbf.h)	2.61% reduction compared to AE3007-A1E
	Net thrust	9678 lbf	Sufficient thrust for cruise and take-off
	Specific NO _x	0.1043	Less nitrogen-based emission
Chaka-76	Static sea level SFC	0.319 lb/(lbf.h)	9.82% reduction compared to CF 34-8E
	Cruise SFC (35000 ft-Mach 0.8)	0.62 lb/(lbf.h)	9.75% reduction compared to CF 34-8E
	Net thrust	10619 lbf	Sufficient thrust for cruise and take-off
	Specific NO _x	0.1841	Less nitrogen-based emission

In order for the proposed engines' specifications to be estimated, a multi-layer perceptron neural network has been implemented. The neural network receives thrust, SFC, and bypass ratio as inputs, and outputs engine's fan diameter, length, weight, and price to find the approximated results of the engines. Figure 40 shows a view of the neural network.

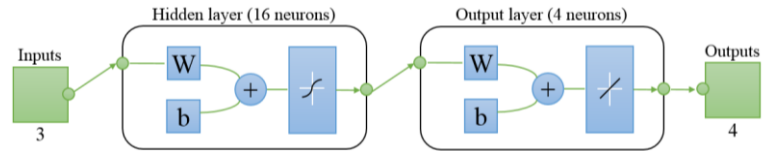


Figure 40- Applied MLP neural network for data estimation of the proposed engines

Table 38 illustrates the estimated values of the proposed engines specifications, using neural network.

Table 38- Estimated data of the proposed turbofan engines

Type	Weight	Length	Diameter	Price
Chaka-50	1680 lb	104 in	54 in	1.80 M\$
Chaka-76	2150 lb	117 in	63 in	2.05 M\$

9.11 Engine Performance Calculations

In this section, performance diagrams and SFC calculations of the proposed engines are provided. Figure 41 illustrates the SFC diagrams of the designed engines in terms of altitude versus Mach number. According to the figure, the maximum cruise altitude and Mach number are 35000 ft. and 0.8, respectively. The figure also shows that the engines can fly at high altitudes with the Mach number 0.8 and possess less SFC compared to competitive engines.

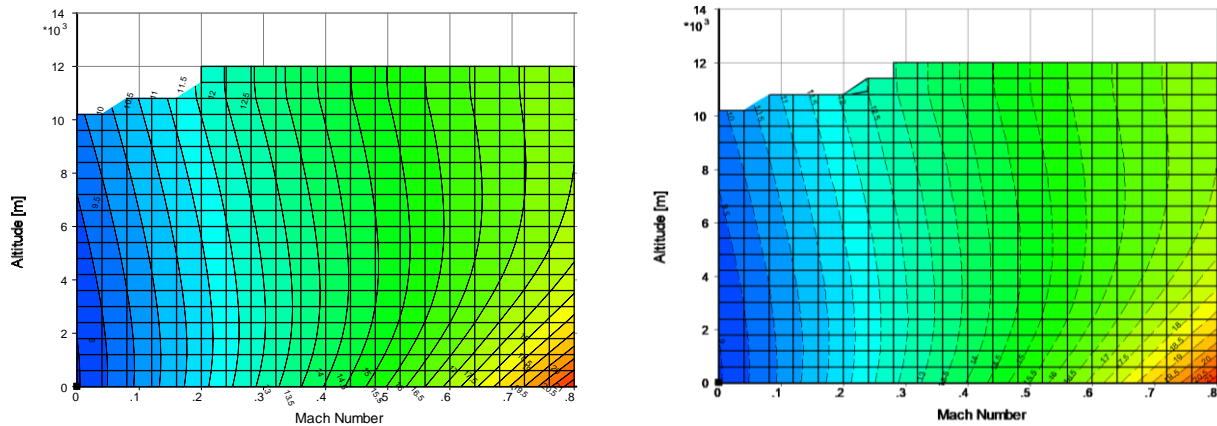


Figure 41- SFC Values of the proposed engines (50-seat on the left, and 76-seat on the right), expressed as Altitude vs. Mach number

Figure 42 and 43 show the take-off SFC values of the proposed engines at the 20 airports of the Scope Clause having high traffic. Meteorological data are the average values of recent 5 years, which are extracted from tutiempo [51]. According to the figure, the proposed engines display enhanced performance compared with the competitive aircraft engines; not only do the proposed designs encompass abatement of fuel consumption at cruise flight but also they demonstrate resembling performance in transient flight conditions such as take-off, hence; it is anticipated that exploitation of the proposed engines will bring about SFC improvements in all flight segments.

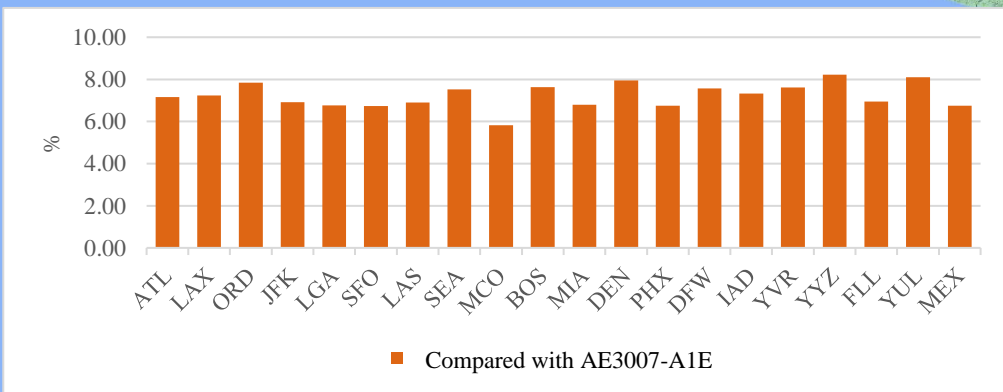
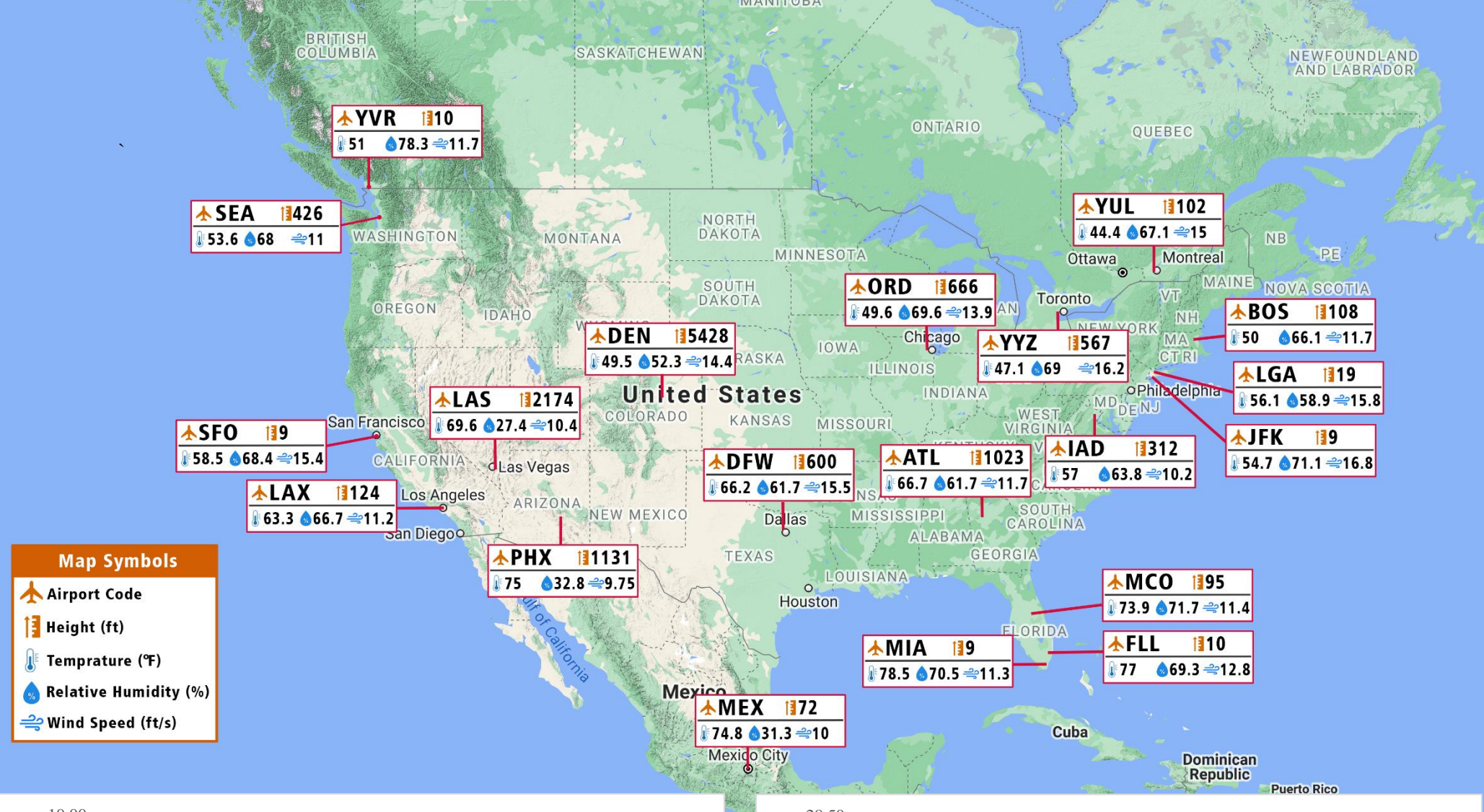


Figure 43- Take-off SFC enhancement of Chaka-50 proposed engine comparing with competitive RJ engine

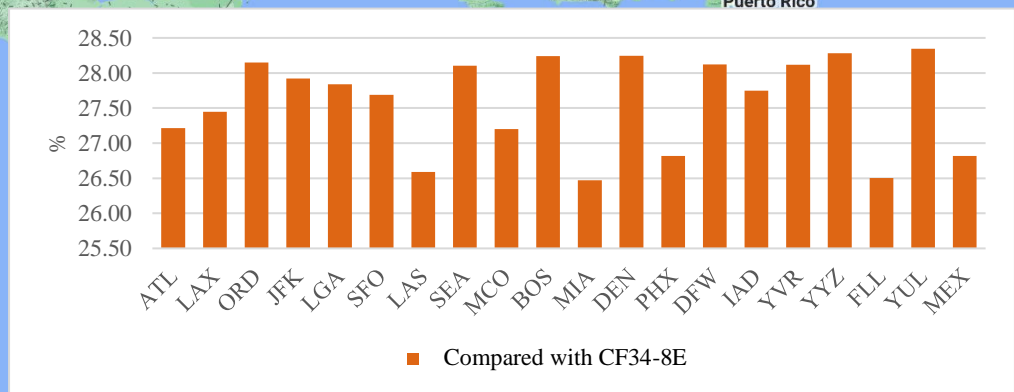


Figure 42- Take-off SFC enhancement of Chaka-76 proposed engine comparing with competitive RJ engine



9.12 Recommendation of Engine Manufacturer

In order for the proposed engines to be manufactured, the propulsion team has reviewed the technology level of prominent engine manufacturers to propound the finest choice. Therefore, the dimensionless figure of Company Technology Characteristic (CTC) is defined based upon Equation 4. The parameter incorporates maximum thermal efficiency of the compressor, turbine, and engine core with the average time of their engines’ overhaul, in-service, warm-up, and maintenance accompanied by the companies’ experience in the production of RJ engines.

$$\text{Equation 4: } CTC = \frac{\eta_{compressor} \times \eta_{turbine} \times \eta_{core} \times t_{overhaul} \times t_{in-service} \times CF}{t_{warm-up} \times t_{maintenance}}$$

A list of civil aircraft turbofan engine manufacturers has been gathered in order to calculate the variables in Equation 4. Afterward, CTC parameter is calculated and normalized. According to the Figure 44, the best options are Rolls Royce and GE, in turn.

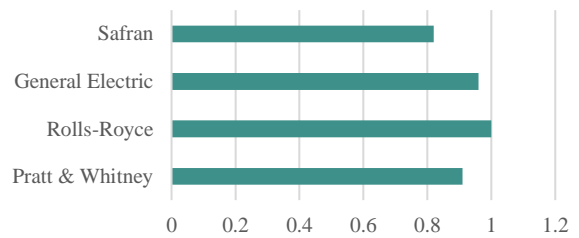


Figure 44- Normalized values of the CTC for manufacturers

9.13 Special considerations

One of the RFP’s requirements is the Capability of performing take-offs at FL50; hence, the performance of the proposed engines is examined for the aforementioned. Using GasTurb, the engines’ performance in maximum take-off thrust phase is evaluated as shown in Table.

Table 39- Atmospheric conditions considered in order to conduct parametric study into the proposed engines at FL50

Parameter	Start Value	End Value	Number of Steps	Step Size
Delta T from FL50	-25 K	25 K	21	2.4 K
Relative Humidity	0 %	100 %	21	5 %

Figure 45 provides an overview of the output thrust of the engines in different Delta T’s and relative humidity at FL50. According to the figure, the proposed engines are capable of supplying sufficient thrust for take-off.

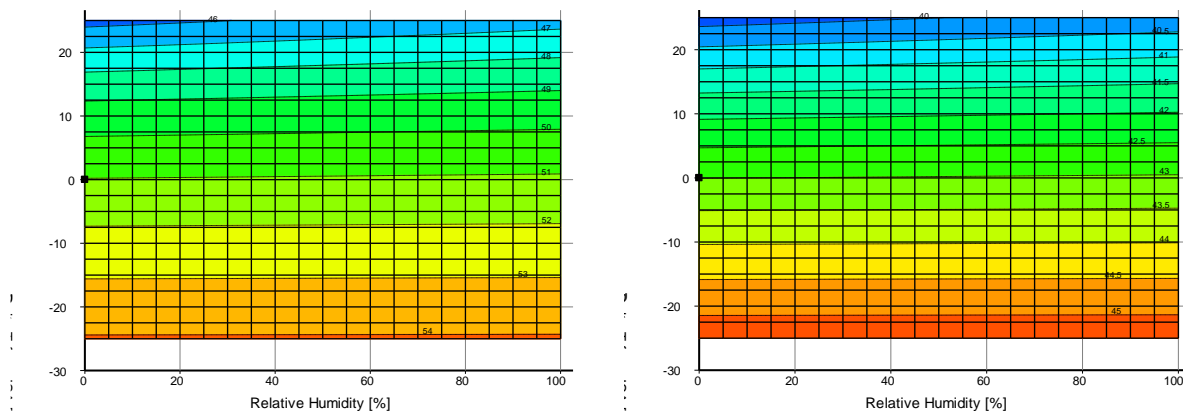
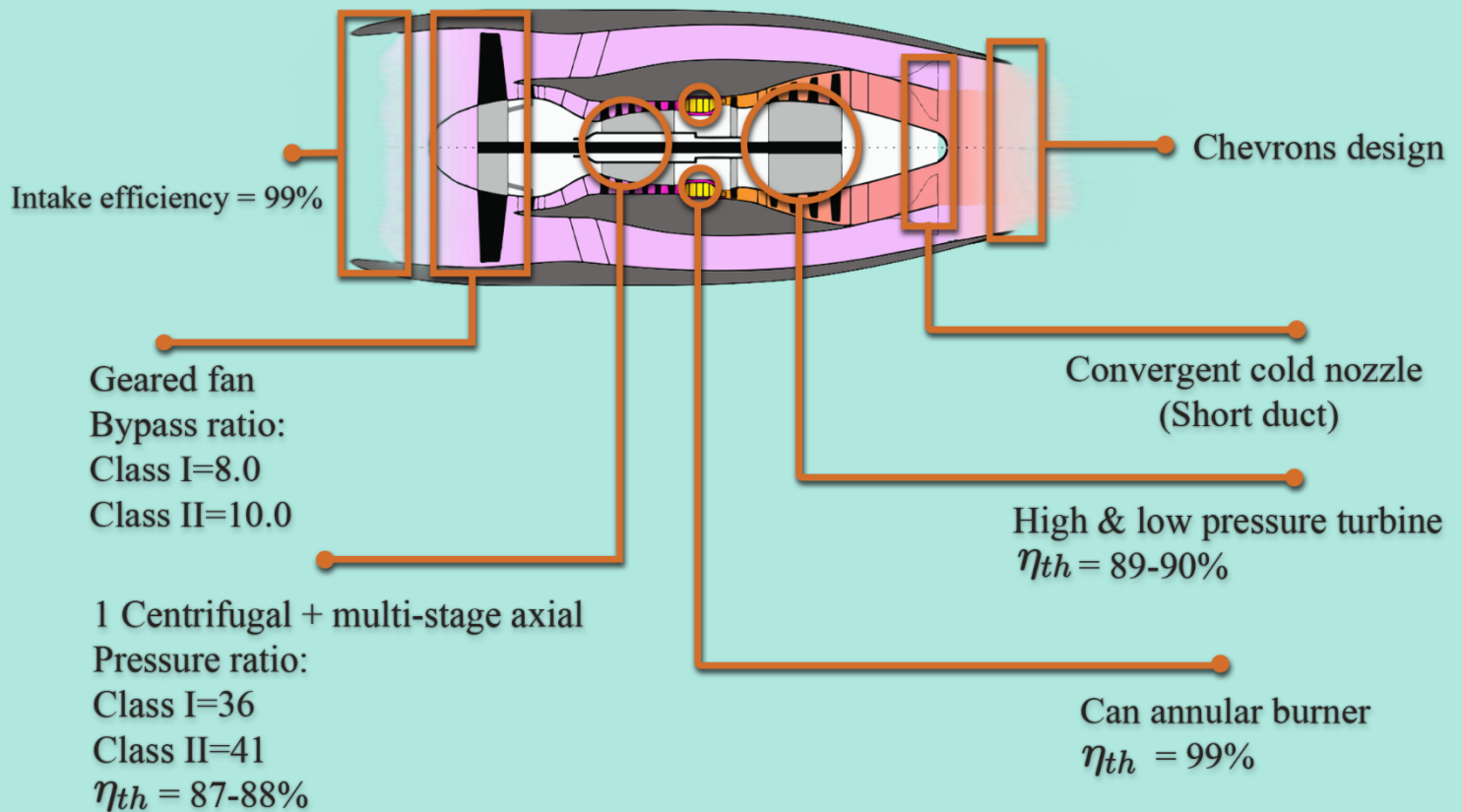


Figure 45- Diagrams of thrust in Delta T vs. relative humidity, at FL50, for the proposed engines of Chaka-76 (left) and Chaka-50 (right)

Chaka MRJ Powerplant



Main features:

- Next generation of small to medium turbofan engines
- Project start time at 2022
- Proposed entry in-service time 2030
- Accessible TRL and MRL
- Capable of high altitude and speed flights
- Higher engine core efficiency
- Less specific NOx (Eco-friendly)
- Compatible with sustainable aviation fuels (SAFs)
- Less generated noise due to new nozzle design



10 Aerodynamics

In order to design the wing of Chaka MRJ family and calculate drag polar with a systematic approach, a road map was developed to follow steps respectively. Figure 46 illustrates a schematic view of the aforementioned.

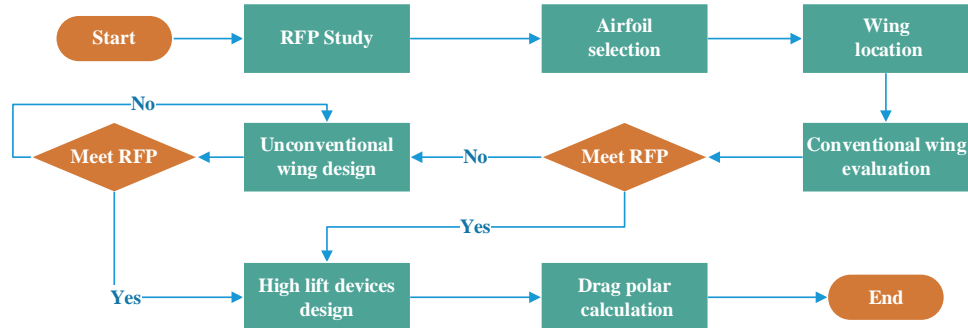


Figure 46- Aerodynamic procedural road map

10.1 RFP Study

The first step in order to design the wing configuration is to determine requirements, constraints, and priorities defined by the RFP in this regard. In accordance with the preliminary design phase, the following points are identified:

- Wingspan should not exceed 36 m
- Target cruise Mach number is 0.8

10.2 Airfoil Selection

Due to the high speed experienced while flying at high subsonic and near transonic regimes, shock waves are formed on the wing, bringing about a significant rise in drag force and decrease in lift force. Using supercritical airfoils, in which the formation of shock waves is delayed, will diminish such unwanted phenomena, allowing for flights at higher near-to-transonic regimes [52, 53]. According to the literature [54-57], the wings of the competitive RJs are also designed by using of supercritical airfoils. Consequently, the team decided to use supercritical airfoils in the Chaka MRJ family's wing design. The Airfoilttools [58] is used to conduct preliminary analyses on numerous supercritical airfoils in constant Re. Lastly, three of the most promising airfoils were chosen, as shown in Table 40.

Table 40- Primary characteristics of supercritical airfoil candidates

Airfoil	t/c	t/c location	Max. camber	Max. camber location
NASA SC(2)-712	12%	37% of chord	2.2%	81% of chord
NYU-GRUMMAN-K1	11.6%	33% of chord	1.9%	75% of chord
NPU-LSC-72614	12.7%	43% of chord	1.8%	80.1% of chord

Due to limitations of the available airfoil analysis tools in terms of Reynolds number, the three down-selected airfoils were numerically analyzed, using the Fluent software, in the cruise conditions of Mach number 0.8 and 35,000 ft elevation, and their primary aerodynamic diagrams were excerpted in Figure 47.

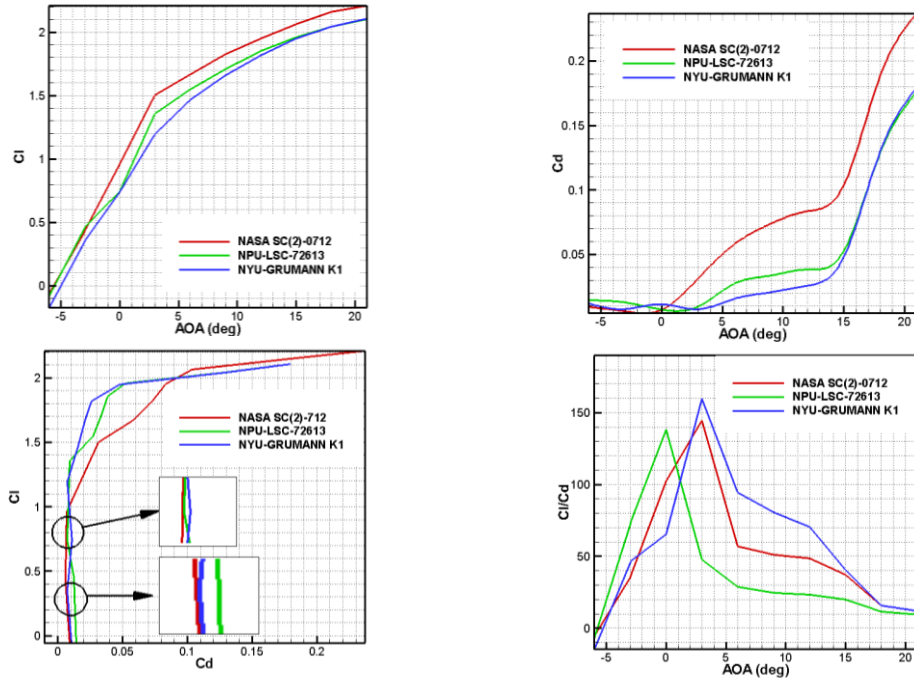


Figure 47- Lift coefficient versus AOA (left-up), drag coefficient versus AOA (right-up), lift coefficient versus drag coefficient (left-down), and L/D versus AOA (right-down) for the three candidate Airfoils

Not only were the primary aerodynamic diagrams of the three airfoils examined, but also other important functional variables of them were put under scrutiny. Figure 48 provides graphs illustrating the distributions of pressure coefficient, surface acoustic power level, and surface Mach number on the surface of the candidate airfoils.

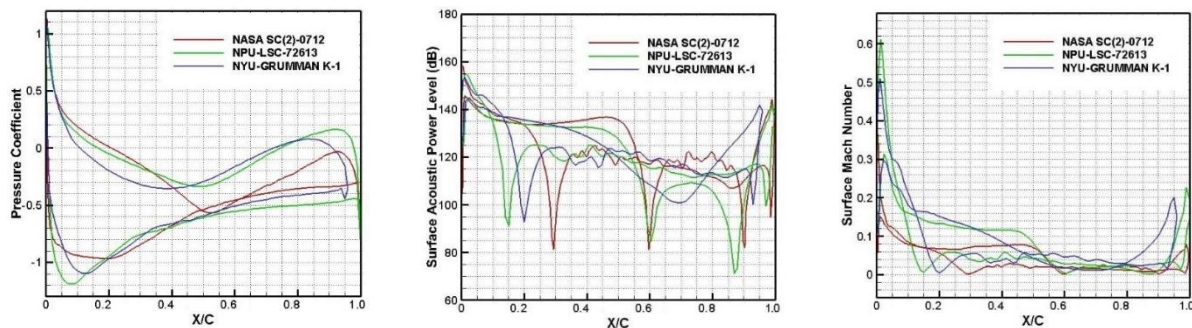


Figure 48- Diagrams of pressure coefficient (left), acoustic power level (middle), and Mach number (right) for the candidate airfoils

Inspecting the candidate airfoils for their performance characteristics, the team formed Table 41 in order to weigh all the parameters collectively. In the tradeoff process, the intended objectives were as Table 41:

Table 41- Airfoil decision matrix (weighed and normalized scores)

Airfoil	lower c_{d0}	Lower c_{dmin}	Proper c_{li}	Higher c_{lmax}	Higher α_{stall}	Higher $(L/D)_{Max}$	Mach Number	c_p	Surface Acoustic Power	Total Score
NASA SC(2)-0712	10	11	10	15	12	15.5	8	9	7	97.5
NYU-GRUMMAN-K1	9	10	9.5	13	11	15	7	5.5	6.5	86.5
NPU-LSC-72614	10.5	10.5	11	13	11	17	6.5	7	6	92.5
Weight (%)	10	11	11	15	12	17	8	9	7	100



According to Table 41, the NASA SC (2) -0712 airfoil gains the highest score, and, therefore, is selected for the wing and truss design of Chaka MRJ family.

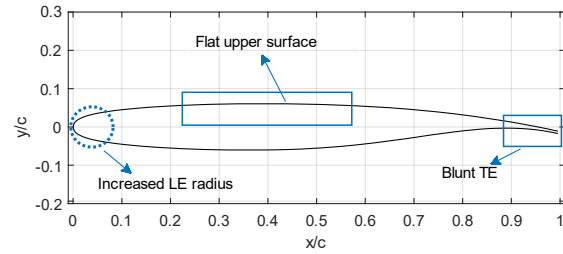


Figure 49- NASA SC (2) -0712 airfoil

10.3 Wing Location

A trade-off study between three wing configurations including low-wing, mid-wing, and high-wing happened. Table 42 provides the summary presenting the advantages and disadvantages of each configuration. The low-wing design is selected due to wing and tail weight reduction of aircraft which is a necessary to reduce block fuel per seat.

Table 42- Wing location trade-off summary [21, 33, 59]

Low-Wing	Advantages	<ul style="list-style-type: none"> • Short and lighter landing gear (wing-mounted) • Better aircraft take-off performance (compared with high-wing) • Lighter aircraft (compared with high-wing) • Less frontal area • Higher lateral control (compared with high-wing) • Lighter tail (compared with high-wing)
	Disadvantages	<ul style="list-style-type: none"> • Poor visibility for some passengers • Less lift • Longer landing run
Mid-Wing	Advantages	<ul style="list-style-type: none"> • Good passenger visibility • Aerodynamically streamlined
	Disadvantages	<ul style="list-style-type: none"> • Heavier aircraft structure • Expensive (compared with high-wing and low-wing) • Long and heavy landing gear
High-Wing	Advantages	<ul style="list-style-type: none"> • More space inside the fuselage for cargo • Saving the wing from high-temperature exit gases • Produce more lift force (compared with mid-wing and low-wing) • Lower stall speed
	Disadvantages	<ul style="list-style-type: none"> • Long and heavy landing gear • More frontal area • Pilot has less higher-than-horizon view • Heavier aircraft • Weaker aircraft lateral control

10.4 Wing Geometry

In accordance with the preliminary design section, a considerable portion of the 20% reduction in terms of block fuel per seat could be achieved by improving the aircraft's aerodynamic performance, i.e., increasing the L/D of the aircraft to 25 at cruising condition. Examining the competitive aircraft's wing layout, the aerodynamic team observed that obtaining the overall L/D of 25 at cruising condition would be impossible if conventional wing design were



utilized. In order to increase the overall L/D ratio, it is vital that the overall drag coefficient be reduced as much as possible while the overall lift coefficient be increased.

According to Equation 5, decreasing the wing’s reference area and increasing the wingspan are mainly the two techniques used for increasing the aspect ratio. According to the wing reference area output by the preliminary design phase and also by increasing the wingspan considerably, the high aspect ratio required could be achieved. Figure 50 illustrates the effect of increasing the wing’s aspect ratio on the overall L/D at different AOAs.

$$\text{Equation 5: } AR = \frac{b^2}{S_{ref}}$$

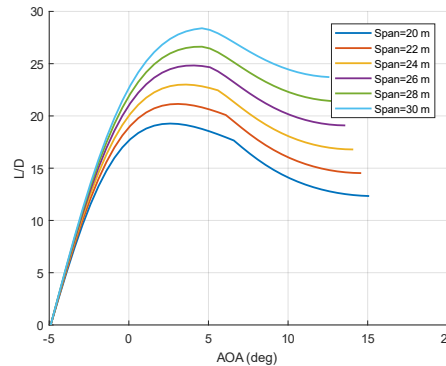


Figure 50- L/D versus AOA, while increasing the wingspan and keeping the wing reference area constant

As Figure 50, Increasing the wing’s aspect ratio at high levels will reduce the wing’s chord line significantly. This will necessitate greater concentration on the structural integrity and vibrational considerations of the wing. In order to strengthen the structure of a wing possessing very high aspect ratio, the idea of designing a truss-braced wing is utilized, which increases the wing’s reliability in terms of structural integrity and modal vibrations. According to the literature in case of truss-braced wings [9, 60, 61], such configuration allows for safe implementation of very high aspect ratio wings, and it is a promising design for procuring overall L/Ds of even 30.

The principal approach to designing the Chaka truss-braced wing has been using numerical simulations. First of all, an initial design of the truss was carried out, using the NASA SC(2)-0712 airfoil, and its aerodynamic performance under cruise conditions was investigated by the Fluent software. Figure 51 demonstrates the static pressure contour on the truss surface and also the streamlines around it at Mach number 0.8 and an altitude of 35,000 feet.

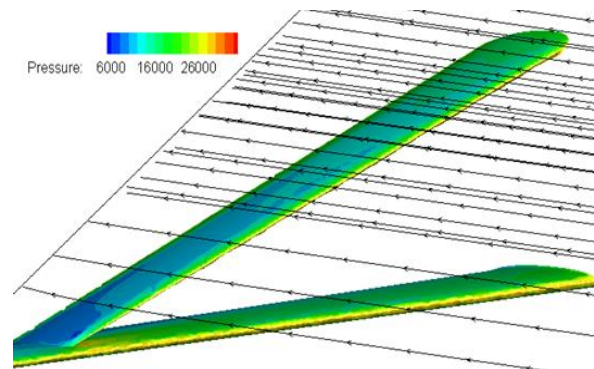


Figure 51- The flow around truss geometry, with NASA SC(2)-0712 airfoil and under cruise conditions

As shown in Figure 51, the pressure contour of the truss is similar to that of the main wing, and the streamlines closed to it are laminar. The results showed that the truss could be utilized as a lift generator component; hence, after iterative simulations, the team decided to use 23% and 31% of the S_{ref} to design the truss of the Chaka-50 and -76,



respectively. Then, in order to design the wing and truss, the equations in [33] were used to achieve the desired L/D . Figure 52 shows the effect of the using the truss on the wing L/D .

In order to reduce the wing wave drag, appropriate wing sweep angle in accordance with the flight regime must be determined. The reason is that increasing the sweep angle will increase the M_{DD} delaying compressibility effects.

Equation 6, linking the related variables, is used for finding suitable quarter chord sweep angle [62]. Figure 53 provides the optimal value of the quarter chord sweep angle in terms of different values of thickness ratio and critical Mach number based on Equation 6. The optimal wing design point is shown in Figure 53, and the amount of quarter chord sweep angle required for the design is 28 degrees.

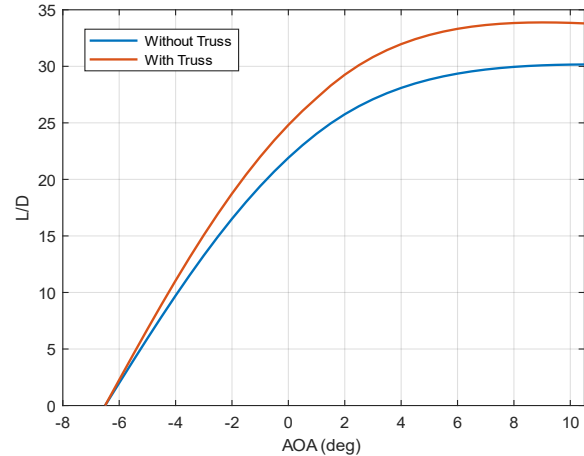


Figure 52- The effect of the truss on the wing's overall L/D in constant S_{ref}

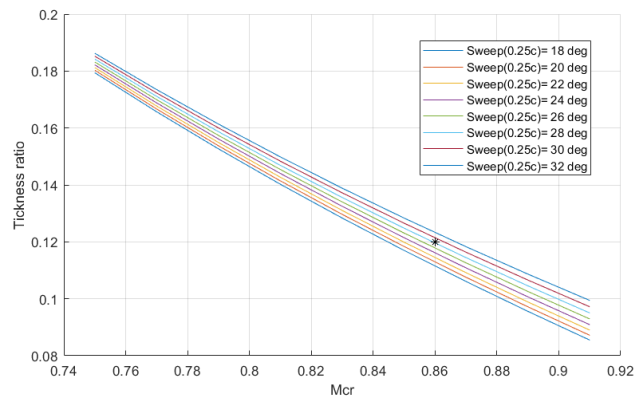


Figure 53- Optimal value of the sweep angle in terms of different thickness ratios and critical Mach numbers

$$\text{Equation 6: } \frac{t}{c} = 0.30 \cos \Lambda_{\frac{1}{4}c} \left\{ \left[1 - \left\{ \frac{5 + M_{DD,eff}^2}{5 + (K_M - 0.25 c_{L,CR})^2} \right\}^{3.5} \right] \sqrt{\frac{1 - M_{DD,eff}^2}{M_{DD,eff}^2}} \right\}^{2/3}$$

Where: $M_{DD,eff} = M_{DD} \sqrt{\cos \Lambda_{\frac{1}{4}c}}$ $K_M = 1.12$ to 1.15 , for supercritical airfoils

Table 43 provides the geometric details of the Chaka MRJ family's wing configuration. Geometric parameters are calculated based on [33]. According to the table, the wings of both aircraft meet the ICAO code C standard.

Table 43- Wing and truss geometric features for the Chaka MRJ family

Wing geometry			Truss geometry		
Parameter	Chaka-50	Chaka-76	Parameter	Chaka-50	Chaka-76
C_{root} (ft)	5.84	7.09	C_{root} (ft)	4.06	6.79
C_{tip} (ft)	2.01	2.43	C_{tip} (ft)	1.25	2.01
Taper ratio (C_{tip}/C_{root})	0.34	0.34	Taper ratio (C_{tip}/C_{root})	0.31	0.29
Span (ft)	91.86	112.21	Span (ft)	20.18	28.18
S_{ref} (ft ²)	359.51	533.46	S (ft ²)	107.64	247.57



AR	23.45	23.6
Dihedral (deg)	6.5	6.5
Wing setting angle (deg)	3	3
Twist angle (deg)	-3	-3

10.5 High Lift Devices

In terms of flap design, the difference between $C_{L, Take-off}$ and $C_{L, landing}$ with the wing's clean $C_{L,max}$ is used. The difference must be compensated for by adding flaps to the wing's structure and enhancing its required performance. Experiencing flows with high-Reynolds numbers at take-off and landing conditions for the sea level +18 °F and FL50 +18 °F, the team conducted numerical simulations using the Fluent to obtain the behavior of the wing's $C_L - \alpha$ diagram at these phases. The results showed that there exists a close resemblance in terms of the required $C_{L,max}$ for both phases. Table 44 demonstrates the available and required $C_{L,max}$ values, as well as the difference between them in take-off and landing at sea level +18 °F and FL50 +18 °F for the Chaka MRJ family.

Table 44- $C_{L,max}$ increase required to fulfill take-off and landing

Condition	Take-off @ sea level +18 °F	Landing @ sea level+18 °F	Take-off @ FL50+18 °F	Landing @ FL50+18 °F
$C_{L,max, clean}$	1.66	1.66	1.64	1.64
$C_{L,max, required}$	2.73	2.94	2.7	2.9
$\Delta C_{L,max}$	1.07	1.28	1.06	1.26

According to Table 44, The required $\Delta C_{L,max}$ is considerable; therefore, both leading and trailing edge HLDs will be used. The relationship between geometry and flap type with $\Delta C_{L,max}$ including inboard and outboard HLD is shown in Equation 7 [63].

$$\text{Equation 7: } \Delta C_{L,max} = 0.9(\sum \Delta c_{l_{flap,i}} * \frac{S_{flap,i}}{S_{ref}} * \cos(\Lambda_{hingeline,i}) + \sum \Delta c_{l_{slat,i}} * \frac{S_{slat,i}}{S_{ref}} * \cos(\Lambda_{\frac{1}{4}i}))$$

The primary constraints on maximizing the area of the flaps are maintaining proper distances from the fuselage, the wingtip, and the truss installation location.

Table 45 illustrates the design details of HLDs for the Chaka MRJ family. Figure 54 shows the $C_L - \alpha$ diagrams of the Chaka MRJ family at takeoff, landing, and cruise conditions, on which principal performance characteristics are superimposed.

Table 45- Geometric specifications of high-lift devices

Parameter	Chaka-50		Chaka-76	
	LE Device	TE Device	LE Device	TE Device
Type	Slats	Single-Slotted Flaps	Slats	Single-Slotted Flaps
Area (ft ²)	300.50	233.80	448.40	334.80
S/S _{ref} ratio	0.13	0.12	0.12	0.13
Span proportion	0.84	0.57	0.80	0.50

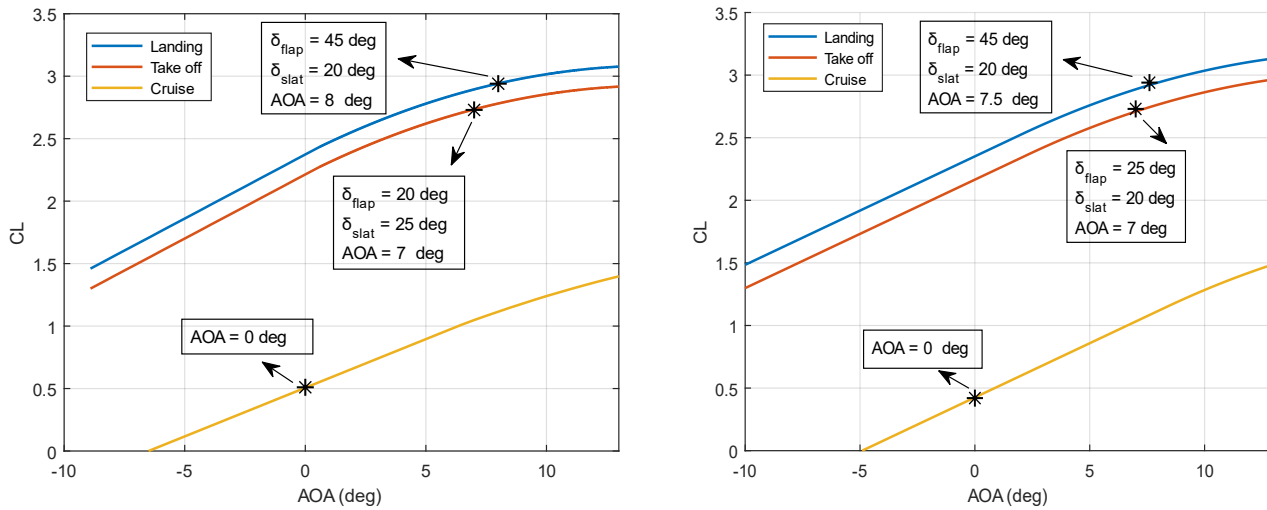


Figure 54- CL versus angle of attack diagrams for Chaka-50 (left) and Chaka-76 (right)

Figure 55 demonstrates the top view and geometric properties of the Chaka MRJ family wings.

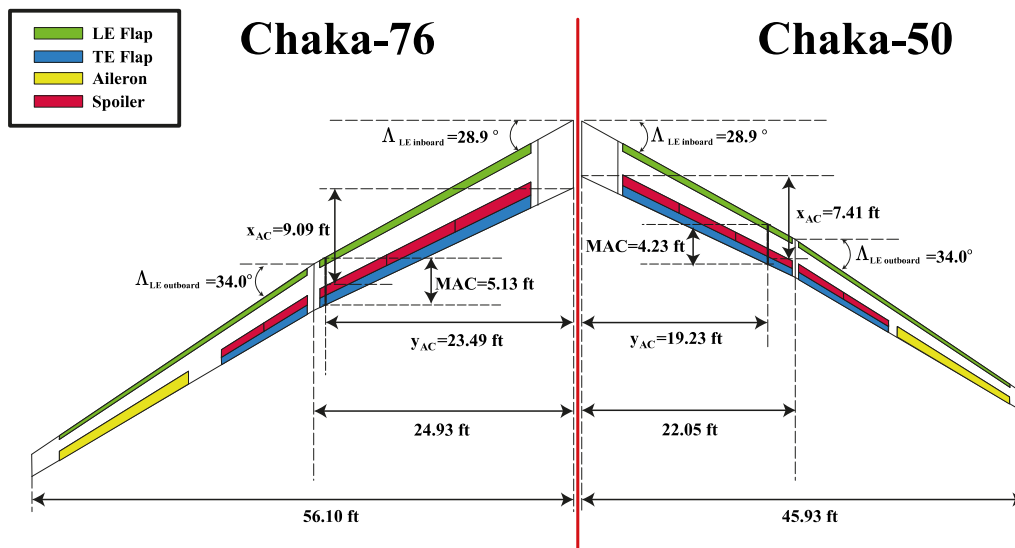


Figure 55- Geometric properties of the Chaka MRJ family wings

10.6 Drag Polar

In order to evaluate the L/D at different flight phases, it is necessary to calculate the aircraft's drag coefficient at each phase. The drag force is calculated separately at low and high speeds, with the essential parts being Profile Drag and Induced Drag. This section's calculations are based on component buildup formulation as Equation 8[33].

$$\text{Equation 8: } C_{D0} = \frac{\sum C_{f_{com}} FF_{com} Q_{com} S_{wet_{com}}}{S_{ref}} + C_{D_{misc}} + C_{D_{L\&P}}$$

When the results output by the flow simulation around Chaka's airfoil-shaped fuselage at various AOAs were compared to those of competitive aircraft fuselages, it was discovered that this design reduced the drag coefficient.



Also, the wing design with high span and low thickness decreased the drag coefficient. This variable is calculated for each phase due to the profile drag changes, and the addition of flaps and landing gear in the takeoff and landing.

Furthermore, because the truss, like the wings, generates lift, its induced drag must be calculated. The induced drag is calculated based on Raymer methodology [33]. Table 46 and 47 demonstrate take-off, landing, and cruise drag build-up for various flight phases and also their corresponding drag equations.

Table 46- Take-off, landing, and cruise drag build-up

Drag component		Chaka-50					Chaka-76				
profile Drag	Component	Take-off Sea level	Take-off FL50	Cruise	Landing Sea level	Landing FL50	Take-off Sea level	Take-off FL50	Cruise	Landing Sea level	Landing FL50
	Fuselage	0.002	0.002	0.0022	0.002	0.002	0.0019	0.0019	0.0021	0.0019	0.0019
	Wing	0.0023	0.0024	0.0026	0.0023	0.0024	0.0015	0.0016	0.0026	0.0015	0.0016
	Truss	0.0012	0.0012	0.0014	0.0012	0.0012	0.0016	0.0016	0.0018	0.0016	0.0016
	Vertical Tail	0.0009	0.0009	0.0012	0.009	0.009	0.0011	0.0011	0.0012	0.0011	0.0011
	Horizontal Tail	0.001	0.001	0.0013	0.001	0.001	0.0012	0.0012	0.0013	0.0012	0.0012
	Nacelle	0.0033	0.0033	0.0027	0.0033	0.0033	0.0027	0.0027	0.0024	0.0027	0.0027
	Upsweep	0.0017	0.0017	0.0017	0.0017	0.0017	0.0017	0.0017	0.0017	0.0017	0.0017
	Landing gear	0.0105	0.0105	0	0.0105	0.0105	0.0105	0.0105	0	0.0105	0.0105
	L&P	0.0017	0.0017	0.00089	0.0017	0.0018	0.0017	0.0018	0.0009	0.0018	0.0018
Total	0.0246	0.0247	0.01399	0.0327	0.0329	0.0239	0.0241	0.014	0.024	0.0241	
C_D trim	0.0095	0.0095	0.0006	0.0135	0.0135	0.0098	0.0098	0.0006	0.0139	0.0139	
C_D wave	0	0	0.0008	0	0	0	0	0.0008	0	0	
C_D flap	0.006	0.006	0	0.0211	0.0211	0.0076	0.0076	0	0.0334	0.0334	
C_D total	0.0401	0.0402	0.01539	0.0673	0.0675	0.0413	0.0415	0.0154	0.0713	0.0714	

Table 47- Drag polars for various flight phases

Flight phase	Chaka-50		Chaka-76	
	K	Drag polars	K	Drag polars
Take-off Sea level + 18°F	0.01776	$0.0401 + K \cdot C_L^2$	0.01778	$0.0413 + K \cdot C_L^2$
Take-off FL50 + 18°F	0.01776	$0.0402 + K \cdot C_L^2$	0.01778	$0.0415 + K \cdot C_L^2$
Cruise	0.01838	$0.015 + K \cdot C_L^2$	0.0183	$0.015 + K \cdot C_L^2$
Landing Sea level + 18°F	0.01776	$0.0673 + K \cdot C_L^2$	0.01782	$0.0713 + K \cdot C_L^2$
Landing FL50+ 18°F	0.01776	$0.0675 + K \cdot C_L^2$	0.01782	$0.0714 + K \cdot C_L^2$

In Figures 56 and 57, graphs show the drag polar, C_L vs. AOA, L/D vs. AOA, and L/D vs. C_L , respectively, at cruise for the Chaka MRJ family.

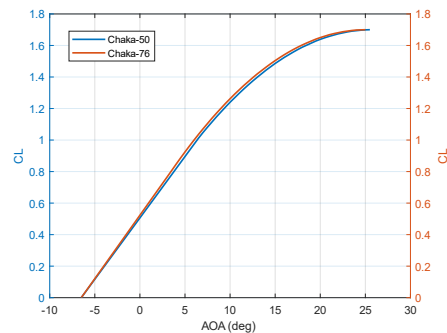
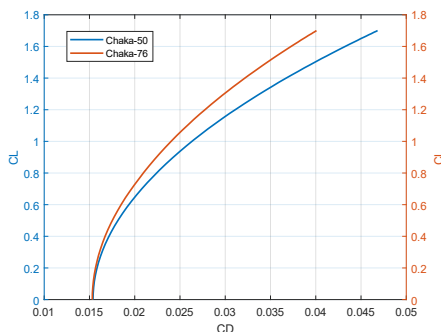


Figure 56-Drag polar (left), C_L vs. AOA (right)

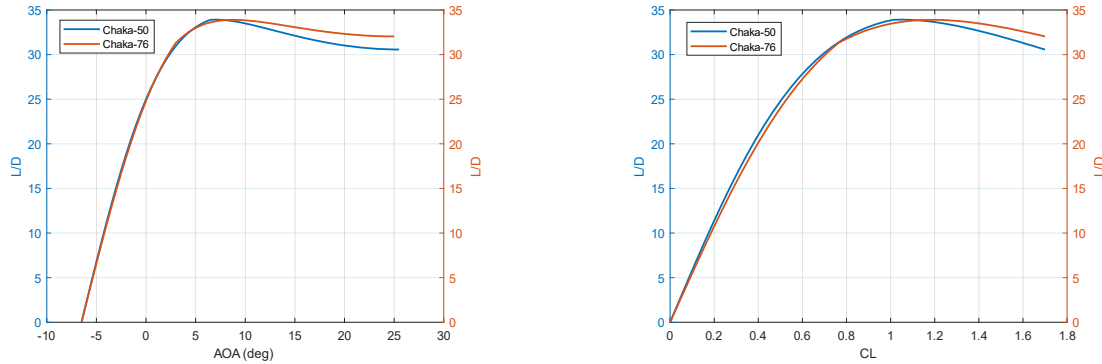


Figure 57- L/D vs. AOA (left), and L/D vs. C_L (right), at cruise for the Chaka MRJ family

11 Empennage and Control Surfaces Design

In this section, the design procedure of the empennage and control surfaces is presented.

11.1 Empennage Design

In this section, preponderant characteristics of the design of horizontal and vertical tails for the Chaka MRJ family will be delineated. The tail surfaces have undergone numerous iterative design loops so that they will be able to carry out the three primary functions of Trim, Stability, and Control properly in every flight phase the two aircraft are going through. It is worthwhile mentioning that the aircraft's trim requirement has been the principal criterion based on which the design equations have been derived and utilized [21].

Using systems engineering approach, the S&C team opted for the general configuration of “one aft horizontal tail, one aft vertical tail”. The selected configuration has several sub-configurations, namely conventional, T-shape, cruciform, etc. Using weighing factors, the team narrowed down the options to the first two sub-configurations mentioned above. Between the two, the T-tail was finally chosen thanks to the following advantages:

- Being out of the wing wake, wing downwash, wing vortices and engine exit flow regions
- Possessing enhanced horizontal tail efficiency and a safer structure
- Experiencing less tail vibration and buffet
- Possessing the end-plate effect [21]

There are some disadvantages originated by the above choice, namely heftier vertical tail structure and, more importantly, deep stall, which need to be taken into consideration. In terms of the structure, sufficient strengthening and weight capacity is provided by the structures team, as is shown in the structural section. As regards the deep stall, the horizontal tail's span is extended considerably beyond the nacelles.



Following the empennage design procedure, using the methodology and equations presented in [21], the S&C team could design the Chaka-50 and -76's empennages with the main characteristics demonstrated in Table 48.

In terms of tail installation, the horizontal tail will be fixed. This is because a fixed horizontal tail is much safer, lighter, cheaper, and structurally less demanding to design compared to adjustable or all-moving tails [21].

Regarding tail airfoil section, a symmetrical section capable of generating the calculated lift while producing minimum drag and pitching moment with a substantially wide range of AOA is ideal. It should be noted that the tail's section must be clean of compressibility effects; hence, the section must be thinner than the wing's airfoil section [21].

Table 48- The main characteristics of the Chaka MRJ family empennage

Parameter	Chaka-50		Chaka-76	
	Horizontal tail	Vertical tail	Horizontal tail	Vertical tail
Volume coefficient	0.9	0.07	0.86	0.09
Optimum tail arm (ft)	39.37	39.37	41.99	41.99
Planform area (ft ²)	94.93	98.16	159.30	164.68
Airfoil section	NACA 0009			
LE sweep angle (deg)	41	42	40	41
Dihedral angle (deg)	0	-	0	-
AR	5.2	1.5	5.25	1.55
Taper ratio	0.45	0.6	0.4	0.52
Tail incidence angle (deg)	-1.72	0	-2.08	0
Span (ft)	22.17	12.14	28.92	15.97
MAC (ft)	4.26	8.08	5.51	10.30
Root chord (ft)	5.62	9.91	7.41	13.12
Tip chord (ft)	2.52	5.94	2.95	6.82

The horizontal tail is influenced by the wing through downwash, wake, and trailing vortices. The most significant consideration in terms of the location of the horizontal tail with respect to the wing is the prevention of deep stall. The criterion is checked in the manner that when the wing stall happens, the horizontal tail must not be in the wing's wake region [21].

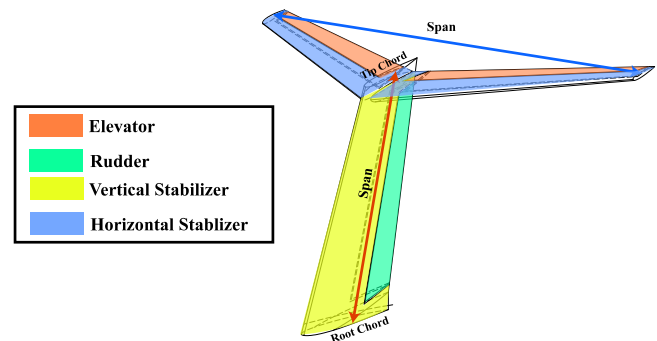


Figure 58- Tail Configuration

Should the aircraft stall and enter a spin, the vertical tail must be able to generate sufficient yawing moment in order to stop the autorotation. The wake region associated with the horizontal tail is considered to lie within two lines: the first line has an orientation of 30 degrees and is drawn at the horizontal tail's trailing edge while the second has an orientation of 60 degrees and is drawn at the horizontal tail's leading edge [21]. Exercising the experimental rule



delineated above for the considered horizontal and vertical tail locations of the Chaka-50 and -76, it was observed that 80% and 78% of the vertical tail's reference area was out of the horizontal tail's wake region for the Chaka-50 and -76, respectively; hence, the spin recovery criterion is satisfied for the Chaka family.

Figures 59 and 60 demonstrate the satisfaction of deep stall and spin recovery criteria, respectively, for the Chaka MRJ family.

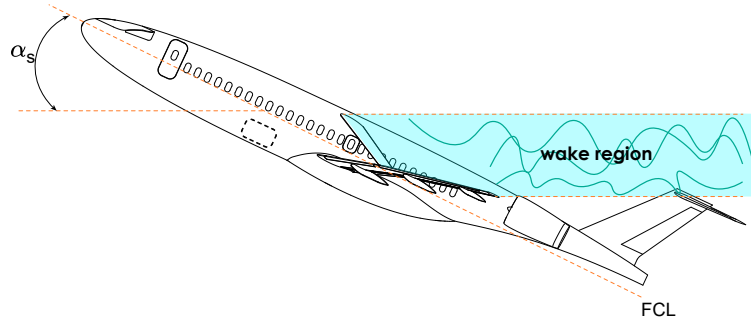


Figure 59- Satisfaction of deep stall criterion for the Chaka family

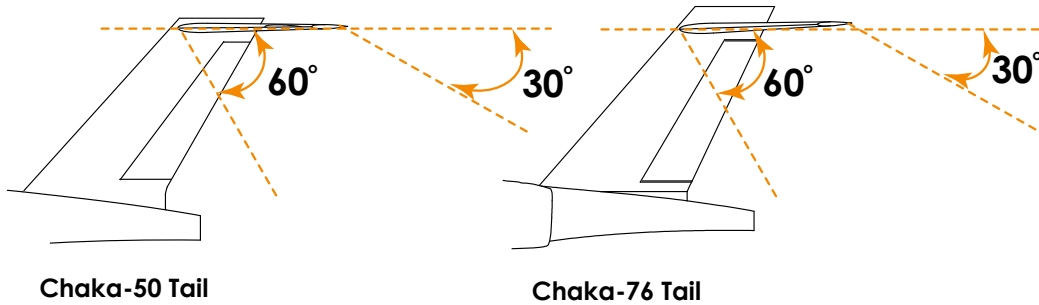


Figure 60- Satisfaction of spin recovery criterion for the Chaka-50 (left) and Chaka-76 (right)

In order to examine if the designed vertical tails of the Chaka-50 and -76 are capable of satisfying the static directional stability criterion ($C_{n,\beta}$), directional X-plot method can be utilized. Figures 61 and 62, in the following, depict directional X-plot diagrams on which the points pertaining to the Chaka-50 and -76's tail reference areas (in ft^2) and their corresponding $C_{n,\beta}$ are superimposed.

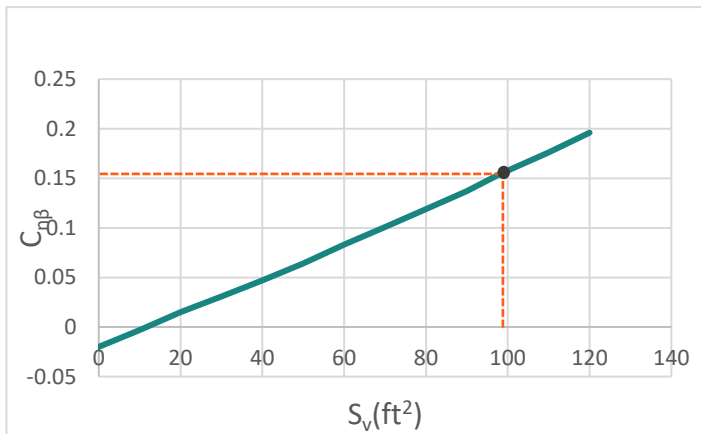


Figure 62- Satisfaction of static directional stability for the Chaka-50

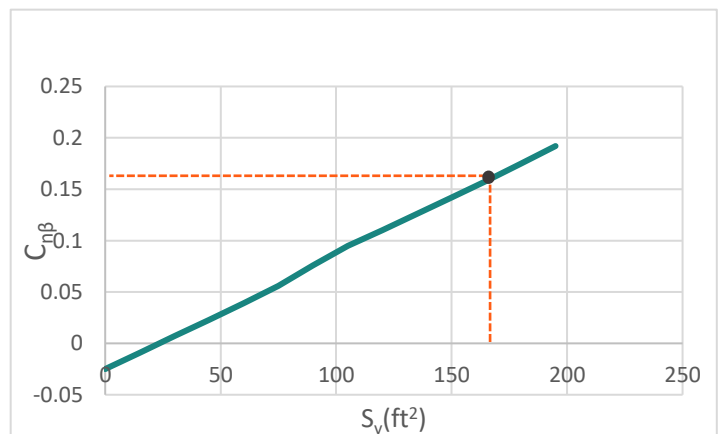


Figure 61- Satisfaction of static directional stability for the Chaka-76



As the figures demonstrate, $C_{n\beta}$ for the Chaka-50 and -76 is 0.15 and 0.159, respectively. Knowing that the typical range of $C_{n\beta}$ for directionally stable aircraft is from +0.05 to +0.4, we can observe that the designed vertical surfaces appropriately satisfy the criterion.

11.2 Control Surfaces Design

The Sadraey methodology [21] was exploited in order to design the control surfaces for the Chaka MRJ family.

Table 49 provides geometric parameters of the designed control surfaces.

Table 49- Geometric parameters of the designed control surfaces for the Chaka MRJ family

Parameter	Aileron		Elevator		Rudder	
	Chaka-50	Chaka-76	Chaka-50	Chaka-76	Chaka-50	Chaka-76
$S_{Control\ surface} / S_{ref}$	0.04	0.05	0.46	0.40	0.32	0.29
Maximum Deflection (deg)	25 (up & down)	25 (up & down)	±30	±30	±35	±35

12 Weight and Balance

12.1 Weight of Components

Having concluded the detailed design of the Chaka MRJ family’s major components, the general design team is now able to calculate the airplanes’ weights with the accuracy of approximately 90-95 % (with respect to the airplanes’ final weight measurement after production) utilizing empirical approach. The approach exploits industrial experience and detailed statistical equations and is predominantly predicated upon the components’ geometry, dimensions, and the materials to be utilized in their manufacturing procedure. The prime reference utilized in this respect is [64], and an appreciable number of calculation iterations have been carried out in order to minimize the discrepancy between the airplanes’ weights prior to and following the major components’ detailed design. Table 50, in the following, demonstrates calculated mass of the components for the Chaka-MRJ family. It is worthwhile mentioning that the impact of using composite materials in each of the components’ manufacturing has been considered in the calculations based upon the percentage use of composite materials for each component. Also, by and large, the amount of composite materials used is considerably higher in the Chaka-50 compared to the Chaka-76.

Table 50- Calculated mass of the major components, in pounds, for the Chaka MRJ family

Component	Chaka-50	Chaka-76
Wing	3337.5	7598.2
Empennage	1013.65	1900
Landing gear	1506.5	2977.5
Fuselage	4354.6	8633
Powerplant + Fuel system	6019.45	8393.75
Equipment and Instruments	7342.2	11406.9
Total	23574.08	40909.47



By comparing the calculated empty weights yielded above with the estimated empty weights used in the preliminary design phase, for the final design loop, it can be observed that the discrepancy between these figures is almost 0 and 2 percent for the Chaka-50 and Chaka-76, respectively, satisfying the “less than 3% discrepancy condition” mentioned in the preliminary design section in order to close the design loop.

12.2 Center of Gravity Calculations

Only after weights of the major components are known, will the general design team be able to implement a thorough weight and balance (W&B) analysis, greatly influencing airworthiness and performance characteristics of the two airplanes via two factors, namely center of gravity (CG), and mass moment of inertia. An airplane might experience an infinite number of loading scenarios throughout its operational lifetime; hence, it would be impossible to incorporate the gamut of loading scenarios in the calculation procedure.

There are four principal scenarios to be considered:

- 1) Passengers, payload, and fuel are all present
- 2) Passengers and payload are present, but fuel is absent
- 3) Fuel is present, but passengers and payload are absent
- 4) Passengers, payload, and fuel are all absent

Additionally, in accordance with the systems engineering approach, in [21], a technique is developed using the laws governing the aircraft’s CG motion owing to diverse factors. These laws are as follows:

1. The motion of moving elements will cause the aircraft’s CG to move accordingly, but at a smaller rate
2. The aircraft’s CG will move farther from an element in absentia
3. The aircraft’s CG will move farther from a lighter element
4. As long as being consumed, the fuel causes the aircraft’s overall CG to move farther with respect to its CG

In order for the technique to be employed, the term “removable load” needs to be explicated. A removable load could be best defined as being any payload or unpaid load which can be removed from an aircraft while the aircraft is still capable of flying safely. It comprises payload, fuel, and the entire unpaid loads except for one pilot.

Having made use of both approaches, [21, 64], the general design team deduced that, for each airplane, two out of the four scenarios of the [64] are of more criticality. Hence, in the following, only the results procured by the approach of [21] are presented.

Table 51 demonstrates the output of the four scenarios for the Chaka-50 and -76, respectively. It is important to mention that the reported CG locations are measured and calculated along the airplane’s X-axis of the body coordinate system and with respect to the airplane’s nose. Then, they are nondimensionalized in terms of the wing’s MAC. For



the 2nd and 4th scenarios, in which there is no fuel in the airplane, and, thus, the airplane cannot be airborne, only the normal CG location is reported.

Table 51- X_{CG} locations with respect to the airplane’s nose and nondimensionalized by wing MAC for the Chaka MRJ family

Chaka-50			Chaka-76		
Scenario 1	In Feet	Nondimensionalized by wing MAC	Scenario 1	In Feet	Nondimensionalized by wing MAC
X_{CG} aft	48.52	0.1475	X_{CG} aft	59.92	0.1532
X_{CG} normal	48.17	0.0648	X_{CG} normal	59.24	0.01345
X_{CG} forward	47.60	-0.07	X_{CG} forward	58.57	-0.1249
CG range	0.92	0.2175	CG range	1.35	0.278
Scenario 2	In Feet	Nondimensionalized by wing MAC	Scenario 2	In Feet	Nondimensionalized by wing MAC
X_{CG} normal	47.60	-0.07	X_{CG} normal	58.56	-0.0969
Scenario 3	In Feet	Nondimensionalized by wing MAC	Scenario 3	In Feet	Nondimensionalized by wing MAC
X_{CG} aft	49.34	0.34	X_{CG} aft	61.16	0.41
X_{CG} normal	48.70	0.19	X_{CG} normal	59.98	0.1804
X_{CG} forward	48.13	0.0556	X_{CG} forward	58.91	-0.0282
CG range	1.21	0.2844	CG range	2.25	0.438
Scenario 4	In Feet	Nondimensionalized by wing MAC	Scenario 4	In Feet	Nondimensionalized by wing MAC
X_{CG} normal	51.65	0.887	X_{CG} normal	63.68	0.9

As can be seen in Table 51, the most critical locations of the aft and forward CG for the Chaka-50, in terms of MAC, are 0.34 and -0.07, respectively; for the Chaka-76, the corresponding figures are 0.41 and -0.1249, respectively. Due to the uncommon nature of the designed wing’s configuration, which has a relatively small reference area and also a very high aspect ratio leading into a fairly short MAC, when the location of the Chaka aircraft’s CG is nondimensionalized based upon wing’s MAC (CG_{aft} , and $CG_{forward}$), the results differ from common aircraft to some extent. The significant point to be considered is that, for all principal scenarios, the most aft CG of the aircraft be retained forward of the main landing gear, and the most forward CG do not impose trouble while taking off; also, in all flight phases, stability and control considerations must be satisfied; which is the case as calculations in all of the corresponding sections depict. Following figures represent the aforementioned for the Chaka-50 and -76, respectively.

Figure 63 depicts CG travel diagrams of the Chaka MRJ family during flight operation at all scenarios. Figure 64 depicts CG travel diagrams of the Chaka MRJ family during flight operation at the 1st scenario. Figure 65 demonstrates the aforementioned for the 3rd scenario. The diagrams demonstrate how the CG will move along X-body axis according to the scheduled fuel burn considered for the three main fuel tanks of the two aircraft, i.e., wing tank, fuselage aft tank, and fuselage forward tank.

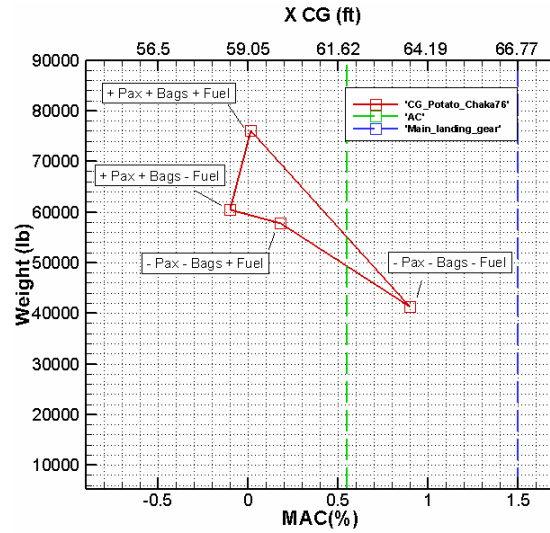
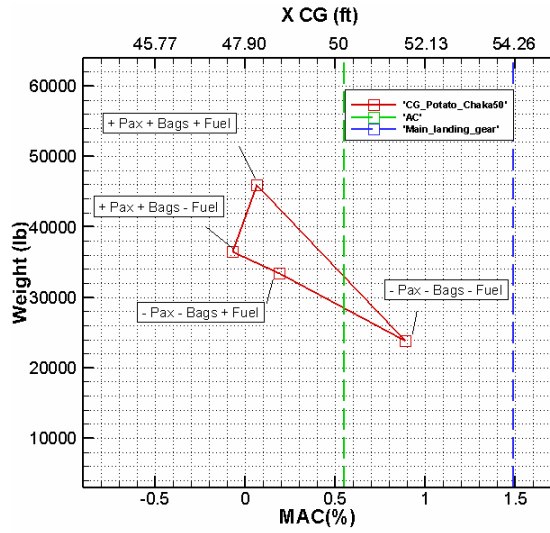


Figure 63- CG potato diagram for the Chaka-50 (left) and -76 (right) at all scenarios

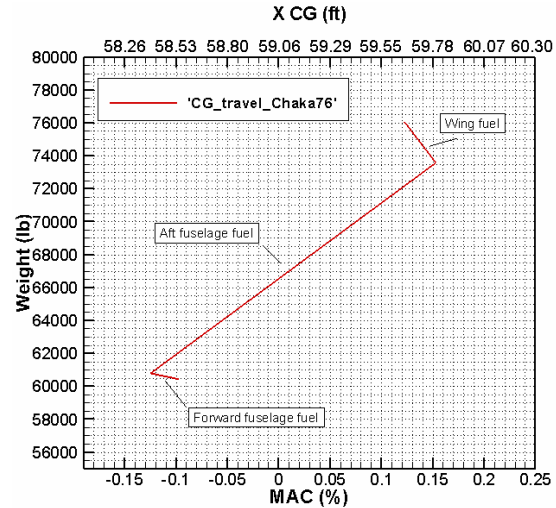
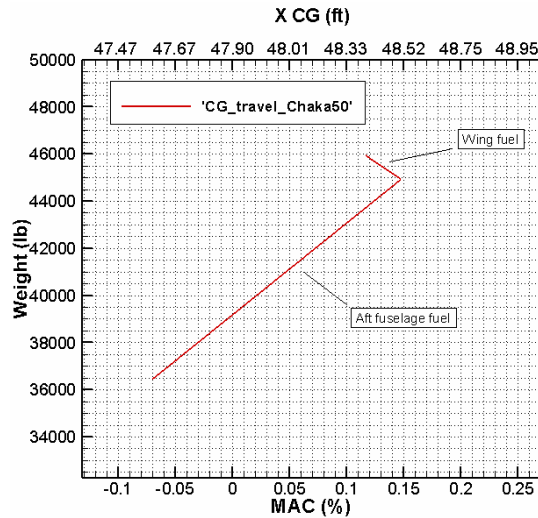


Figure 64- CG travel diagram of the Chaka-50 (left) and Chaka-76 (right) during flight operation at 1st scenario

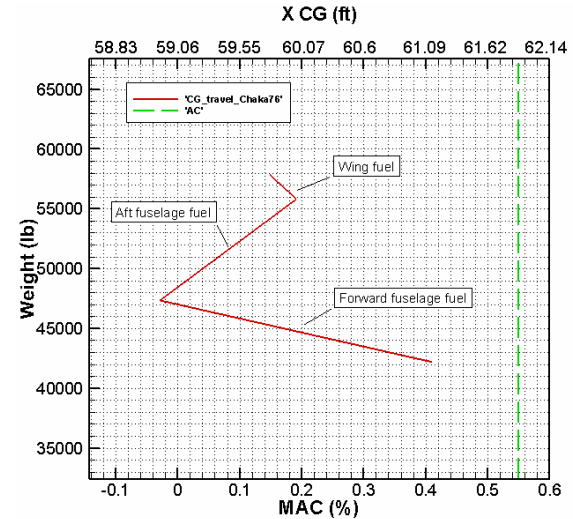
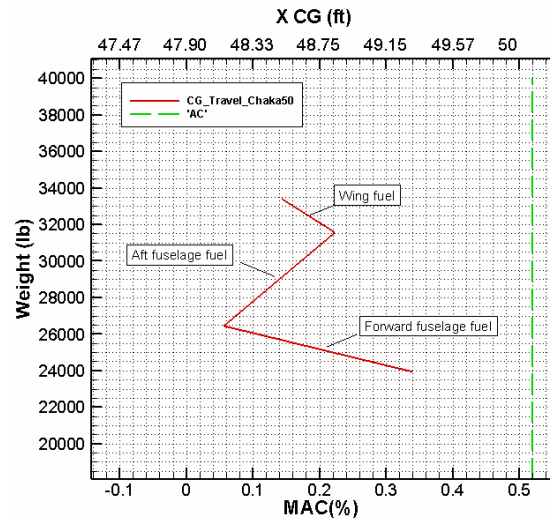


Figure 65- CG travel diagram of the Chaka-50 (left) and Chaka-76 (right) during flight operation at 3rd scenario

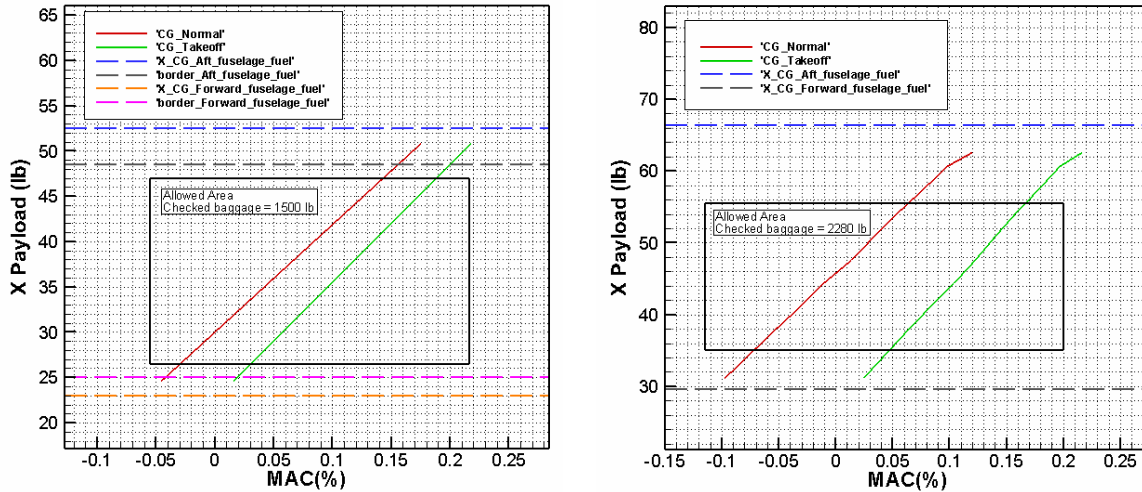


Figure 66- Normal and take-off CG point movement based on different possible payload arrangements, Chaka-50 (left) and -76 (right)

Figure 66 depicts the movement of normal CG and take-off CG point based on different possible arrangements of the payload in the cargo section of the Chaka MRJ family. Following figures depict detailed CG distribution of the Chaka-50 and -76 in terms of the 1st scenario, a significant scenario referring to the aircraft while possessing MTOW. Moreover, Tables 52 and 53 provide an overview of the details in this regard for the Chaka MRJ family, as an example.

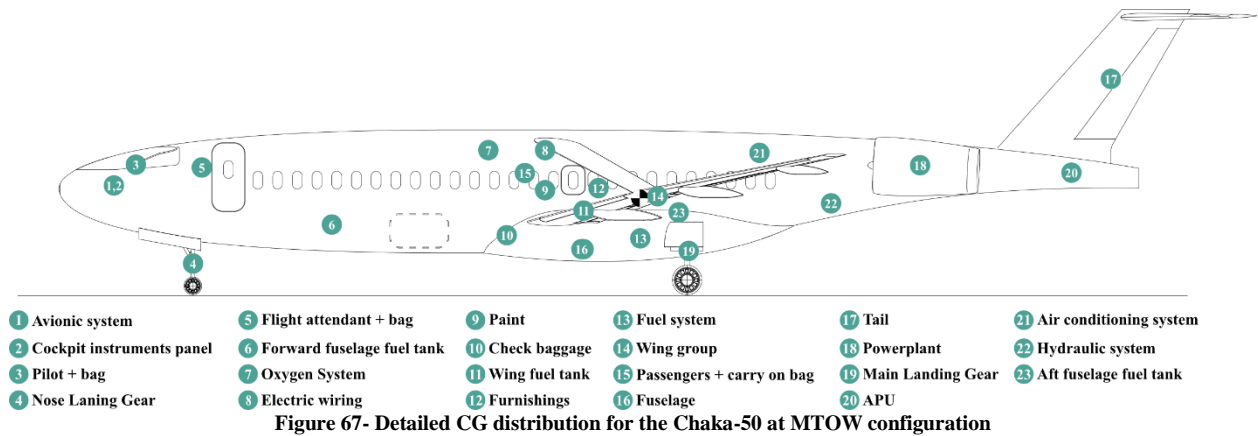


Figure 67- Detailed CG distribution for the Chaka-50 at MTOW configuration

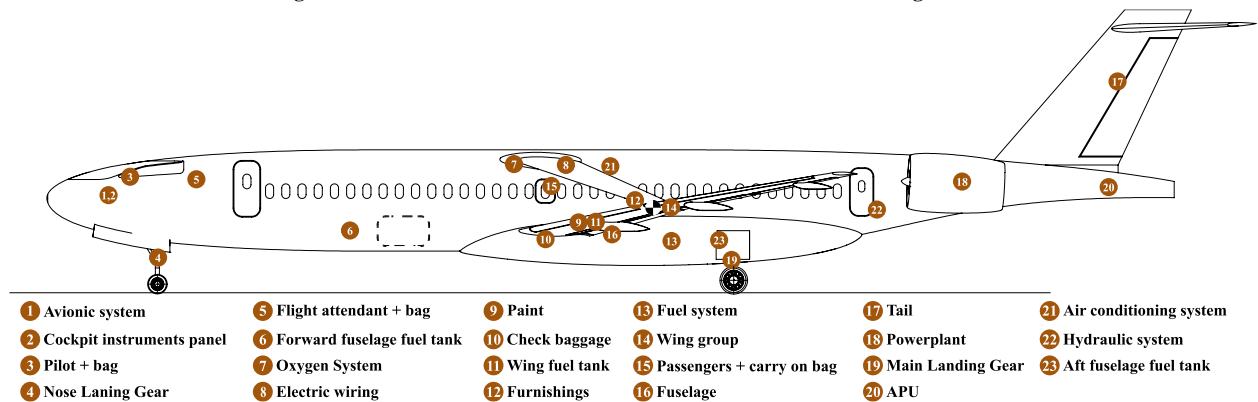
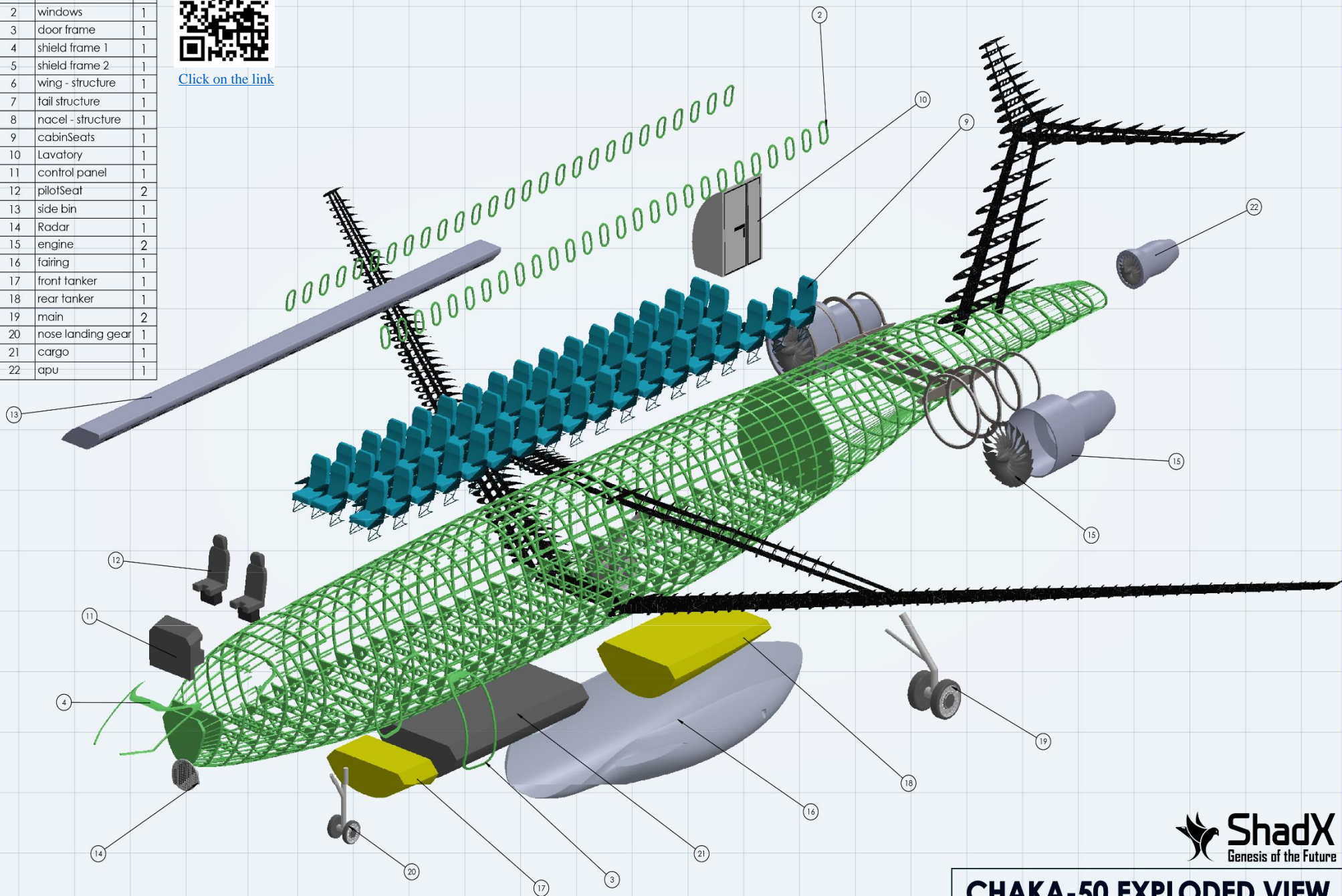


Figure 68- Detailed CG distribution for the Chaka-76 at MTOW configuration

ITEM NO.	PART NUMBER	QTY.
1	fuselage Structure	1
2	windows	1
3	door frame	1
4	shield frame 1	1
5	shield frame 2	1
6	wing - structure	1
7	tail structure	1
8	nacel - structure	1
9	cabinSeats	1
10	Lavatory	1
11	control panel	1
12	pilotSeat	2
13	side bin	1
14	Radar	1
15	engine	2
16	fairing	1
17	front tanker	1
18	rear tanker	1
19	main	2
20	nose landing gear	1
21	cargo	1
22	apu	1



[Click on the link](#)



CHAKA-50 EXPLODED VIEW



Table 52- Payload, unpaid load Breakdown (Relative to Nose)

Component	Chaka-50		Chaka-76	
	Weight (lb)	xCG (ft)	Weight (lb)	xCG (ft)
Pilot + bag	440	6.49	440	8.20
Passengers + carry on	10500	42.62	15960	49.57
Flight attendant + bag	220	11.54	440	14.76
Checked baggage	1500	41.012	2280	52.49
Wing fuel	up to 1800	42.60	up to 2000	53.83
Aft fuselage fuel	up to 8500	52.49	up to 12800	66.33
Forward fuselage fuel	up to 2500	22.96	up to 5200	29.52

Table 53- Empty Weight Breakdown (Relative to Nose)

Component	Chaka-50		Chaka-76	
	Weight (lb)	xCG (ft)	Weight (lb)	xCG (ft)
Wing	3337.51	50.52	7598.20	61.68
Empennage	1013.64	86.78	1900	109.91
Nose landing gear	277.94	11.35	704.97	11.35
Main landing gear	1228.57	54.20	2272.54	66.76
Fuselage	4354.67	44.29	8633	55.77
Engines + pylon + nacelle + engine control + engine starting + thrust reverser	4936.98	73.69	7230.30	93.50
Furnishings	1624.39	45.93	3238.97	58.07
APU	120	86.81	230	109.71
Paint	229.57	41.01	380.277	52.49
Cockpit instruments panel	1056.82	4.59	1435.6	5.905
Air cond./pressurization/icing	1209.24	59.05	2175.21	55.77
Avionic system	820.62	4.59	1148.85	5.90
Hydraulic system	459.14	65.62	760.55	82.02
Electric wiring	1708.82	41.012	1885.73	51.41
Oxygen system	113.64	36.09	151.72	45.93
Fuel system	1082.47	49.21	1163.45	62.18
Empty weight	23574.08		40909.47	

Figures 69 and 70 show the schematic empty and take-off weight breakdown for the Chaka-50 and -76, respectively.

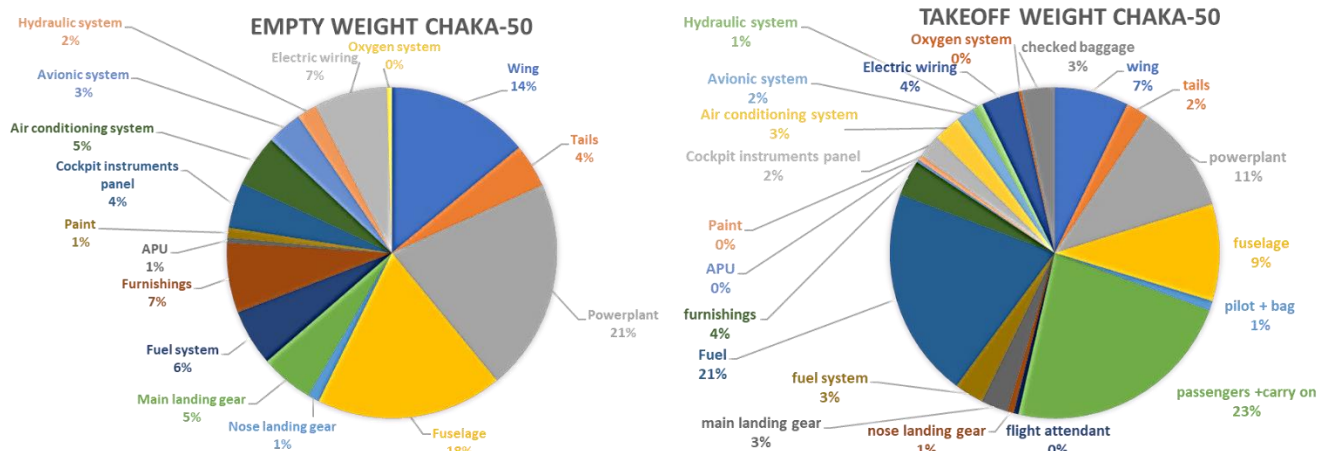


Figure 69--Empty (left) and take-off (right) weight breakdown of the Chaka-50

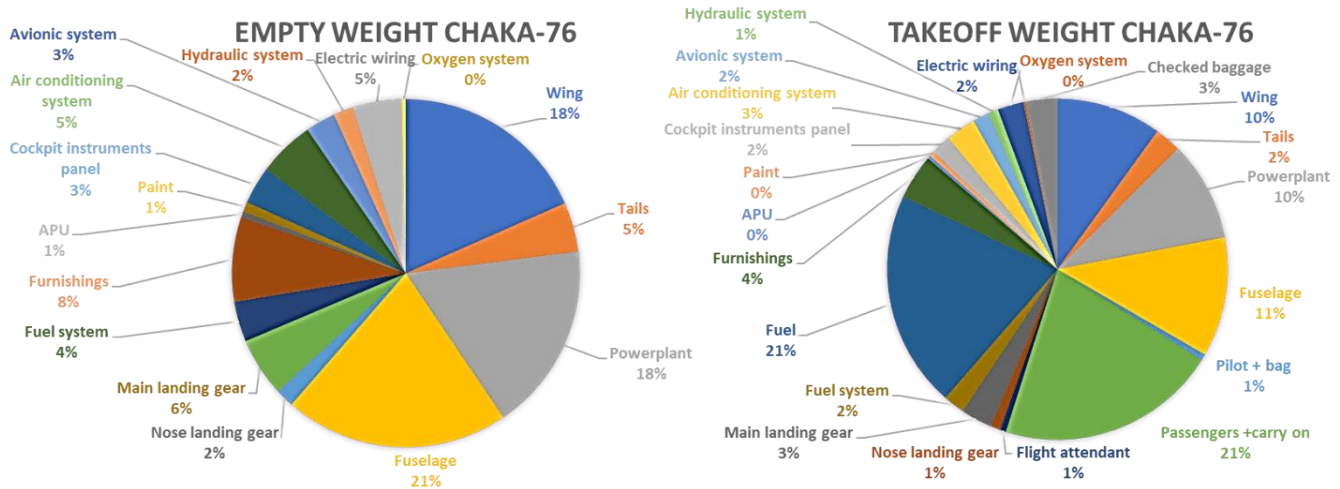


Figure 70-Empty (left) and take-off (right) weight breakdown of the Chaka--76

13 Landing Gear Design

For the Chaka undercarriage, a retractable tricycle configuration has been chosen due to the following [21, 63, 65]:

- Stability against ground loops
- Satisfactory ground control while in a crosswind
- Hard braking on main wheels cannot cause the airplane to nose over
- Diminished bouncing after touch-down
- A shorter wheelbase allows for a tight turning radius

Principal characteristics germane to the main- and nose-gear have been calculated using Gudmundsson method [63]. Figure 71 and Table 54 provide information about the geometric layout of the Chaka-MRJ's undercarriages.

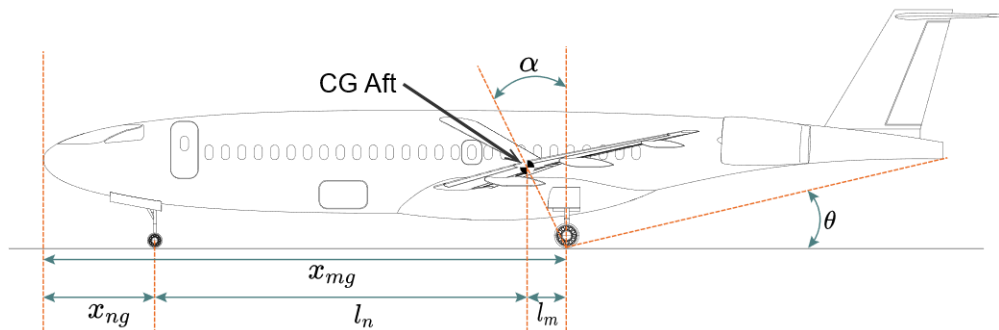


Figure 71- Landing gear characteristics along the fuselage

Table 54- Longitudinal characteristics of the Chaka MRJ family landing gears

Aircraft type	θ	α	x_{ng}	x_{mg}	l_n	l_m
Chaka-50	13.5°	15°	11.35 ft	51.90 ft	40.55 ft	2.76 ft
Chaka-76	12.5°	18.5°	11.35 ft	67.36 ft	52.36 ft	3.64 ft

Thanks to satisfactory values of α and θ , the aircraft will not experience any tail strike.

Table 55 shows the static and dynamic loads acting on each gear, calculated using Roskam's methodology [65].



Table 55- Static and dynamic loads acting on each gear

Aircraft type	Dynamic load on nose-gear	Static load on nose-gear	Static load on main-gear	MTOW
Chaka-50	7749.5 lb	5344.5 lb	20285 lb	45914.6 lb
Chaka-76	15022 lb	9617.2 lb	33219 lb	76055.5 lb

Since each gear has two tires, the load acting on each tire is half the amount of the load acting on each gear. Load capacity and minimal tire dimensions play essential roles in terms of tire selection. After considering various tires supplied by numerous manufacturers, the team selected the following tires, as shown in Table 56:

Table 56- Tire specifications for the Chaka-50 and -76 undercarriages

Aircraft	Gear Type	Manufacturer	Tire	Width	Outer Diameter	Rated Load
Chaka-50	Main-Gear	GoodYear	30 × 8.8 type VII	8.8 in	30 in	14200 lb
	Nose-Gear	GoodYear	18 × 4.4 type VII	4.4 in	18 in	4350 lb
Chaka-76	Main-Gear	GoodYear	34 × 11 type VII	11 in	34 in	20500 lb
	Nose-Gear	GoodYear	24 × 5.5 type VII	5.5 in	24 in	8070 lb

According to [65], in order to meet lateral ground clearance criteria, the angle ϕ , shown in Figure 72, must be more than 5 degrees. Table 57, illustrates the lateral ground clearance for the Chaka MRJ family.

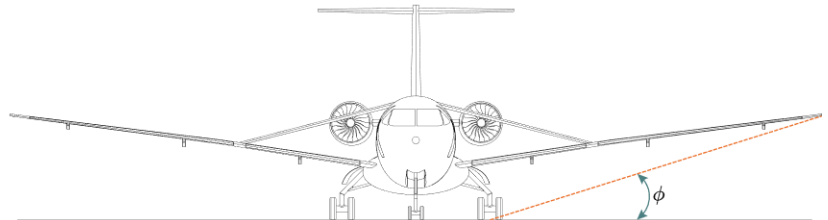


Figure 72- Landing gear lateral ground clearance criterion illustration

Table 57- Landing gear lateral ground clearance criterion for the Chaka MRJ family

Aircraft type	ϕ	Wheel track
Chaka-50	17.3°	13.94 ft
Chaka-76	14°	14.43 ft

For the lateral tip-over criterion, in accordance with [65], the angle ψ , shown in Figure 73, must be no more than 55 degrees. Table 58 shows the amounts of ψ angle for the Chaka MRJ family.

Table 58- Landing gear lateral tip-over criterion for the Chaka MRJ family

Aircraft type	ψ
Chaka-50	54.5°
Chaka-76	54.5°

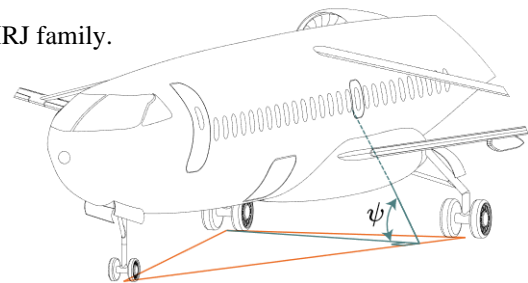


Figure 73- Landing gear lateral tip-over criterion illustration

The struts for each gear are designed utilizing equations in [65]. Table 59 shows strut geometry for each gear.

Table 59- Landing gear strut parameters for the Chaka MRJ family

Aircraft Type	Gear Type	S_s	d_s
Chaka-50	Main-Gear	15.81 in	4.76 in
	Nose-Gear	20.84 in	3.13 in
Chaka-76	Main-Gear	18.37 in	5.96 in
	Nose-Gear	20.86 in	4.22 in



Knowing that main landing gear doors are dead weights, the team conducted a trade-off study between aerodynamic performance and weight considerations, finally doing away with main-gear doors. In this manner, the main-gear can retract and fit into the fuselage fairing; this is followed by sealing up the gap between the tires and the fuselage. Figure 74 shows this feature in the Chaka MRJ family.

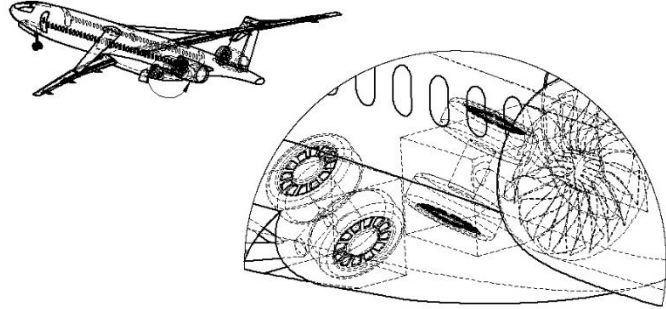


Figure 74 Chaka MRJ retracted landing gear

14 Stability and Control

This section presents stability, handling quality analysis, and 6 DOF dynamic simulations of the Chaka MRJ family.

14.1 Stability Analysis and Flying Quality

In the condition that small perturbations occur around a uniform flight, the coupled dynamic equations can be expressed linearly. In this section, to analyze the stability and flight quality of the designed aircraft, using aerodynamic coefficients and state-space equations, transfer functions are extracted. Therefore, for the longitudinal axis, it is sufficient to use Equation 9 [66]:

$$\text{Equation 9: } \begin{Bmatrix} \frac{u(s)}{\delta_e(s)} \\ \frac{\alpha(s)}{\delta_e(s)} \\ \theta \\ \frac{\delta_e(s)}{\delta_e(s)} \end{Bmatrix} = \begin{bmatrix} s - X_u - X_{T_u} & -X_w & g \cos(\theta) \\ -Z_u & s(1 - Z_w) - Z_w & -(Z_q + U)s + g \sin(\theta) \\ -M_u & -sM_w - M_w & s^2 - M_q s \end{bmatrix}^{-1} \begin{Bmatrix} X_{\delta_e}(s) \\ Z_{\delta_e}(s) \\ M_{\delta_e}(s) \end{Bmatrix}$$

And for the lateral axis to use Equation 10 [66]:

$$\text{Equation 10: } \begin{Bmatrix} \frac{\beta(s)}{\delta_a(s)} \\ \frac{\phi(s)}{\delta_a(s)} \\ \frac{\psi(s)}{\delta_a(s)} \\ \frac{\beta(s)}{\delta_r(s)} \\ \frac{\phi(s)}{\delta_r(s)} \\ \frac{\psi(s)}{\delta_r(s)} \end{Bmatrix} = \begin{bmatrix} sU_1 - Y_\beta & -(sY_p + g \cos(\theta)) & s(U_1 - Y_r) \\ -L_\beta & s^2 - L_p s & -sL_r \\ -N_\beta - N_{T\beta} & -N_p s & s^2 - sN_r \end{bmatrix}^{-1} \begin{Bmatrix} \frac{Y(s)}{\delta_a(s)} \\ \frac{L(s)}{\delta_a(s)} \\ \frac{N(s)}{\delta_a(s)} \\ \frac{Y(s)}{\delta_r(s)} \\ \frac{L(s)}{\delta_r(s)} \\ \frac{N(s)}{\delta_r(s)} \end{Bmatrix}$$

The aerodynamic coefficients were extracted in two phases of take-off and cruise by the CFD method and the dynamic coefficients for these phases were extracted by Digital Datcom software for the full body.



Table 60- Stability and control derivatives (1/rad) of the Chaka MRJ family

Longitudinal derivatives	Chaka-50		Chaka-76		Lateral-Directional derivatives	Chaka-50		Chaka-76	
	Take-off	Cruise	Take-off	Cruise		Take-off	Cruise	Take-off	Cruise
$C_{D\alpha}$	0.95	0.89	0.95	0.821	$C_{y\beta}$	-1.16	-1.26	-1.15	-1.03
$C_{L\alpha}$	11.06	14.88	11.06	14.13	$C_{l\beta}$	-0.06	-0.06	-0.06	-0.06
$C_{m\alpha}$	-12.18	-11.84	-12.19	-11.05	$C_{n\beta}$	0.150	0.154	0.15	0.15
C_{D_u}	0.040	0.041	0.01	0.04	C_{y_p}	-0.02	-0.01	-0.02	-0.01
C_{L_u}	0	0.081	0	0.081	C_{l_p}	-0.50	-0.57	-0.50	-0.46
C_{m_u}	0	-0.039	0	-0.039	C_{n_p}	-0.03	-0.03	-0.01	-0.03
C_{L_q}	11.31	12.53	11.25	12.4	C_{y_r}	0	0	0	0
C_{m_q}	-40.25	-40.69	-40.27	-41.10	C_{l_r}	0.07	0.05	0.07	0.09
$C_{L\dot{\alpha}}$	3.12	2.94	3.35	3.1	C_{n_r}	-0.74	-0.73	-0.24	-0.26
$C_{m\dot{\alpha}}$	-13.41	-14.28	-13.41	-14.28	$C_{y\delta_a}$	-0.001	-0.002	-0.001	-0.002
$C_{L_{iH}}$	0.34	0.22	0.34	0.22	$C_{l\delta_a}$	0.01	0.011	0.01	0.011
$C_{m_{iH}}$	-4.73	-3.23	-4.73	-3.23	$C_{n\delta_a}$	-0.013	-0.008	-0.013	-0.009
$C_{L\delta_e}$	0.96	0.78	1.26	1.01	$C_{y\delta_r}$	0.12	0.17	0.12	0.18
$C_{m\delta_e}$	-6.15	-5.98	-6.13	-5.96	$C_{l\delta_r}$	0.06	0.008	0.06	0.008
$C_{D_{iH}}$	0	0	0	0	$C_{n\delta_r}$	-0.01	-0.02	-0.01	-0.02

The aircraft's transfer functions at take-off condition and AOA of 3 degrees, and also at cruise condition and AOA of 1 degree are shown in Table 61.

Table 61- Transfer functions at take-off and cruise

	Take-off	Cruise
$\frac{u(s)}{\delta_e(s)}$	$\frac{45.52s^3 - 3.758s^2 + 36.06s + 36.7}{67.62s^4 + 55.64s^3 + 17.93s^2 + 0.8685s + 0.1922}$	$\frac{u(s)}{\delta_e(s)} = \frac{1.011e04s^3 + 1.92e04s^2 + 4.163e04s + 1.8e04}{778.9s^4 + 1257s^3 + 807.5s^2 + 13.64s + 2.283}$
$\frac{\alpha(s)}{\delta_e(s)}$	$\frac{9.649s^3 - 1.107s^2 - 0.08514s - 0.01242}{67.62s^4 + 55.64s^3 + 17.93s^2 + 0.8685s + 0.1922}$	$\frac{\alpha(s)}{\delta_e(s)} = \frac{-64.51s^3 - 395.4s^2 - 6.996s - 1.229}{778.9s^4 + 1257s^3 + 807.5s^2 + 13.64s + 2.283}$
$\frac{\theta(s)}{\delta_e(s)}$	$\frac{-1.976s^2 - 3.879s - 0.2132}{67.62s^4 + 55.64s^3 + 17.93s^2 + 0.8685s + 0.1922}$	$\frac{\theta(s)}{\delta_e(s)} = \frac{-394.1s^2 - 567s - 7.541}{778.9s^4 + 1257s^3 + 807.5s^2 + 13.64s + 2.283}$
$\frac{\beta(s)}{\delta_a(s)}$	$\frac{0.007017s^3 + 0.5256s^2 + 0.7794s + 0.02975}{66.4s^4 + 56.2s^3 + 9.513s^2 + 2.785s + 0.08994}$	$\frac{\beta(s)}{\delta_a(s)} = \frac{11.54s^2 + 19.7s + 0.6086}{778.3s^4 + 825.4s^3 + 348s^2 + 239.3s + 3.114}$
$\frac{\phi(s)}{\delta_a(s)}$	$\frac{4.496s^2 + 3.468s + 0.2709}{66.4s^4 + 56.2s^3 + 9.513s^2 + 2.785s + 0.08994}$	$\frac{\phi(s)}{\delta_a(s)} = \frac{219.6s^2 + 44.33s + 39.19}{778.3s^4 + 825.4s^3 + 348s^2 + 239.3s + 3.114}$
$\frac{\psi(s)}{\delta_a(s)}$	$\frac{-0.5358s^3 - 0.5057s^2 - 0.08503s + 0.01836}{66.4s^4 + 56.2s^3 + 9.513s^2 + 2.785s + 0.08994}$	$\frac{\psi(s)}{\delta_a(s)} = \frac{-11.57s^3 - 12.18s^2 - 1.436s + 1.539}{778.3s^4 + 825.4s^3 + 348s^2 + 239.3s + 3.114}$
$\frac{\beta(s)}{\delta_r(s)}$	$\frac{1.861s^3 + 5.434s^2 - 0.2976s - 0.04127}{66.4s^4 + 56.2s^3 + 9.513s^2 + 2.785s + 0.08994}$	$\frac{\beta(s)}{\delta_r(s)} = \frac{14.5s^3 + 40.48s^2 + 31.12s + 0.355}{778.3s^4 + 825.4s^3 + 348s^2 + 239.3s + 3.114}$
$\frac{\phi(s)}{\delta_r(s)}$	$\frac{-4.143s^2 - 3.691s - 1.559}{66.4s^4 + 56.2s^3 + 9.513s^2 + 2.785s + 0.08994}$	$\frac{\phi(s)}{\delta_r(s)} = \frac{158.9s^2 + 5.034s - 5.559}{778.3s^4 + 825.4s^3 + 348s^2 + 239.3s + 3.114}$
$\frac{\psi(s)}{\delta_r(s)}$	$\frac{-5.201s^3 - 3.988s^2 - 0.2051s - 0.1975}{66.4s^4 + 56.2s^3 + 9.513s^2 + 2.785s + 0.08994}$	$\frac{\psi(s)}{\delta_r(s)} = \frac{-27.08s^3 - 23.52s^2 + 0.1146s - 0.2199}{778.3s^4 + 825.4s^3 + 348s^2 + 239.3s + 3.114}$

Where the eigenvalues, natural frequency, time constant, and damping ratio are shown in Table 62.



Table 62- Stability and flight handling quality analysis at take-off and cruise

		Poles	Damping	Frequency (rad/sec)	Time Constant (sec)	Handling quality level
Take-off	Longitudinal	-0.0069 + 0.10i -0.0069 - 0.10i -0.404 + 0.28i -0.404 - 0.28i	0.06(Ph) 0.82(S.p)	0.10 0.49	145 2.47	Level 1 (Ph) Level 1 (S.p)
	Lateral	-0.03 -0.0428 + 0.22i -0.0428 - 0.22i -0.72	1(S) 0.18(D) 1(R)	0.03 0.22 0.72	27.90 23.40 1.38	Level 1 (S) Level 1 (D) Level 1 (R)
Cruise	Longitudinal	-0.0064 + 0.05i -0.0064 - 0.05i -0.8 + 0.61i -0.8 - 0.61i	0.11(Ph) 0.79(S.p)	0.05 1.01	157 1.25	Level 1 (Ph) Level 1 (S.p)
	Lateral	-0.01 -0.05 + 0.5i -0.05 - 0.5i -0.93	1(S) 0.103(D) 1(R)	0.01 0.57 0.93	75.4 17.10 1.08	Level 1 (S) Level 1 (D) Level 1 (R)

According to [67], the damping ratio of the short-period mode at the take-off phase should be at least 0.5, which, as shown in the above table, is 0.82. Also, the damping ratio of the Phugoid mode should be greater than or equal to 0.04, which is also passed.

To analyze the flight quality of the roll mode, the time constant of this mode should be less than 1.4 seconds, which as shown in the above table, is 1.38 seconds. Also, the damping ratio of the Dutch roll mode should be at least 0.08, which is 0.18 for the designed aircraft. Flight quality requirements for the cruise phase are also met. The response of the transfer functions to the step input is examined at take-off condition.

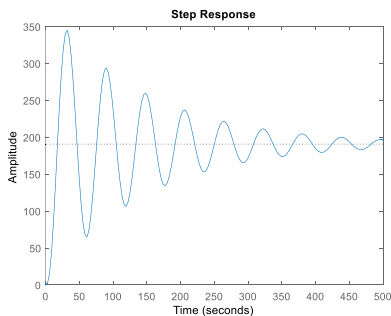


Figure 75- $\frac{u(s)}{\delta_e(s)}$

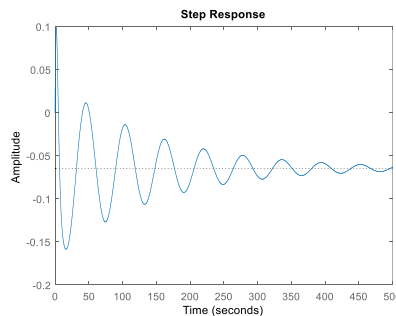


Figure 76- $\frac{\alpha(s)}{\delta_e(s)}$

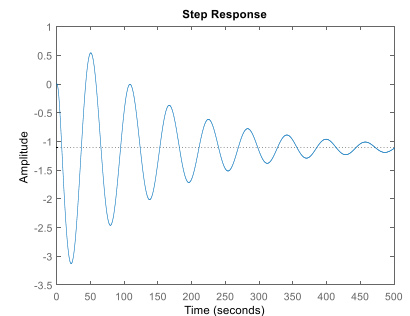


Figure 77- $\frac{\theta(s)}{\delta_e(s)}$

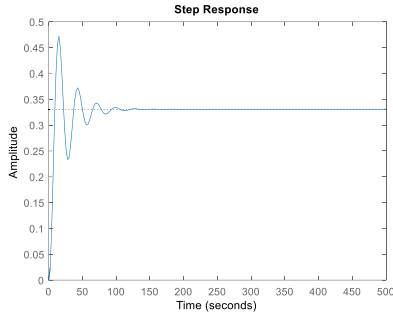


Figure 78- $\frac{\beta(s)}{\delta_a(s)}$

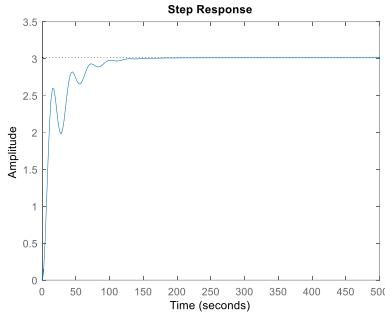


Figure 79- $\frac{\phi(s)}{\delta_a(s)}$

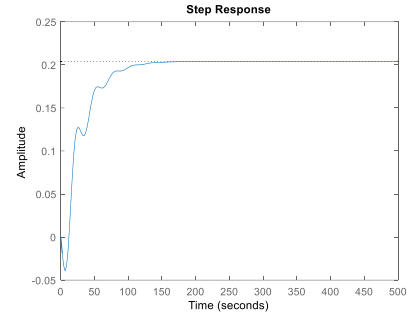


Figure 80- $\frac{\psi(s)}{\delta_a(s)}$

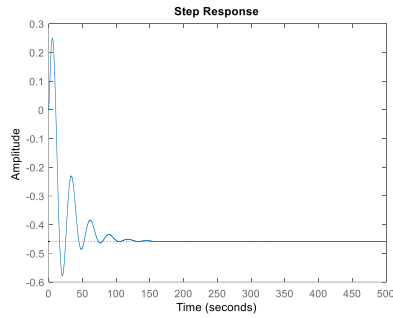


Figure 81- $\frac{\beta(s)}{\delta_r(s)}$

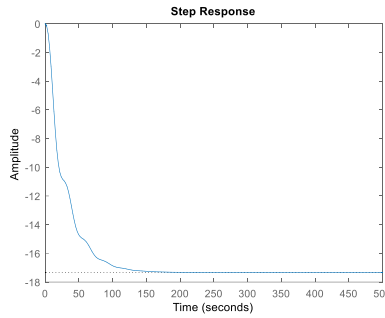


Figure 82- $\frac{\phi(s)}{\delta_r(s)}$

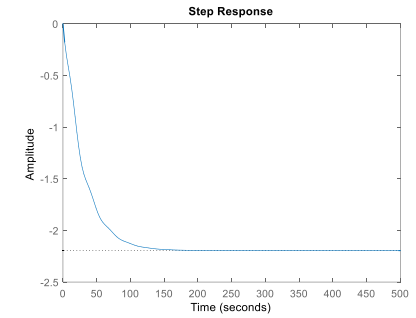


Figure 83- $\frac{\psi(s)}{\delta_r(s)}$

In this section, the response of the transfer functions to the step input is examined at cruise condition.

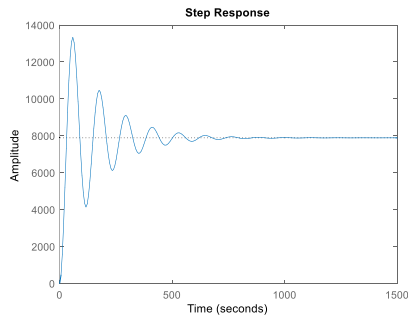


Figure 84- $\frac{u(s)}{\delta_e(s)}$

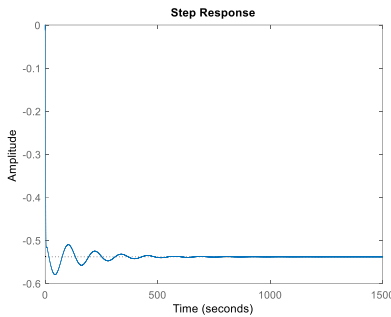


Figure 85- $\frac{\alpha(s)}{\delta_e(s)}$

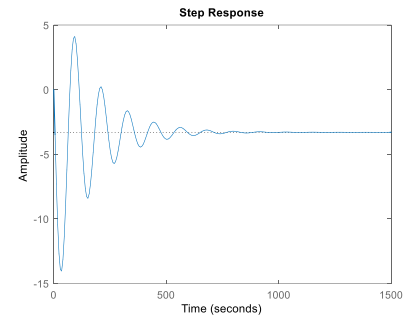


Figure 86- $\frac{\theta(s)}{\delta_e(s)}$

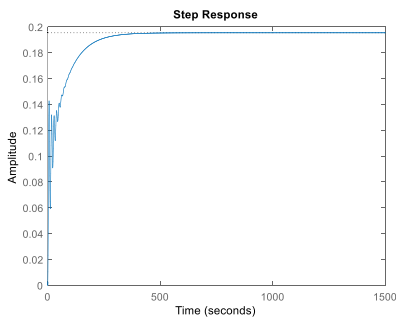


Figure 87- $\frac{\beta(s)}{\delta_a(s)}$

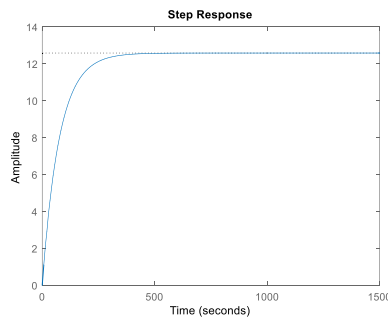


Figure 88- $\frac{\phi(s)}{\delta_a(s)}$

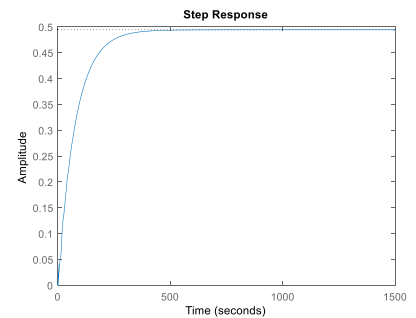


Figure 89- $\frac{\psi(s)}{\delta_a(s)}$

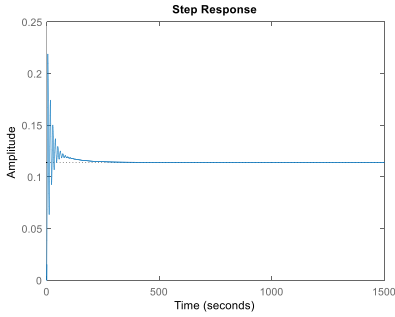


Figure 90- $\frac{\beta(s)}{\delta_r(s)}$

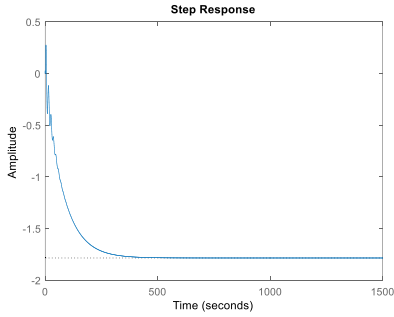


Figure 91- $\frac{\phi(s)}{\delta_r(s)}$

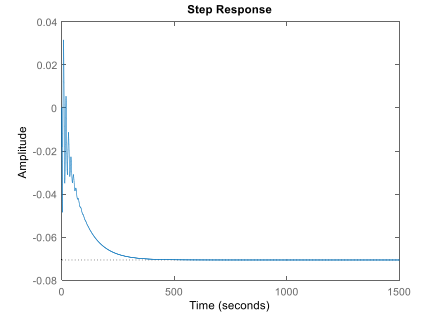


Figure 92- $\frac{\psi(s)}{\delta_r(s)}$

14.2 Trim Analysis and 6DOF Simulation

To draw a trim diagram, after calculating $Cm_0, Cm_{\delta_e}, Cm_{i_H}$, the following equations are solved for changing the angle of the elevator from -20 degrees to 20 degrees and changing the angle of attack from -10 to 10 degrees.

$$C_L = C_{L_0} + C_{L_\alpha} \cdot \alpha + C_{L_{i_H}} \cdot i_H + C_{L_{\delta_e}} \cdot \delta_e$$

$$C_m = C_{m_0} + \left(\frac{C_{m_\alpha}}{C_{L_\alpha}} \right) \cdot C_L + C_{m_{i_H}} \cdot i_H + C_{m_{\delta_e}} \cdot \delta_e$$

The result is the following diagram:

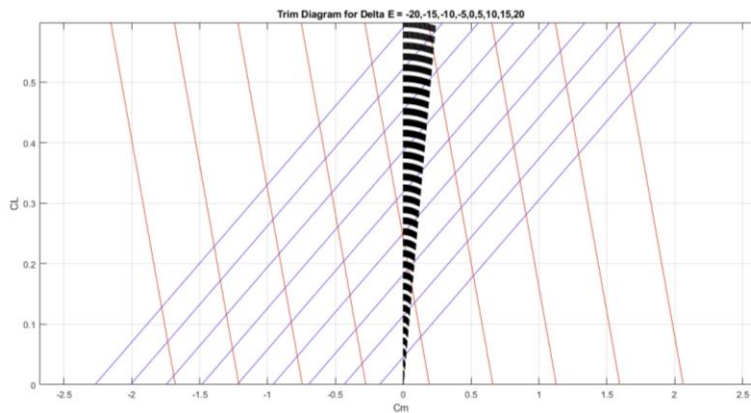


Figure 93- Trim diagram of the Chaka-50

It is concluded that for changing the angle of the elevator at each AOA, the pitching moment coefficient is necessary to provide a C_L for a point. The first limitation is the AOA that cannot exceed a certain value, which is the highest purple line with 10 degrees. Also, the AOA cannot be less than a certain value (the lowest purple line). The pitching moment generated by the elevator is the second constraint applied by the red lines on the diagram. Thus, the elevator control power is sufficient for controlling the aircraft in longitudinal motions.

For an aircraft to be able to fly in a steady-state flight condition and also to be able to maneuver from one flight condition to another, it is necessary that:

- The aircraft have sufficient controllability



- The pilot do not make extra effort

Therefore, for an aircraft to fly, it must be trimmed at all steady-state flight conditions. The trim ability means that the linear and angular accelerations be equal to zero and within the allowable range of motion and control parameters. Therefore, the purpose of this section is to extract the conditions in which if the aircraft were to fly at the cruise phase, it would have no linear and angular acceleration.

$$\begin{aligned}
 mg \sin \gamma_1 &= -(C_{D_0} + C_{D_\alpha} \alpha_1 + C_{D_{i_h}} i_{h_1} + C_{D_{\delta_e}} \delta_{e_1}) q^{-1} S + T_1 \cos(\phi_T + \alpha_1) \\
 mg \cos \gamma_1 &= (C_{L_0} + C_{L_\alpha} \alpha_1 + C_{L_{i_h}} i_{h_1} + C_{L_{\delta_e}} \delta_{e_1}) q^{-1} S + T_1 \sin(\phi_T + \alpha_1) \\
 0 &= (C_{m_0} + C_{m_\alpha} \alpha_1 + C_{m_{i_h}} i_{h_1} + C_{m_{\delta_e}} \delta_{e_1}) q^{-1} S \bar{c} - T_1 d_T
 \end{aligned}$$

By solving the above three equations with the three unknowns, the required thrust, angle of attack, and deflection angle, for the elevator to trim the aircraft at an altitude of 35,000 feet, are calculated.

Table 63- Trim conditions of the Chaka MRJ family

Thrust required (lbf)	AOA (deg)	Elevator deflection (deg)
4435.8	0.34	-1.25

In this section, using nonlinear, coupled, and kinematic equations, a 6 DOF simulation is carried out. By applying the above conditions to the simulation, the aircraft must be trimmed. Linear momentum equations are as follows [66]:

$$m(\dot{U} - VR + WQ) = -mg \sin \theta + F_{Ax} + F_{Tx} \quad m(\dot{V} + UR - WP) = mg \sin \theta \cos \theta + F_{Ay} + F_{Ty} \quad m(\dot{W} - UQ + VP) = mg \sin \theta \cos \theta + F_{Az} + F_{Tz}$$

Angular momentum equations are as follows [66]:

$$I_{xx} \dot{P} - I_{xz} \dot{R} - I_{xz} PQ + (I_{zz} - I_{yy}) RQ = L_A + L_T \quad I_{yy} \dot{Q} + (I_{xx} - I_{zz}) + I_{xz} (P^2 - R^2) = M_A + M_T \quad I_{zz} \dot{R} - I_{xz} \dot{P} + (I_{yy} - I_{xx}) PQ + I_{xz} QR = N_A + N_T$$

Kinematic equations are as follows [66]:

$$\dot{\phi} = P + Q \sin \phi \tan \theta + R \cos \phi \tan \theta \quad \dot{\theta} = Q \cos \phi - R \sin \phi \quad \dot{\psi} = (Q \sin \phi + R \cos \phi) \sec \theta$$

According to the following figures, velocity along the X-axis changes ± 20 ft/sec, and then the perturbations are damped. Angular velocity about the Y-axis changes negligibly.

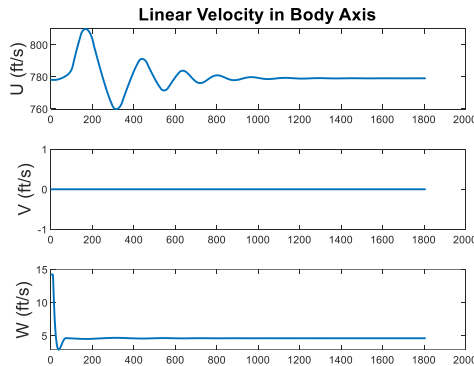


Figure 94- Linear velocity of the Chaka-50

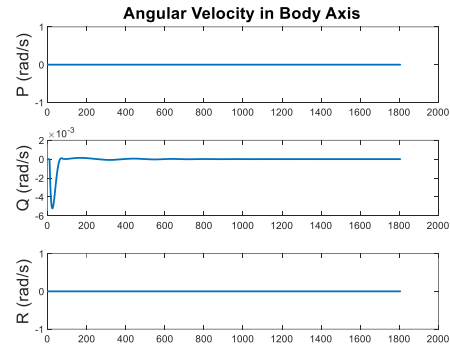


Figure 95- Angular velocity of the Chaka-50

According to the following figures, after some very small perturbations, the pitch angle converges somewhere close to the AOA. According to the results of the above equations shown in Table 63, the figure on the right shows



that the angle of attack converges to value of 0.34 degrees, without any controller, after 1800 seconds. This diagram guarantees the accuracy of the simulation conducted in the Simulink software.

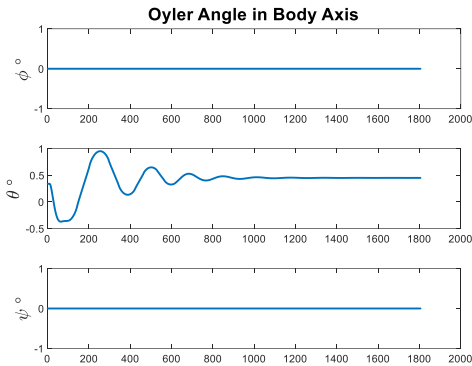


Figure 96- Oyler angle of Chaka-50

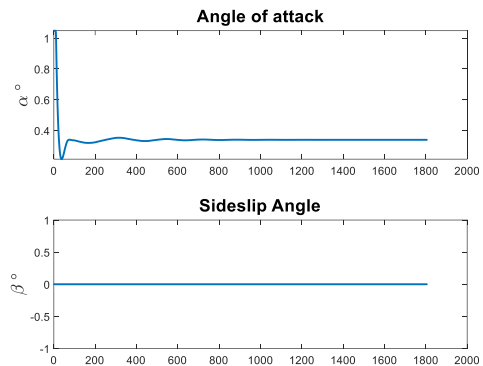


Figure 97- Angle of attack and side slip of Chaka-50

Applying the values shown in Table 63 to the simulation, it can be observed that the aircraft increases its altitude by 7,000 feet after 30 minutes without any controller.

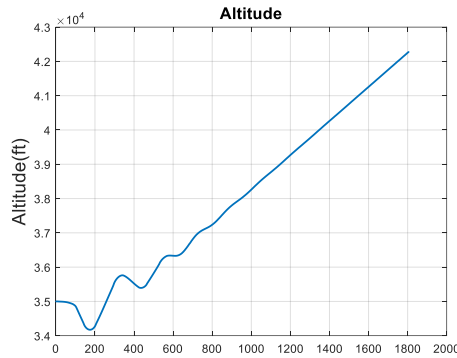


Figure 98- Elevation versus time

14.3 Autonomous Operation

In the past, the main obstacle to developing autonomous flight was the level of technology since humans had to be replaced with intelligent guidance and navigation systems requiring highly sophisticated sensors. Nowadays, with the



development of small and powerful processors, fast and accurate sensors, the technology level is no longer a concern.

Figure 99 illustrates the intellectual levels of autonomous flight [68].

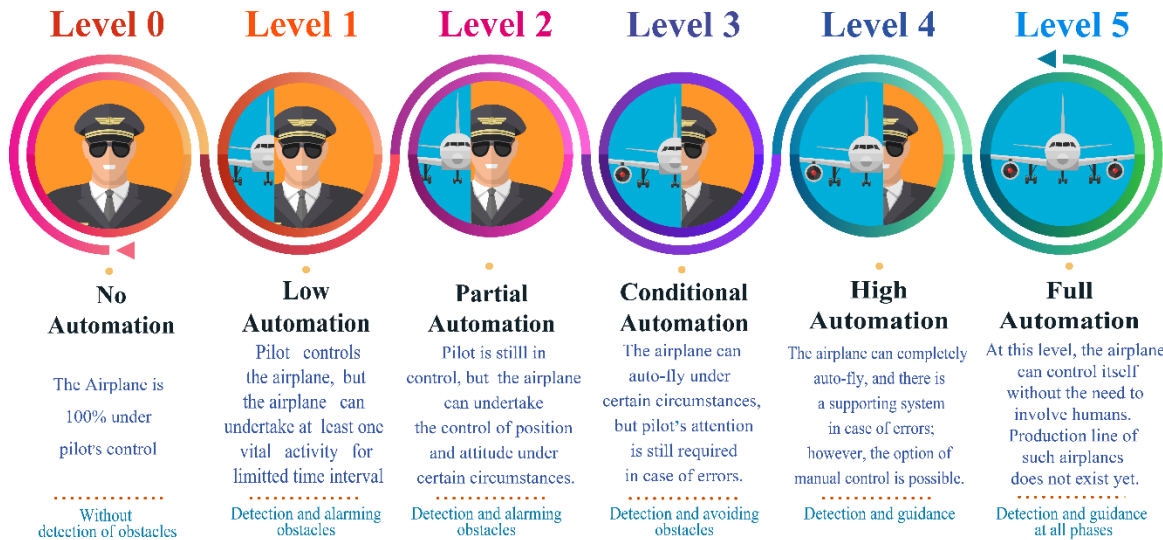


Figure 99- Intellectual levels of autonomous flight

In this project, the 5th level of intelligence is intended to be utilized. Moreover, if this level is implemented, in the swarm and collaborative manner, the efficiency of the aircraft's automation system will increase in several ways. In this way, each aircraft will share environmental information and the output quality of each action in every state and attitude, and other aircraft can act based upon collective awareness, leading into increased intelligence and convergence of the autonomous flight algorithm.

In fact, the collective intelligence is complex behavior (including traffic control) consisting sets of simple behavior (i.e., complete fulfillment of a mission profile); such behavior is seen in many creatures in nature, such as ants. The proposed system is predicated upon a combination of hardware configuration and the architecture of a flexible system allowing for high-level missions to be thoroughly fulfilled without human intervention.

14.3.1 A Description of the Autonomous System

The architecture of the flexible system contains the two following nodes: Global traffic planner (GTP) and Aircraft mission planner (AMP). The GTP node is responsible for generating and managing mission profiles for all aircraft on a flight network. The term "flexible" is used since the system can create and manage mission profiles both automatically and manually for all aircraft in a flight network. In this node, the fuzzy C-means clustering algorithm is used to generate a mission profile [69].



This algorithm optimally determines the waypoints of the mission profile based upon weighted data provided by past flights or dispatching units. Clearly, safety options of this algorithm would not be a replacement for TCAS/ACAS, and it is added to the aforesaid principal systems as an extra option. In order to train the aircraft before flight, a reinforcement learning framework must be developed to integrate a deep reinforcement learning agent with a simulator like Gazebo. This simulator has advantages over other simulators [70].

The reinforcement learning algorithm is chosen since it is not feasible to thoroughly train the aircraft for all scenarios with supervised learning algorithms. For example, a limited number of mayday scenarios could be created in the simulator environment and after recording the pilots' reactions, the optimal action is extracted and taught to the intelligent agent. Thousands of other mayday and non-emergency scenarios are customizable around these scenarios. In Deep Reinforcement Learning with reward and policy [71] capability, auto-training is also possible.

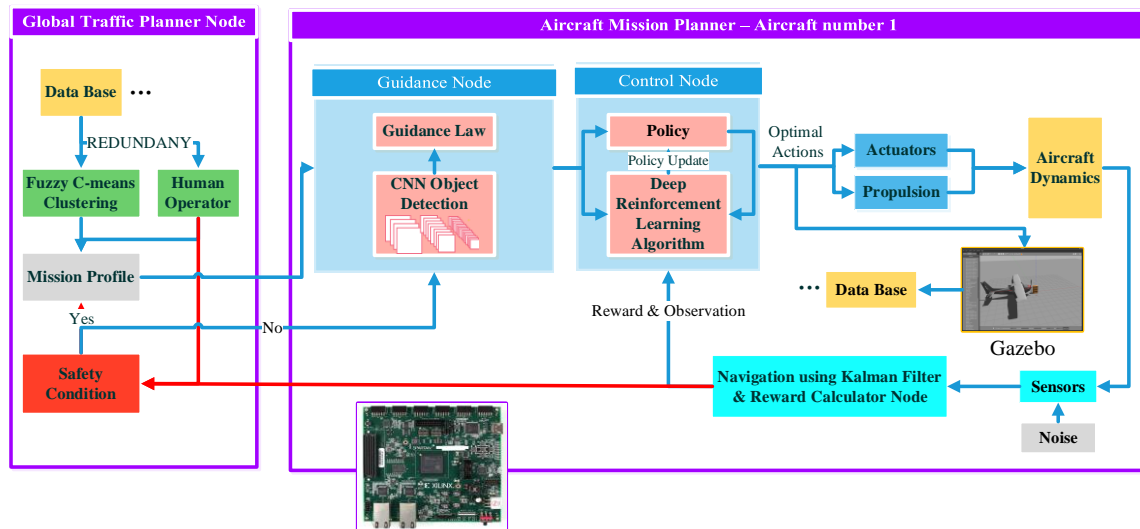


Figure 100- Proposed autonomous flight algorithm for the Chaka MRJ family

Figure 100 is the representation of the suggested autonomous flight algorithm added to the existing principal algorithms of aircraft. Mission profiles generated by the GTP node will be published to the guidance segment of each aircraft. The mission profile also contains operations carried out on the airport. During taxiing, aircraft navigate using navigation nodes and safety conditions (containing other airplanes' data) and also CNN algorithm (added to the other existing guidance algorithms). Furthermore, control of each aircraft to reach the waypoint is done by the Control Node.

Following that, in parallel and simultaneously, each flight is simulated in the Gazebo environment using the developed nodes in Robot Operating System (ROS) [72], and the agents' training will be updated. The hardware architecture is suggested to use the Field Programmable Gate Array (FPGA) in order to enable parallel processing and minimize lag problems in command transmission and data receiving.



15 Systems and Components

In this section, subsystems of the Chaka MRJ family, according to Figure 101, are discussed.

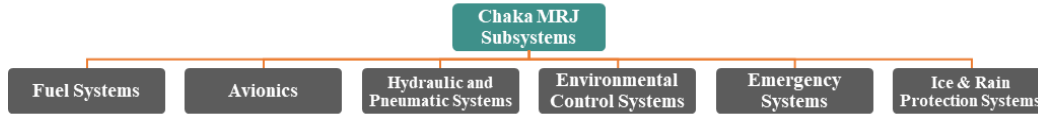


Figure 101- Various subsystems of the Chaka MRJ family

15.1 Fuel Systems

The fuel system stores fuel and supplies it to the power plant. It is also used to control the CG movement of the aircraft. Fuel management and pumping systems are used to balance the aircraft in all conditions. Fuel lines are located away from sensitive and vulnerable areas, and shut-off valves are utilized in case of damage. The primary fuel tank is located in the aft fuselage. A venting System controls the tank's pressure according to

structural limits. It also prevents fuel spillage during flight maneuvers. Figure 102 illustrates the Chaka-50 fuel system.

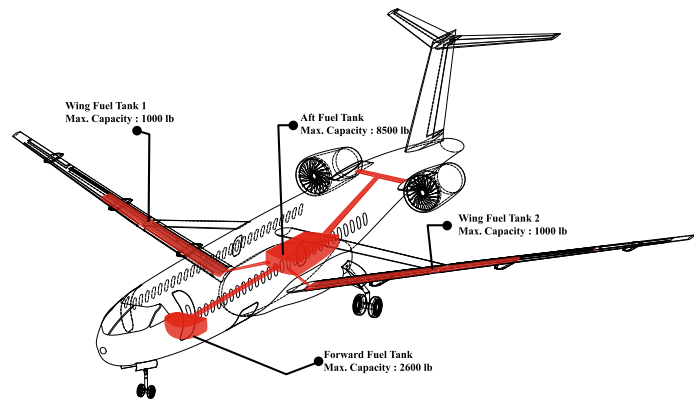


Figure 102- Fuel system of the Chaka-50

15.2 Hydraulic Systems

The aircraft is provided with a hydraulic power system designed to supply adequate power (up to 3000 psi) to meet the performance and redundancy requirements of safe flight. Information with regard to fluids and pumps is available on the Systems Monitoring Display. Figure 103 illustrates hydraulic system of the Chaka MRJ family.

The hydraulic power system supplies pressure for the operation of the following systems:

- Primary Flight Controls
- Landing Gear
- Nose Wheel Steering
- Spoilers
- Thrust Reverser
- Main Landing Gear Brakes

For the fly-by-wire system, hydrostatic actuators will be used, possessing their own hydraulic systems.

15.3 Avionics and Instruments Systems

Avionics is a feature of paramount importance in modern aircraft design. Control systems, onboard computers, communication equipment, and sensor suites constitute only a portion of the electronic systems allowing the aircraft fulfill what it has been designed for. Table 64 shows the comparison of 4 compatible avionic suites.



Table 64 Comparison between compatible avionic suites

Avionic system's designation	Honeywell Primus 1000	Honeywell Primus Epic	Rockwell Collins Pro Line 4	Garmin G5000
Compatible aircraft	Embraer ERJ series	Embraer E170	Bombardier CRJ Series	Cessna Citation Excel
IFR flight capability	Capable	Capable	Capable	Capable
GS/IRS	Rockwell Collins Flight Dynamics (HGS™) / Primus Elite Synthetic Vision	SmartView Synthetic Vision	Rockwell Collins Flight Dynamics HGS™	Garmin GHD™
AHRS	dual attitude	AH-1000	dual attitude	Garmin AHRS
TAWS	EGPWS / RAAS	EGPWS / RAAS	GPWS	GPWS
TCAS	TCAS II	TCAS II	TCAS II	TCAS II
RVSM	Capable	Capable	Capable	Capable
ILS	CAT III ILS	CAT III ILS	CAT III ILS	CAT III ILS
ADS-B	Compatible	Compatible	Compatible	Compatible
FMS	FMZ-2000	FMZ-2000	1 or 2 Collins FMS-4200	Dual integrated FMS
Displays	Two multi-function and two primary displays one IECMS (8in×7in)	Four displays	Four multi-function and two primary displays	Three 12-inch touchscreen displays
Conspicuous properties	- Low cost - Common usage	- All-digital - Lightweight - Modular architecture - Fly-by-wire capability	- Stable operational history	- Removed wires - Touchscreen - Lightweight

Owing to the existing competitive market, the packages are practically identical in terms of scope and overall capabilities. The packages must fully handle day-in and day-out requirements of the regional airline operations; such situations are one of the most difficult challenges experienced in the regional commercial aviation. For instance, RJ avionic systems, on average, experience as many as five or even more take-off, climb, cruise, descent, and landing flights during a working day. These flights are invariably accompanied by more turbulence, pressure, and temperature changes compared to large high-subsonic wide-body aircraft [73].

CAT III operations are essential in the frequently fog-bound northwestern US, which does not just include landings. However, Also, the level of reliability must be sufficiently high, and the HGS/IRS option is not easily justified in other less demanding parts of North America, although Air Canada and its Jazz subsidiary carry this option in their Bombardier RJs.

Also, the level of reliability must be sufficiently high, and if a failure occurs, the system must be capable of conducting fast and accurate diagnosis and rapid line replaceable unit (LRU) exchange during the aircraft's very short turnaround times. Wiring in terms of critical flight components must be triply redundant and separately located. Three actuators must be used for each outboard flap, spoiler, and aileron. Two actuators must be used for each inboard flap



and spoiler, the rudder, and the elevators. This provides full functionality to each control surface in case of one actuator failure. Figure 103 illustrates Electrical wirings of the Chaka MRJ family.

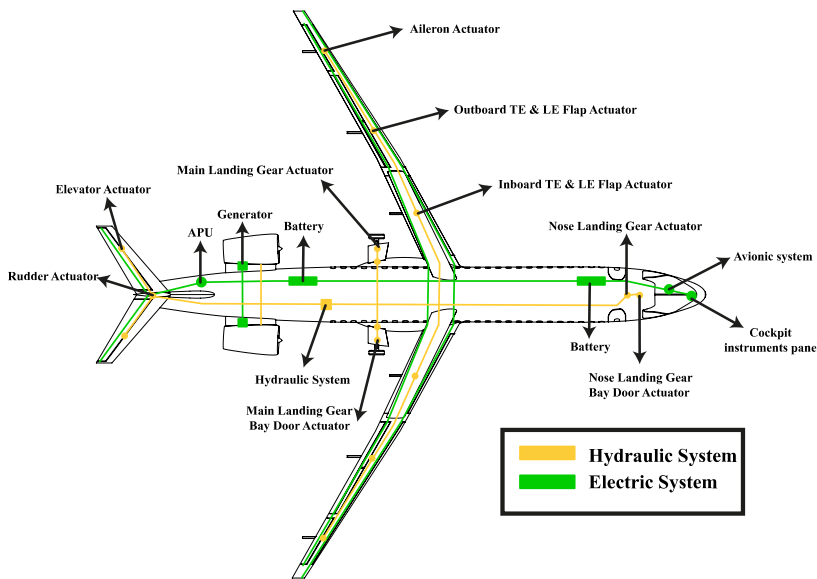


Figure 103- Hydraulic System & Electric System of the Chaka MRJ family

Garmin G5000 is a state-of-the-art design with touchscreen displays, user-friendly systems, and lightweight systems thanks to removed wires. However, it has not been installed in a regional jet, and its cost would be higher than the other competitors [77].

Our team has decided to use the Honeywell Primus Epic for its availability and compatibility, thanks to its modular design. The Primus Epic also meets applicable certification requirements of the FAA 14 CFR Part 25 and has the capability of IFR flight. It is a cutting-edge design for the target year of 2030.

Figure 104 depicts the Honeywell Primus Epic 2.0.

The Primus Epic comprises:

- Two primary flight displays featuring crystal-clear, high-resolution and wide viewing capability, allowing for cross cockpit scanning
- Integration of aircraft systems, safety sensors and navigation information to decrease pilot workload and improve safety through enhanced situational awareness
- Increased reliability using advanced design techniques, ruggedization and solid-state sensors



Figure 104- PRIMUS® EPIC 2.0 FLIGHT DECK BY HONEYWELL



- Capability of satisfying Communication Navigation Surveillance/Air Traffic Management (CNS/ATM) operational and environmental requirements
- A flexible architecture allowing for easy integration of hardware and software as new technology becomes available
- Primary flight displays supporting SmartView™ Synthetic Vision –with advanced symbology (including 3-D terrain, Approach guidance, En route, Terrain alerting, and Visual runway) which gives the aircraft CAT III landing capability
- Fly-by-wire systems
- Automatic Flight Control System (ACFS) Providing the Autopilot System [78]

15.4 VFR and IFR Flight Requirements

In terms of VFR and IFR flight, the type of airspace must be known. The two principal categories of airspace are: regulatory and nonregulatory. There are four types within these two categories: controlled, uncontrolled, special use, and other airspace. Figure 105 presents a profile view in terms of various classes of airspace [79].



Figure 105- Airspace classes

15.4.1 Controlled Airspace

Controlled airspace is a generic term covering different classifications of airspace and defined dimensions within which air traffic control (ATC) service is provided, in accordance with the airspace classification. Controlled airspace is classified as shown in Table 65.

Table 65- Requirements for airspace operations

Class Airspace	Entry Requirements	Equipment *	Minimum Pilot Certificate
Class A	ATC clearance	IFR equipped	Instrument rating
Class B	ATC clearance	Two-way radio, transponder with altitude reporting capability	Private—(However, a student or recreational pilot may operate at other than the primary airport if seeking private pilot certification and if regulatory requirements are met.)



Class C	Two-way radio communications prior to entry	Two-way radio, transponder with altitude reporting capability	No specific requirement
Class D	Two-way radio communications prior to entry	Two-way radio	No specific requirement
Class E	None of VFR	No specific requirement	No specific requirement
Class G	None	No specific requirement	No specific requirement
* Beginning January 1, 2020, ADS-B Out equipment may be required in accordance with 14 CFR part 91, section 91.225			

15.4.2 Uncontrolled Airspace

Class G Airspace: Uncontrolled airspace or Class G airspace is the portion of the airspace that has not been designated as Class A, B, C, D, or E. It is therefore designated uncontrolled airspace. Class G airspace extends from the surface to the base of the overlying Class E airspace. Although ATC has no authority or responsibility to control air traffic in this class, pilots ought to remember there are visual VFR minimums that apply to Class G airspace.

15.4.3 Operating Rules and Pilot/Equipment Requirements

Flight safety is the top priority of all pilots, and the responsibilities associated with operating an aircraft should always be taken seriously. The air traffic system maintains a high degree of safety and efficiency with strict regulatory oversight of the FAA.

15.5 Environmental Control Systems

Environmental control systems provide temperature and humidity control of the cabin and also the pressurization system. Environmental Control Systems consist of:

- Pressurization system
- Avionics cooling
- Air-conditioning system
- Pneumatic system
- Smoke detection
- Oxygen system

The system, therefore, maintains passenger comfort and pressures suitable for human survivability. Airflow is provided via ram air, which is temperature-controlled through cooling units and pressurized by bleed air. All the control is to be managed from the cockpit. Also, the avionic systems of the aircraft need significant cooling. High pressurization reliability is required as the results of depressurization at high altitudes can be fatal. Reliability is achieved through redundancy. Therefore, the pressurization system is powered by the bleed air of each engine, in the case of one engine failure, and by an electrically powered air pump in case of double engine failure. 20 ft³ of air per passenger per minute shall be provided as recommended in [64]. High-reliability systems must be used for the crew and passengers. Therefore, the crew members shall have their own cylinders of oxygen, and the passengers shall have access to larger cylinders of oxygen. Figure 106 illustrates the pneumatic and air conditioning systems.



15.6 Emergency Systems

These systems predominantly consist of emergency lighting, passenger and crew personal flotation equipment, emergency rafts, and communication systems separate from the primary system. The emergency system also encompasses the following elements:

- Separated battery to supply power to emergency lighting and communication systems
- Manual overcome ability for any closing/locking systems on doors in case of emergency
- 4 six-person emergency rafts
- Personal flotation equipment providing emergency flotation for ten individuals in case one of the rafts fails
- Three Protective Breathing Equipment (PBE) units (The PBE is the equipment for protection of the crew members against the effects of smoke, toxic gases, and hypoxia)
- Two oxygen cylinders, positioned near cabin attendant stations, to be used for first-aid therapeutic purposes
- Emergency Free-Fall Landing Gear Extension between the copilot's seat and control pedestal

The airplane is equipped with additional emergency equipment according to the local authorities' regulations. A typical set is composed of portable fire extinguishers, megaphone, first-aid kit, medical kit, hatchet, smoke goggles, and flashlights [80].

15.7 Ice & Rain Protection Systems

Ice and rain protection is provided for the following components:

- Wing leading edges
- Windshields
- Air data probes and sensor
- Engine intake cowls
- Side windows

Hot bleed air coming from the engine is used to anti-ice the wing leading edges and engine intake cowls. Electrical power is used to anti-ice the windshields, side windows, air data probes, and sensors. Electrical windshield wipers provide rain removal for the pilot and copilot's windshields.

The aircraft is equipped with an ice detection system alerting the flight crew to impending icing conditions. A bleed air leak detection system monitors the bleed air ducting for leaks and over temperatures. The wing anti-ice system is divided into identical left and right systems. This ensures that wing anti-icing is maintained in both systems. The engine cowl anti-ice system is used to prevent ice formation on the engine's intake LE. This is done by using hot engine bleed air to heat the LE surface. The hot bleed air is supplied to the intake LE through respective L/R cowl anti-ice shut-off valves. Figure 106 illustrates LE de-icing components. Windshield and side window anti-icing is



achieved by electrically heating the windshield and side windows. The windshield wiper system is designed to remove rain and/or snow from the pilot and co-pilot's windshields at speeds up to 250 knots [81].

16 Performance Analysis

In this section, performance analysis of the Chaka MRJ family is presented.

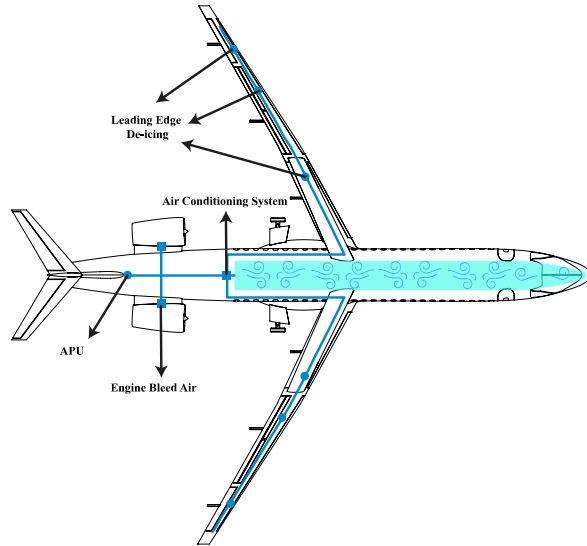


Figure 106- Pneumatic and Air conditioning systems of the Chaka

16.1 Payload Range Diagrams

In Figure 107, payload range diagrams of the Chaka-50 and -76, representing the maximum range achieved under different loading conditions, are shown and compared with their competitive aircraft. The first segment, from point A to point B, is the harmonic range, representing the longest range while having the maximum payload. Then, the range is extended to point C by trading payload for fuel. After the maximum fuel volume is reached at point C, the payload will be decreased to its minimum operating amount at point D. This minimum operational weight consists of only a pilot, the trapped fuel and oil, and the reserve fuel. The reserve fuel is capable of delivering 45 minutes of loitering flight or a 100 nmi diverted flight to an alternate airport. The range at point D is the maximum ferry range. Equation 11 is used in this regard [82].

$$\text{Equation 11: } R = \left(\frac{V}{T_{SFC}}\right)_{cruise} \cdot \left(\frac{L}{D}\right)_{cruise} \cdot \ln\left(\frac{W_1}{W_2}\right)$$

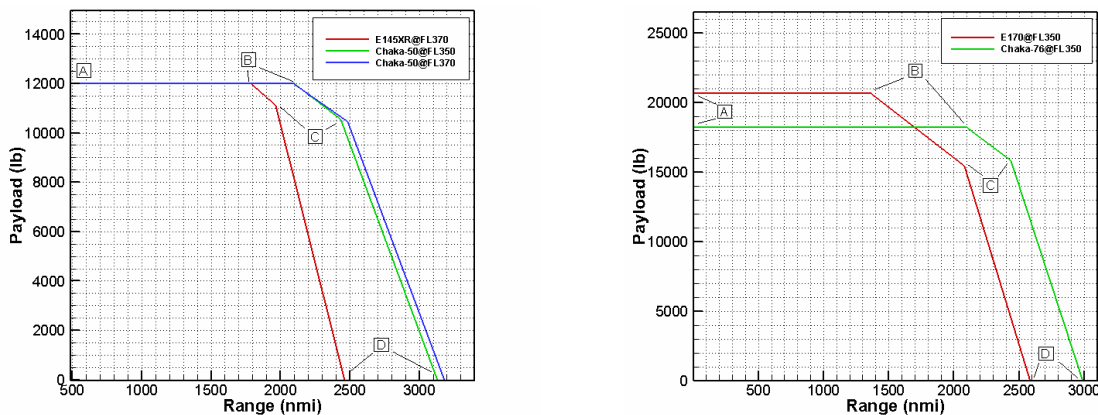


Figure 107- Comparison between payload range diagrams of the Chaka-50 and E145 (left), and also Chaka-76 and E170 (right)



16.2 Flight Envelope

In Figure 108, flight envelope diagrams of the Chaka-50 and -76 are shown. Using Saarlás formulations [83], the performance team has depicted the flight envelope at different load factors, with the service ceiling of the aircraft shown as the green line. In the diagrams, the right limiting line represents the maximum dynamic pressure and structural limit; the left limiting line represents the stall limit; and the upper limiting line represents the thrust limit. It is worthwhile mentioning that the orange region denotes cruising speed at maximum L/D .

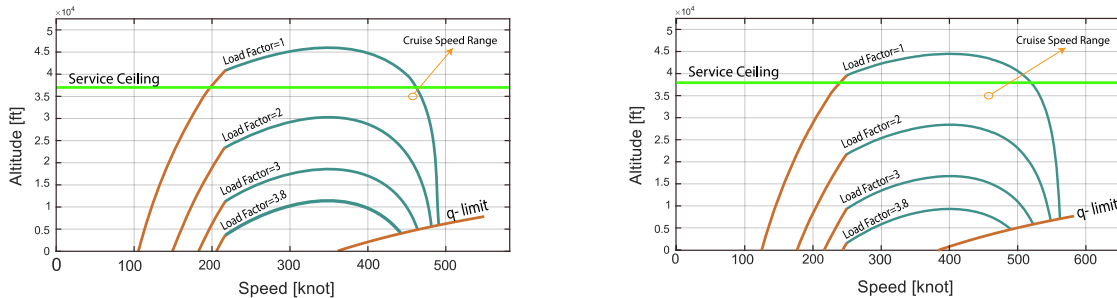


Figure 108- Flight envelope diagrams for the Chaka-50 (Left) and Chaka-76 (Right)

16.3 Take-off and Landing Performance

In accordance with the RFP’s requirements, take-off and landing field lengths must be less than 4,000 and 6,000 feet over a 50 ft obstacle, for the 50-seat and 76-seat airplanes, respectively, to a runway with dry pavement (sea level ISA+18°Fday). Table 66 provides an overview of the take-off and landing field lengths for the Chaka MRJ family at both sea level ISA+18°F day and FL50 ISA+18°F conditions. The calculations are carried out using [84].

Figure 109 and 110 illustrate take-off and landing field lengths with respect to aircraft’s weight, at different runway elevations, for the Chaka-50 and -76, respectively.

Table 66- Required take-off and landing field lengths for the Chaka MRJ family

Aircraft	Sea Level ISA + 18°F		FL50 ISA + 18°F	
	Take-off	Landing	Take-off	Landing
Chaka-50	3721.6 ft	3769.4 ft	3824.8 ft	3966.2 ft
Chaka-76	5064.2 ft	5209.7 ft	5150.7 ft	5588.5 ft

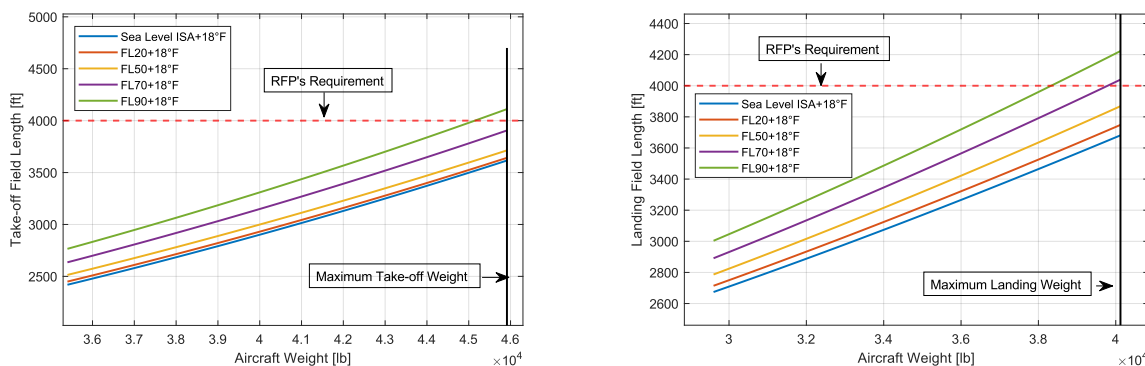


Figure 109- Take-off (left) and landing (right) field lengths with respect to aircraft’s weight for the Chaka-50 at different altitudes

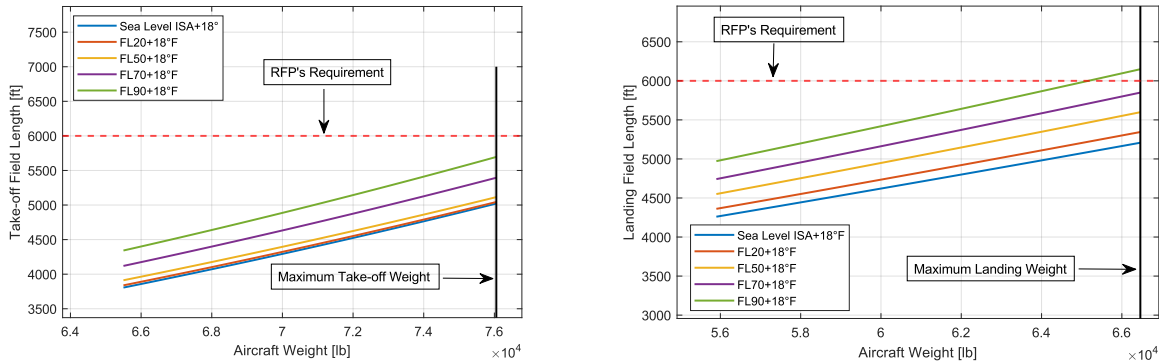


Figure 110- Take-off (left) and landing (right) field lengths with respect to aircraft's weight for the Chaka-76 at different altitudes

16.4 Rate of Climb and Ceiling

Utilizing Sadraey's aircraft performance formulations [85], like the ones shown in Equation 12 and Equation 13, the performance team iteratively calculated the ROC through a range of AOAs and ceilings.

$$\text{Equation 12: } \gamma = \sin^{-1} \left(\frac{T-D}{W} \right)$$

$$\text{Equation 13: } ROC_{max} = V_{ROC} \cdot \sin(\gamma)$$

In accordance with the calculations carried out, Figure 111 shows that, for both the Chaka-50, absolute ceiling (ROC of 0 fpm), service ceiling (ROC of 100 fpm), and cruise ceiling (ROC of 300 fpm) are equal to 38,100, 37,000, and 35,200 ft, respectively. For the Chaka-76, the figures are 38150, 37120, and 35290 ft, respectively.

The RFP requires that the distance to climb up to initial cruising altitude be less than 200 nmi. Based upon calculations, the minimum and maximum climb angles at which the Chaka-50 and -76 are able to satisfy the aforementioned are 1.65 and 7 degrees, respectively. The climb gradients corresponding to the former and the latter are 2.8% and 12%, respectively, meeting the 14 CFR 25.121. Figure 111, in the following, demonstrates altitude versus maximum ROC change for the Chaka MRJ family, superimposed on which calculated absolute, service, and cruise ceilings of each aircraft are defined.

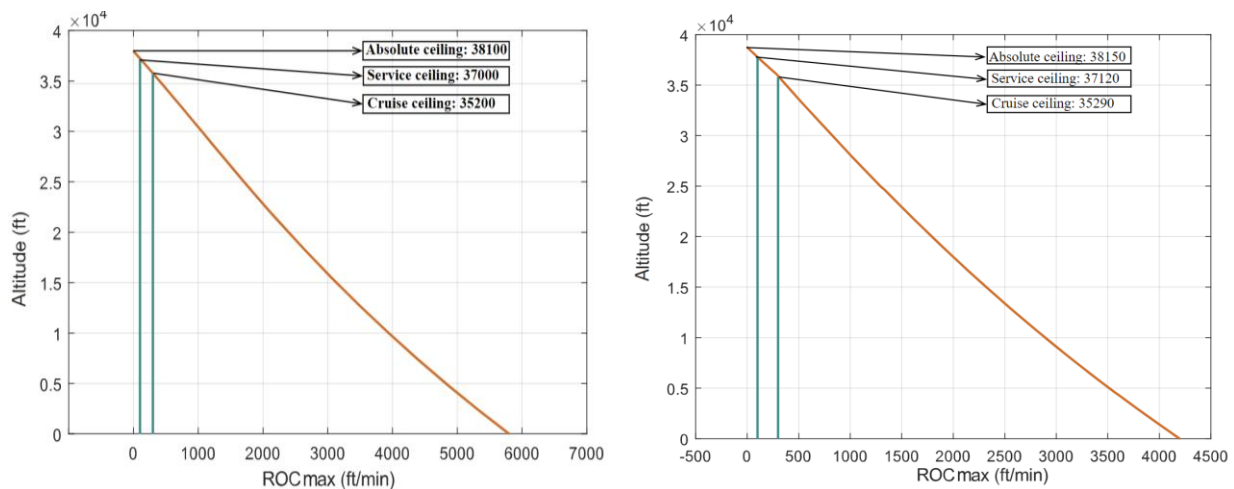


Figure 111- Altitude vs. maximum ROC for the Chaka-50 (left) and Chaka-76 (right)



Figure 112 provides details of climb-up distance versus climb angle, and it is plotted for the ROC of 2,200 fpm (36.7 ft/sec), horizontal speed of 301 ft/sec, and target ceiling of 35,000 ft, resulting in a 16-minute interval of climbing. As the figure implies, climb angles above 1.65 degrees are able to provide the “less than 200 nmi climb-up distance” requirement of RFP.

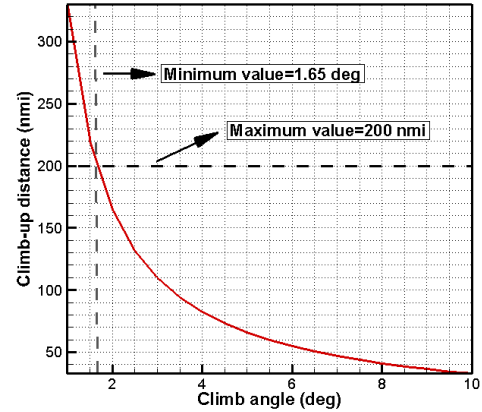


Figure 112- Climb-up distance vs. climb angle diagram for the Chaka

16.5 Performance Compliance with FAR Part 25

Lastly, it is time to run a final check on the Chaka aircraft’s performance compliance with FAR Part 25. As shown, all the performance requirements of FAR Part 25, going from sections 101 through 125, have been checked and met.

Table 67- Performance compliance of the Chaka MRJ family with FAR Part 25

FAR 25 Section	Part 25 Subject	Status
25.101	General	Met
25.103	Stall speed	Met
25.105	Take-off	Met
25.107	Take-off speeds	Met
25.109	Accelerate-stop distance	Met
25.111	Take-off path	Met
25.113	Take-off distance and run	Met
25.115	Take-off flight path	Met
25.117	Climb: General	Met
25.119	Landing Climb: All-engines-operating	Met
25.121	Landing Climb: One-engine-inoperative	Met
25.123	En route flight paths	Met
25.125	Landing	Met

17 Structures

This section outlines the structural layout and material accompanying their components’ parameters. Steps of structural design of Chaka MRJ family in systematic approach of aircraft design are illustrated in Figure 113.

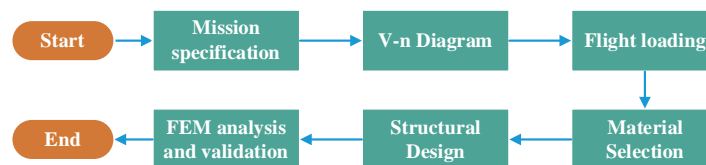


Figure 113- Road map of structural design



17.1 V-n Diagrams

As RFP stated, FAR 25 and Roskam are used to sketch the V-n diagrams for Chaka MRJ family as displayed in Figure 114. These graphs are plotted in sea level and maximum cruise weight. A safety factor of 1.5 is assumed for Chaka’s structure design in which its region is shown in the diagrams. The ultimate load points as a critical point for structural calculations are represented in the diagram.

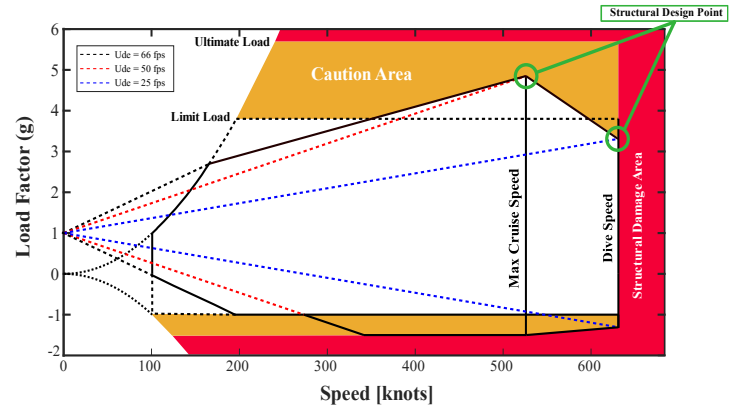


Figure 114- V-n Diagram of the Chaka-50 and -76

17.2 Material Selection

For decreasing fuel burn, one of the main strategies, used by the ShadX team, has been to decrease empty weight, which was achieved using composite and metal combination for the primary parts of the Chaka's structures. Table 68 represents these materials along with mechanical properties.

Table 68- Selected material utilized in the Chaka MRJ family

Material	Component	S _u (ksi)	Density (slug/ft ³)
2024 T4 Aluminum	Wing & fuselage skin	68.2	5.39
7075 Aluminum	Frame, longeron, and bulkhead	31.9	5.45
AISI 4340 Steel (Normalized)	Engine pylon, landing gear	161	15.23
S-Fiberglass	Nose radar cover, fuselage fairing, and flap fairing	696.1	4.84
Epoxy Carbon UD (395 GPa)	Wing rib & spar, empennage rib & spar	87.02	3.1
Countersunk rivet	Skin-longeron joints	--	--
5056 Aluminum rivet	Other joints	49.31	5.24
Composite metal foam	Wing leading edge	12.32	-
Sandwich panel	Cabin floor beams	12.03	-

Requiring less empty weight reduction, the Chaka-76 was designed using lower percentages of composite material compared to the Chaka-50, diminishing the cost of Chaka-76.

17.3 Structural Design

The fuselage structural design is done based on Roskam method [64] and the specifications are listed in Table 69.

Table 69- Fuselage structural specifications

Parameter	Chaka-50	Chaka-76	Recommended
Frame spacing (in)	20	20	18-22
Frame thickness (in)	3	3	-
Frame cross section shape	S	S	-
Longeron spacing (in)	11	11	6-12
Skin thickness (in)	0.07	0.07	-



The front and aft pressure bulkhead is manufactured with 7075 Aluminum. Wing spar and landing gear attachment to the fuselage are strengthened on frames 26 and 27. Due to the airfoil-shaped fuselage, the aft segment is strengthened where the tail junction is located.

In order to maintain commonality between Chaka-50 -76, only 14 frames were added to the Chaka-50's fuselage mid-section, and the rest of the aircraft's structure remained the same. The overall structure of Chaka MRJ family is presented in Figure 115.

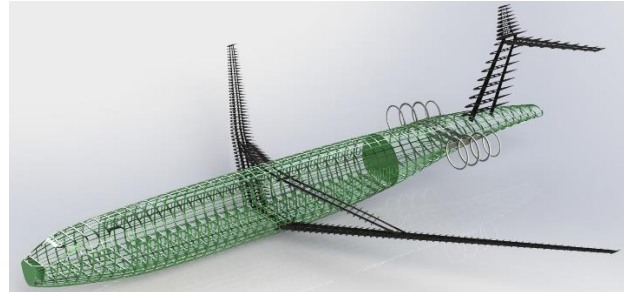


Figure 115- The overall structure of the Chaka MRJ family

For aerodynamic considerations, a high aspect ratio wing was selected. In order to minimize the amount of exerting bending moment on the wing root, a truss was designed in a way that its spars acting as an auxiliary linkage, bearing a share of the wing's lift force. In addition, three spars are designed along the wing to transmit tip load to wing root. Wing structural design parameters for Chaka MRJ family are illustrated in Table 70.

Table 70-Wing structure properties

	Parameter	Chaka-50	Chaka-76
Wing	Number of spars	3	3
	Front spar location	15% Chord	15% Chord
	Mid spar location	45% Chord	45% Chord
	Rear spar location	60% Chord	60% Chord
	Rib spacing	12 inches	14 inches
	Upper skin thickness	0.07 in	0.07 in
	Lower skin thickness	0.1 in	0.1 in
Truss	Number of spars	2	2
	Front spar location	20% Chord	20% Chord
	Rear spar location	65% Chord	65% Chord
	Rib spacing	14 in	14 in

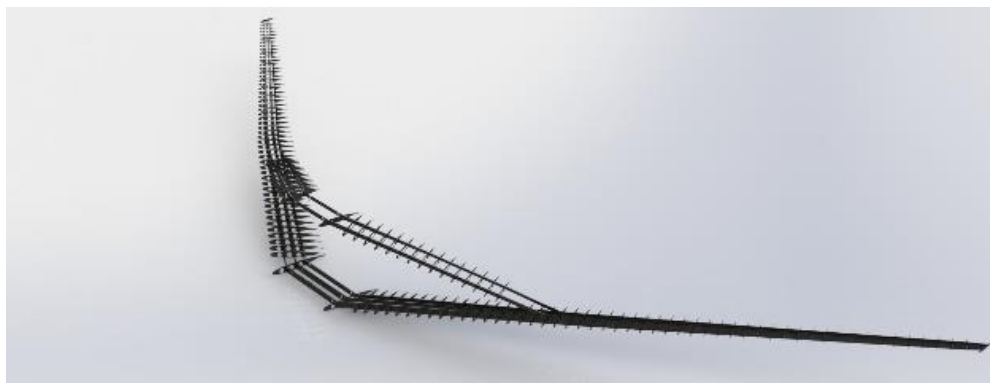


Figure 116- Wing structure of the Chaka MRJ family

According to the Soderburg criteria, by using high-truss configuration, the force distribution on the truss structure is compressive, which enhance fatigue strength and increase the structure lifetime.



Tail structural design was carried out the same as the wing's based on aerodynamic loads. Table 71 shows detail of ribs and spars.

Table 71- Ribs and spars details

Parameter	Chaka-50	Chaka-76	Recommended
Rib Spacing	15 in	15 in	15-30 inches
Front spar Location	25 % Chord	25 % Chord	15-25 % Chord
Rear spar Location	65 % Chord	65 % Chord	70-75 % Chord

Figure 117 shows tail structure of the Chaka MRJ family.

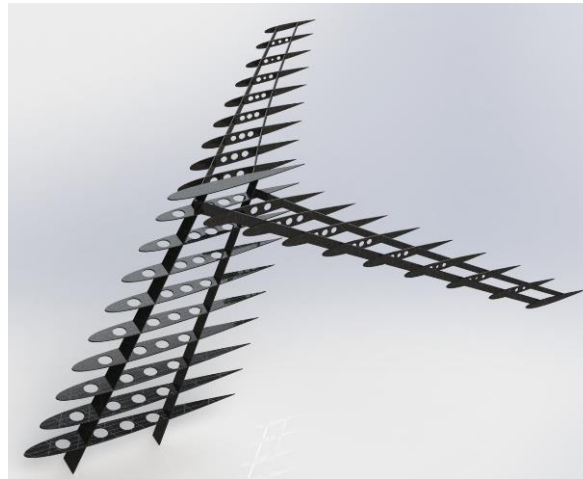
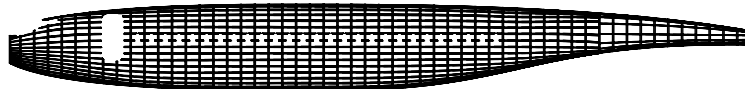


Figure 117- Tail structure of the Chaka MRJ family

In order to reduce production cost and maximum commonality between Chaka-50 and -76, part of the mid-section fuselage was designed in cylindrical cross-section with no curvature on the side edges to be extendable from 8'-4" in Chaka-50 to 32'-6" in Chaka-76. In more detailed view, only 14 frames would be added to Chaka-50 fuselage structure to obtain Chaka-76. Figure 118 shows structure transformation between family members.

Chaka-50



Chaka-76

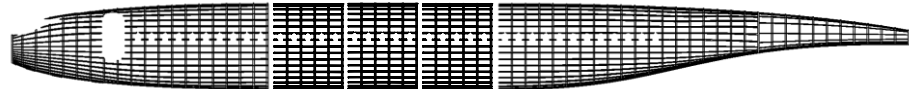
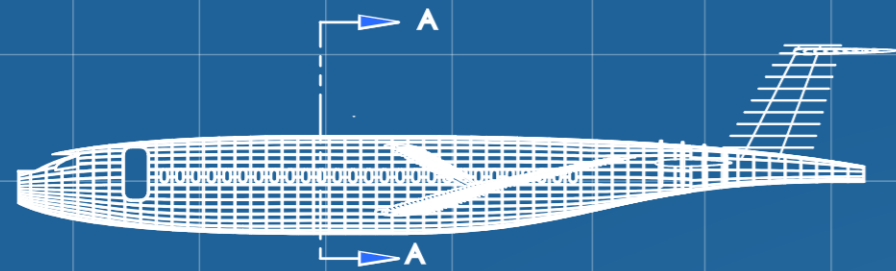
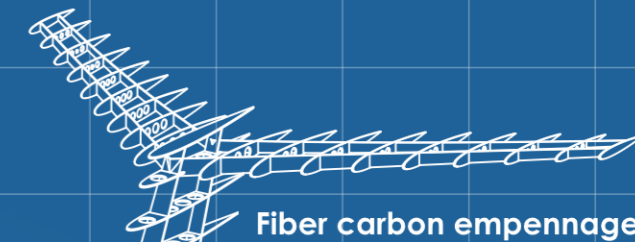


Figure 118-Fuselage structure of the Chaka MRJ family



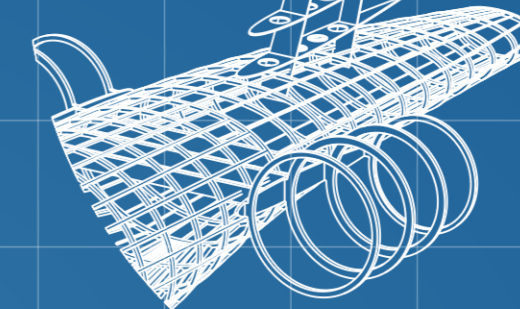
3 spars located @ 15% , 45% , 60% of wing chord



Fiber carbon empennage

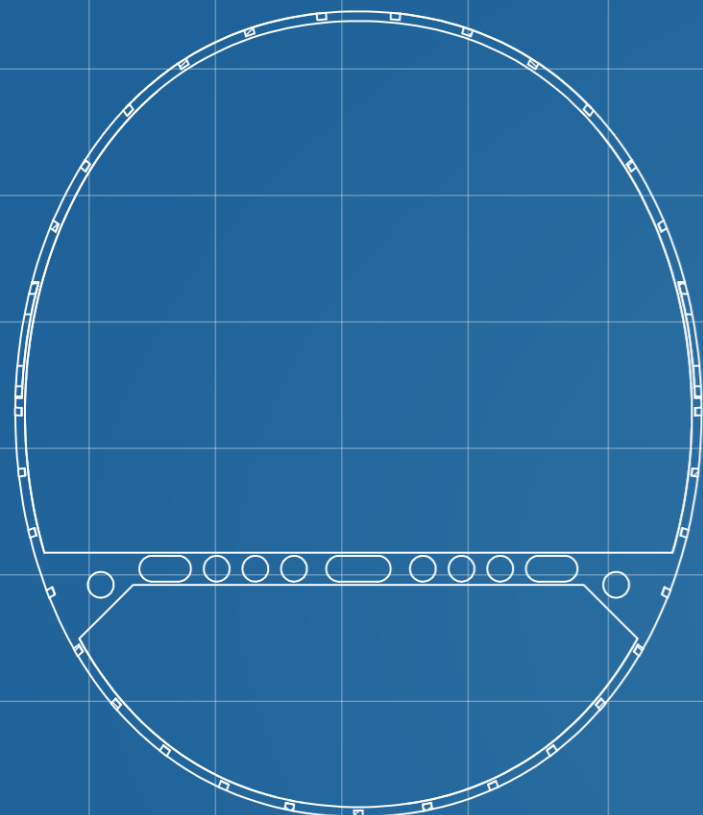
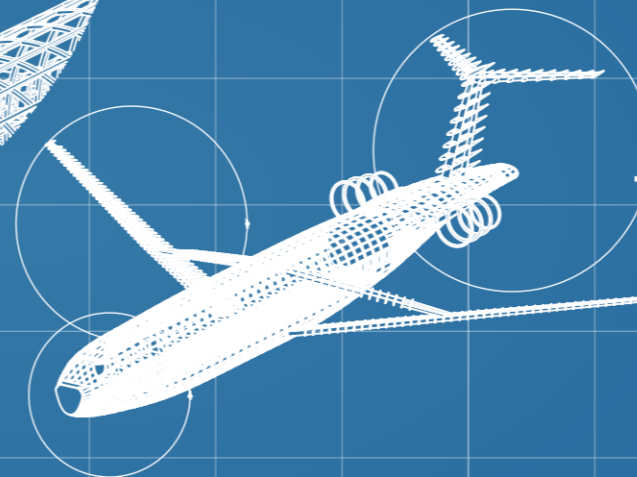
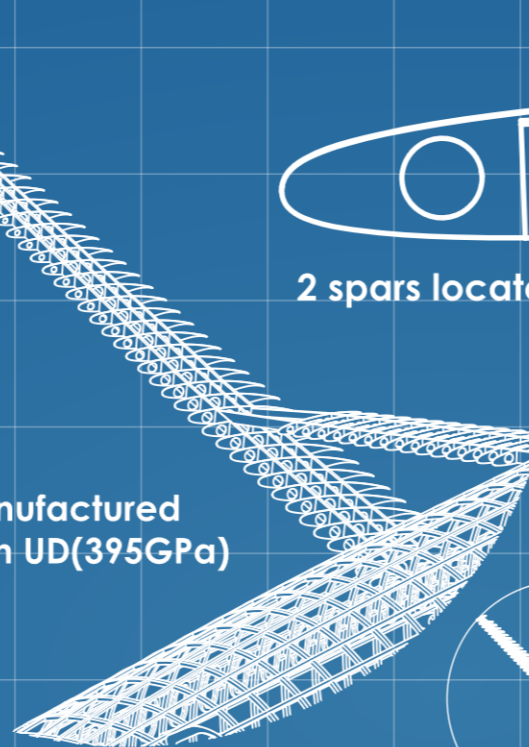


2 spars located @ 20% , 65% of truss chord



AISI 4340 normalized steel pylon

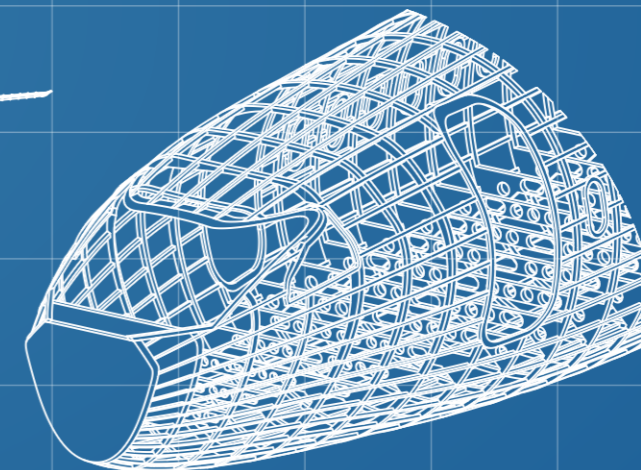
Ribs & spars manufactured from Epoxy carbon UD(395GPa)



SECTION A-A

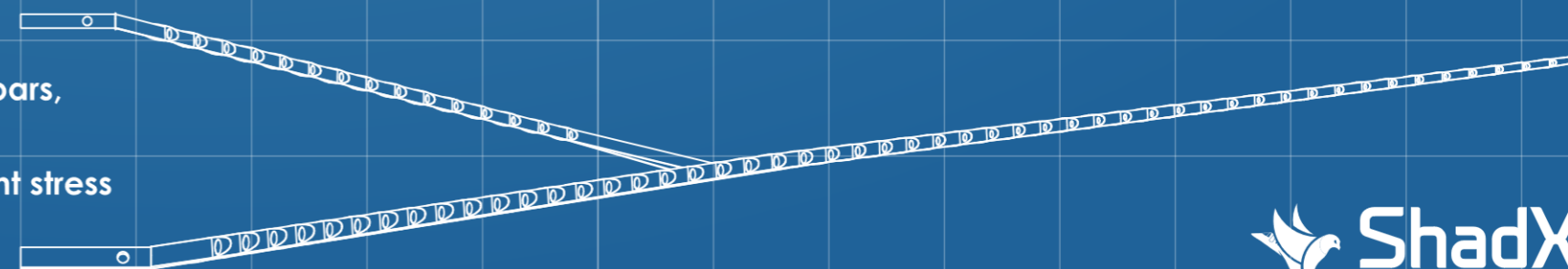
Sandwich panel floor beams
2024 T4 Al skin

34 x 11in spaced longerons
59 x 20in spaced frames(Chaka-50)
73 x 20in spaced frames(Chaka-76)

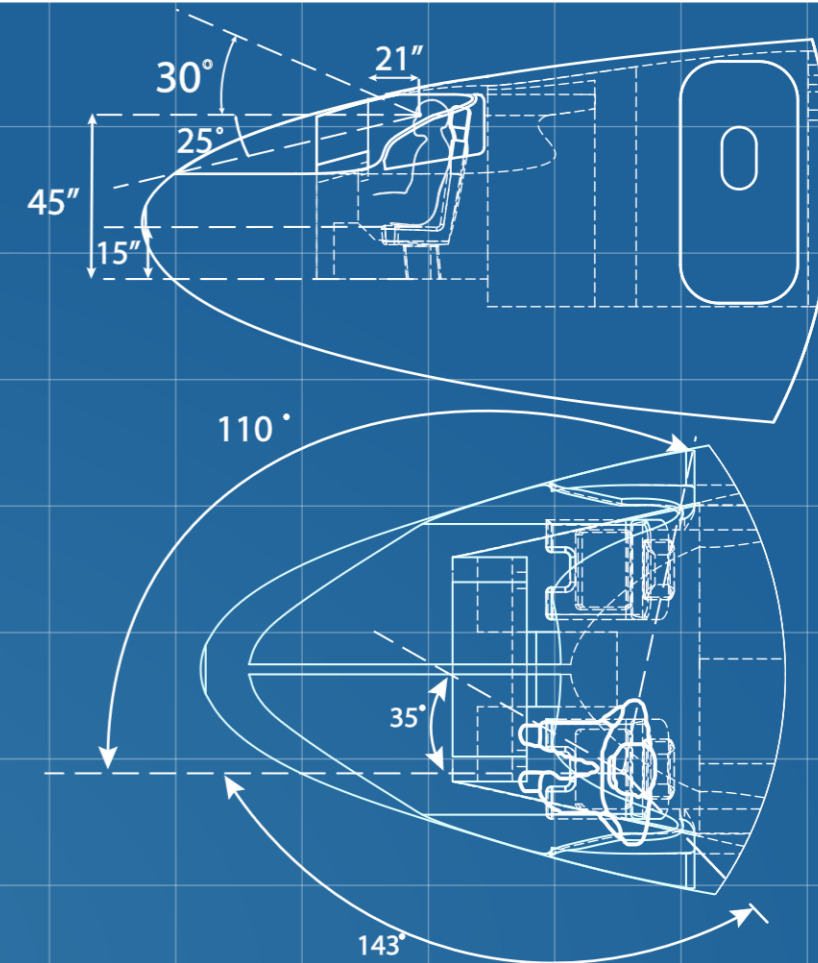
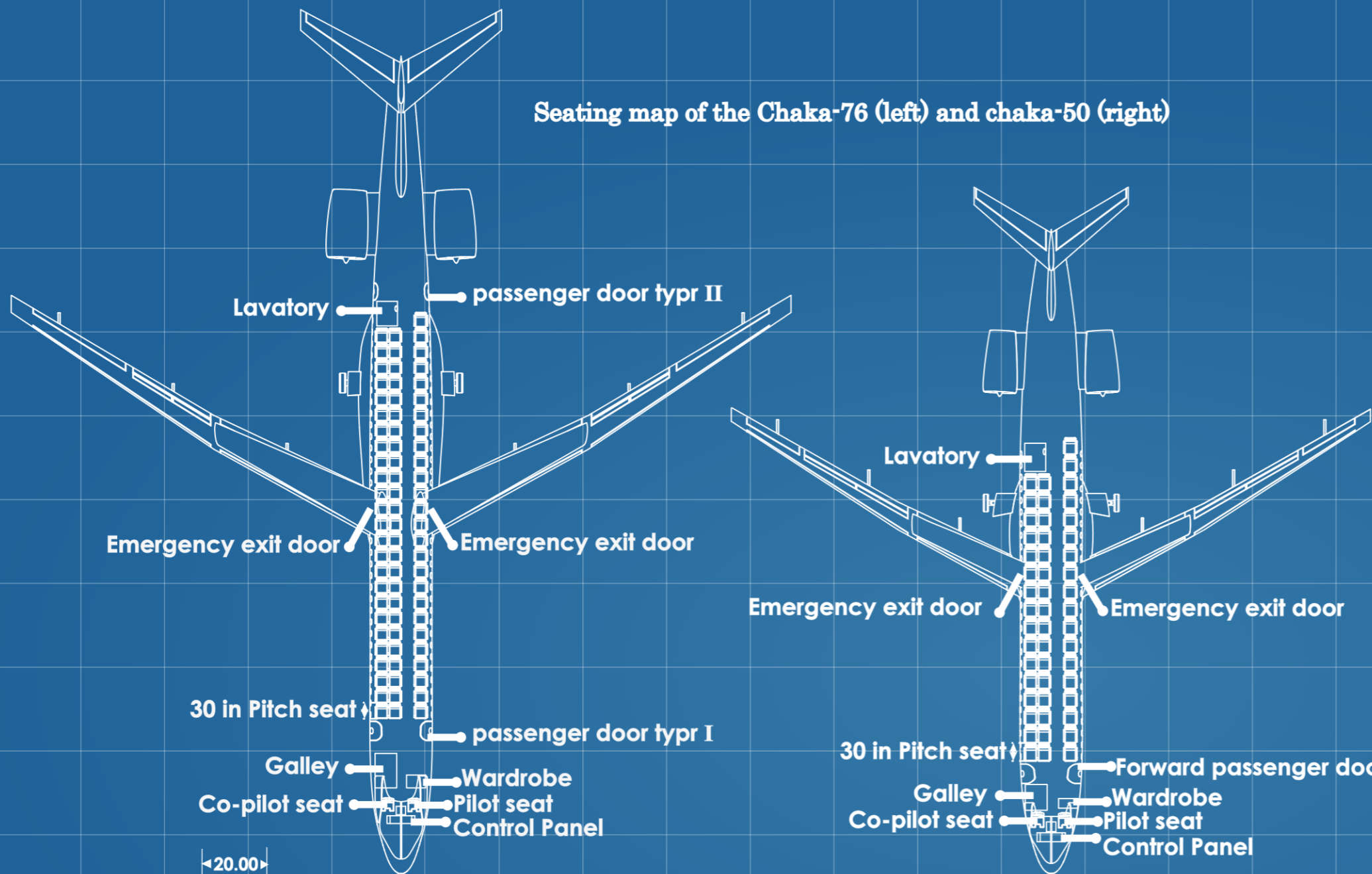


7075 Al bulkheads/frames/longeron

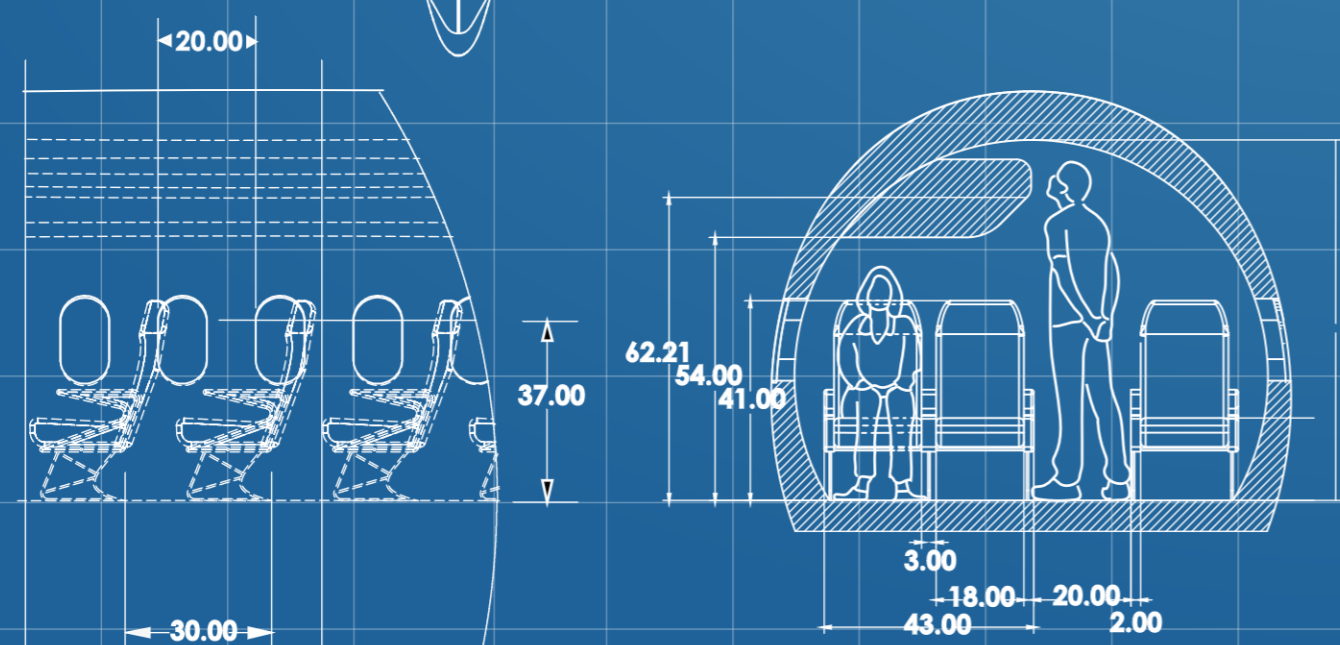
Truss spars joining wing's front & rear spars,
acting as auxiliary linkages,
dramatic decrease of bending moment stress



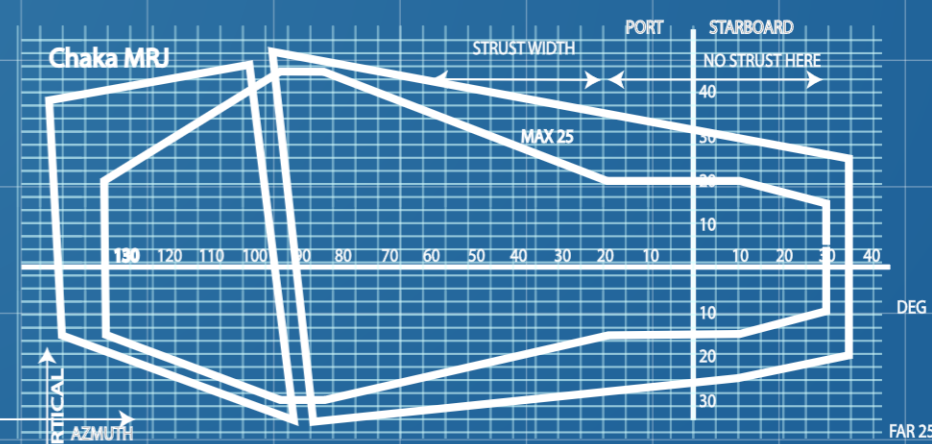
Seating map of the Chaka-76 (left) and chaka-50 (right)



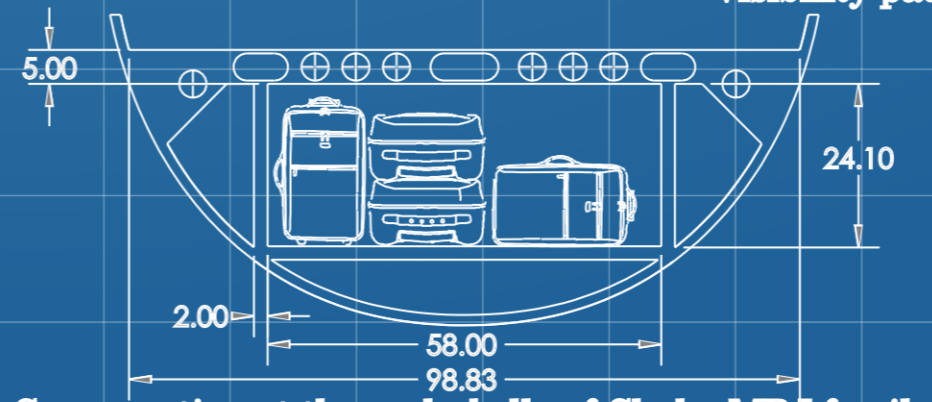
Cockpit, side view (up) and top view (down)



Seating arrangement, side view (left) and front view (right)



Visibility pattern for Chaka MRJ family



Cargo section at the underbelly of Chaka MRJ family



**CHAKA MRJ FAMILY
INTERIOR DESIGN**





19 Design Validations

In this section, exploited software tools are validated and verified. In terms of fluid and structural analyses, Ansys Fluent and structural has been utilized, respectively. Also, in terms of engine performance (i.e. thrust and SFC), GasTurb has been used, with the corresponding validations presented in the propulsion section. Figure 119 summarizes the numerical tools.

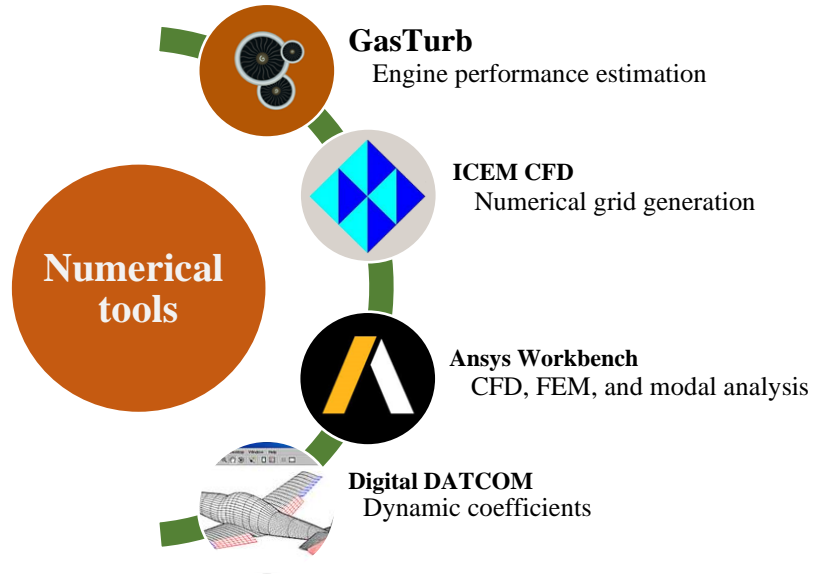


Figure 119- Summary of numerical tools

19.1 Validation of the CFD Tools

Regarding the exploitation of CFD methodology and Fluent software in different parts of the project, it is essential that the solvers in this regard be verified and validated. The flow around the aircraft has been simulated in two regimes, i.e. under Mach 0.3 (for the take-off and landing phases) and also Mach 0.8 (for the cruise phase). Each solver’s information is listed in Table 72. It is worthy to mention that the solver used for each regime has already been utilized successfully in multiple papers.

Table 72- Settings pertinent to the solvers used for CFD analyses carried out during the project

Setting	Low-subsonic flow (Mach <0.3)	High-subsonic flow (Mach 0.8)
Formulation	Pressure-based	Density-based
Turbulence model	K- ω SST	K- ω SST
Energy equation	Activated	Activated
Order of discretization	2 nd order	2 nd order
Viscosity model	Sutherland	Sutherland
Compressibility effects	Ideal incompressible flow	Ideal compressible gas

For the discretization, a hybrid grid was used, comprising a structured grid for the boundary layer region and an unstructured grid for the outside of the boundary layer region. With regard to flow simulation, adiabatic wall boundary condition was used to model the airplane’s surfaces, and fan boundary condition was used to incorporate engine effects. Figure 120 provides a schematic view of the boundary conditions used and also computational grid around the wing’s boundary layer region.

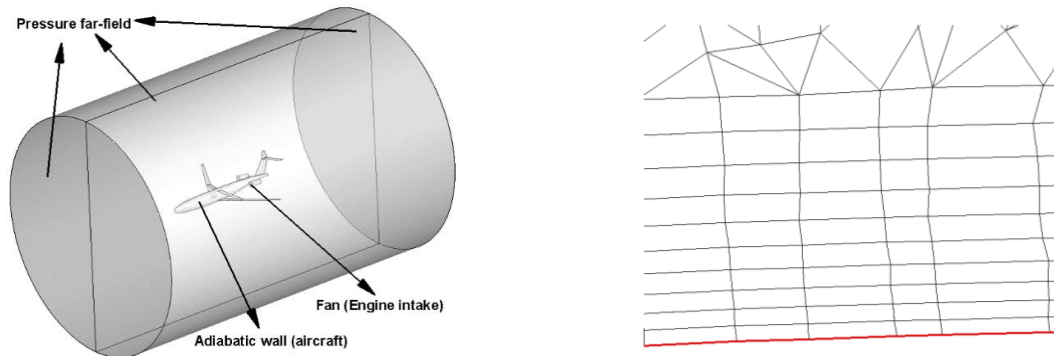


Figure 120- Views of the boundary conditions used to simulate the flow around the aircraft (left) and also the computational mesh used on the wing's boundary layer region (right)

Also, in order to investigate grid independency of the results, mesh study has been carried out. Figure 121 presents pressure contours of the Chaka-50 and its wing configuration, respectively.

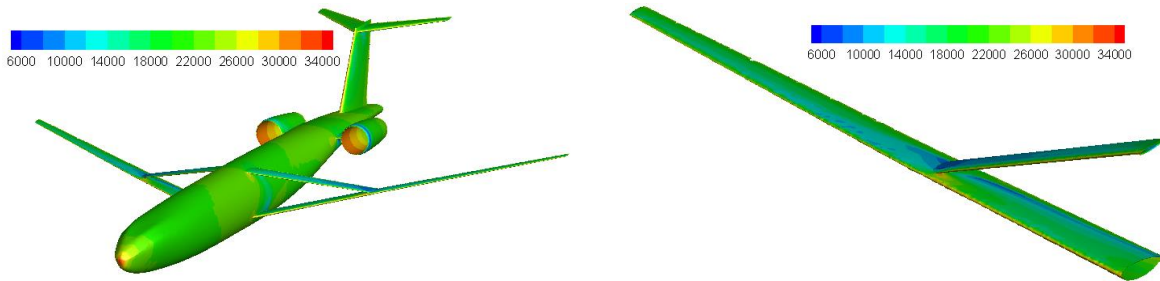


Figure 121-Static pressure contour on the surface of the Chaka-50 (left) and its wing configuration (right)

19.2 Validation of FEM Tools

In terms of structural analysis, Ansys Structural has been used, which is a customary tool with regard to analyzing tension in aerospace structures. Considering the structural sensitivity of the truss-braced wing configuration, it is mandatory to calculate its stress distribution and reliability to ensure structural integrity.

A view of the computational grid used for stress analysis on the wing is shown in Figure 122. Also, Figure 123 shows stress distribution of the wing configuration at cruise phase, verifying the structural design of the wing's configuration.



Figure 122- Grid on the wing's configuration

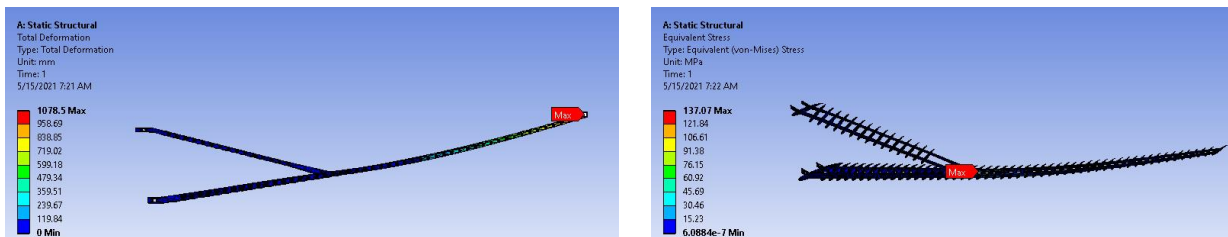


Figure 123- FEM analysis



19.3 Validation of Modal tools

Due to high aspect ratio used in the wing configuration of the Chaka family, it is crucial to study the natural frequencies of the wing and truss for the first three modes. To do so, Ansys modal tools is implemented. The numerical grid is similar to Figure 122 and “fixed displacement” boundary condition was used for wing and truss roots. Table 73 provides the first 3

natural frequencies of the Chaka-50’s wing configuration. Also, [the link](#) displays the videos of natural frequencies. Comparison proves that the resonance phenomena will not occur.

Table73 -Natural frequencies of Chaka-50’s wing configuration

Mode	Frequency (Hz)
1 st	1.57
2 nd	2.28
3 rd	4.48

20 Cost Analysis

In order to conduct cost analysis of the Chaka MRJ family, Roskam methodology has been utilized [86]. Since Chaka-50 and Chaka-76 are expected to enter into service in 2030 and 2031, respectively, having a gap period of only one year, they will be analyzed simultaneously.

It is worthy to mention that all of the costs and prices are reported based upon the 2030 US dollar, assuming a stable economic condition. Furthermore, wage rates and prices have been estimated utilizing the CPI and inflation rate forecasts [87]. It goes without saying that due to the current unstable economy caused by the Covid-19 crisis, cost estimation in terms of a program designed for the distant future (2030 to 2050) involves numerous complications.

20.1 Life Cycle Cost

Figure 124 provides an overview of the life cycle pertinent to Chaka MRJ family. According to the timeline, the RDT&E phase will get started in 2025. Immediately after the phase has been concluded, the manufacturing phase will start in 2030, and it will continue for the next twenty years. The delivery phase will be pursued shortly after the manufacturing phase, except for the first couple of months. Chaka MRJ family will reach its End of Life, when the disposal phase awaits it.

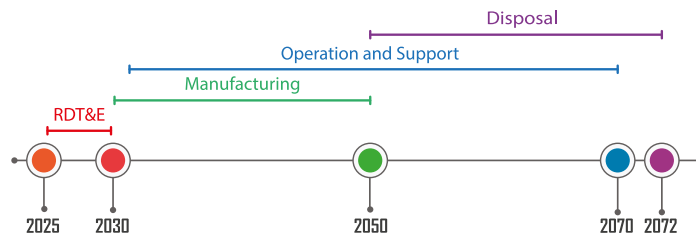


Figure 124- Life cycle of the Chaka MRJ family



20.2 RDT&E Cost

In this section, the RDT&E cost, comprised of non-recurring development costs of the airplane (i.e. engineering, FAA/EASA certification, production tooling, facilities, and labor), will be estimated. The RDT&E cost breakdown is presented in Figure 125.

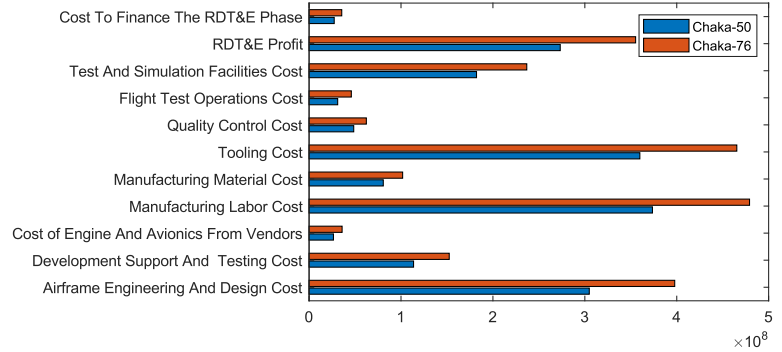


Figure 125- RDT&E cost breakdown of the Chaka MRJ family

Roskam’s cost estimation model [86] exploits judgment factors, as shown in Table 74, to determine the aircraft’s design characteristics. The difficulty factor of 1.8 has been assumed for the Chaka MRJ family owing to such unconventional design characteristics as having a supercritical airfoil-shaped fuselage and also a truss-braced wing.

Table 74- The judgment factors utilized in the Chaka MRJ family cost model

Factor	Domain	Determined value for Chaka-50	Determined value for Chaka-76
Difficulty factor	1 to 2	1.8	1.8
CAD capability	0.8 to 1.2	0.8	0.8

The material factor has been calculated for the Chaka-50 and -76. The details concerned with the material factor calculation are demonstrated in Table 75; the percentages pertaining to the aircraft’s structural materials are obtained from structure section.

Table 75- Material factor calculated for the Chaka MRJ family cost model

Material	F _{mat}	Percentage used in Chaka-50	Percentage used in Chaka-76
Aluminum 2024 T4	1.1	17%	26%
Aluminum 7075	1	27%	40%
Aluminum 5056	1.2	2%	3%
Fiber Glass	2.2	6%	6%
composite metal foam sandwich panels	2	1%	1%
AI-SI 4340 normalized steel	1.4	2%	2%
Epoxy Carbon UD (390GPa)	1.5	4%	4%
Epoxy Carbon UD (390GPa)	3	41%	18%
Total F _{mat}		1.941	1.502

20.3 Manufacturing and Acquisition Cost

In this section, the manufacturing and acquisition cost of the Chaka MRJ family will be estimated. As regards production and manufacturing phase, an essential parameter to be estimated is the production rate per month. In the market section of the proposal, it was indicated that, using deep learning, the target market has been simulated. The data obtained from the aforementioned have been utilized in order to estimate the market demand for RJs. Business plan details with regard to the Chaka MRJ family are illustrated in Table 76.



Table 76- The Chaka MRJ family business plan

Parameter	Chaka-50	Chaka-76
Number of airplanes built to production standards	1760	486
Airplane manufacturing rate per month	6.63	2.03

The manufacturing cost breakdown is presented in Figure 126. The acquisition cost and also the unit acquisition cost, also known as flyaway cost, for the Chaka-50 and -76 are listed in Table 77.

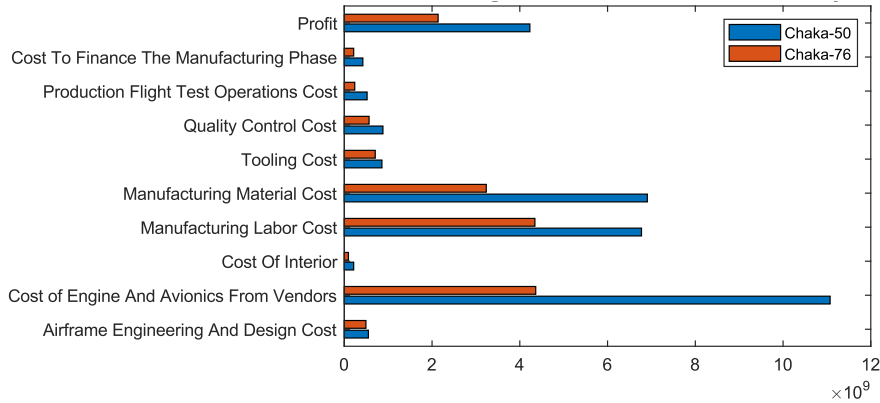


Figure 126- The manufacturing cost breakdown of the Chaka MRJ family program

Table 77- The acquisition and unit acquisition cost for the Chaka MRJ family

Parameter	Chaka-50	Chaka-76
Acquisition cost	32.426 B\$	16.391 B\$
Unit flyaway/acquisition cost	19.417 M\$	33.726 M\$

20.4 Aircraft Price Estimation

Following previous sections, in this section, the AEP and also the Aircraft Purchase Price will be calculated. The RFP required 15% marginal profit relative to the aggregate cost, applied in AEP calculations. Figure 127 shows the non-recurring cost, marginal cost, and the profit share; while Table 78 presents the AEP of the Chaka-50 and -76.

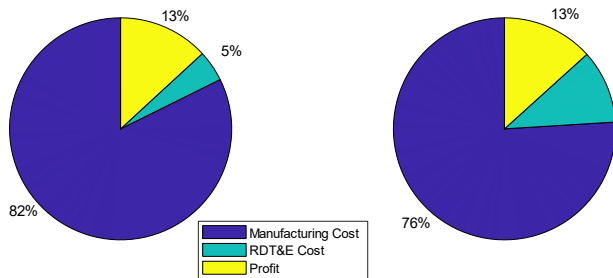


Figure 127- Aircraft Estimated Price Breakdown of the Chaka-50 (left) and -76 (right)

Table 78- AEP estimated for the Chaka MRJ family

Parameter	Chaka-50	Chaka-76
AEP	20.508 M\$	38.599 M\$

20.5 Operating Cost

Operational cost of Chaka as any other commercial airplane is divided into direct operating cost (DOC) and indirect operating cost (IOC). In this segment the main concern is to estimate the DOC of Chaka. Therefore, IOC is assumed to be equal to DOC as it usually is. The operating cost of the Chaka MRJ family is listed in Table 79.



Table 79- Operating cost assumed for 1,200 flight hours per year (in 2030 USD)

Parameter	Chaka-50	Chaka-76
DOC	4,667,750 \$	7,362,400 \$
IOC	4,667,750 \$	7,362,400 \$
Operating Cost	9,335,500 \$	14,724,800 \$

20.5.1 Direct Operating Cost

Direct operating cost is divided into five parts according to the Roskam cost model, as presented in Figure 128.

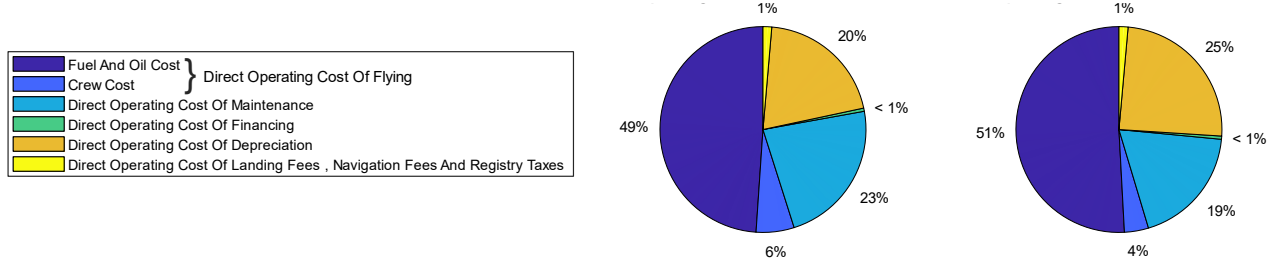


Figure 128- Direct operating cost of the Chaka-50 (left) and -76 (right)

20.5.1.1 Maintenance Cost

The maintenance cost is made up of labor and material costs of maintenance, as elaborated in Figure 129. Costs with regard to brakes and other consumable materials are considered in this part. Maintenance cost per flight is also shown for a 500 nmi flight in Table 80.

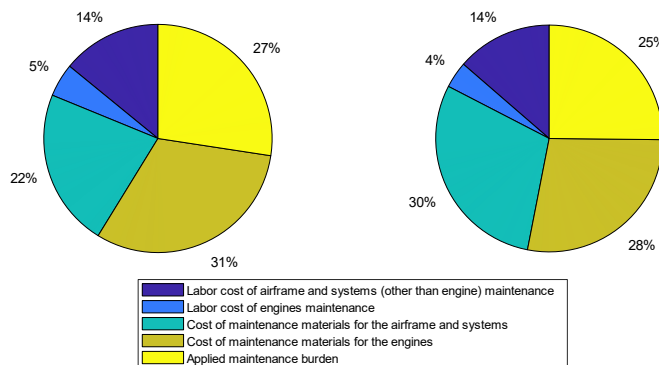


Figure 129- The maintenance cost of the Chaka-50 (left) and -76 (right)

Table 80- A 500 nmi flight maintenance cost for the Chaka MRJ family

Parameter	Chaka-50	Chaka-76
Maintenance cost	1,542.3 \$	2,018.7 \$

20.5.1.2 Direct Operating Cost of Flying

The direct operating cost of flying is comprised of the crew, fuel, and oil costs, as shown in Table 81.

Table 81- Operating cost of flying assumed for 1,200 flight hours per year (in 2030 USD)

Parameter	Chaka-50	Chaka-76
Fuel and oil	2,282,168 \$	3,741,914 \$
Flight crew	278,580 \$	278,580 \$

20.5.2 Fuel Cost

As shown in Figure 128, fuel cost plays the most important role in operating cost. Chaka, being a fuel-efficient aircraft, is a few steps ahead of its competitions in this era, but, still, fuel prices can affect the operating cost a lot.



For the fuel, there are the customary options such as the jet fuel, which is economically more beneficial. All the calculations in advance are based on jet fuel and the predicted price used for 2030 is obtained from [88].

Although - as previously discussed in propulsion system section - a green solution is also considered for fuel which is using 10% bio fuel (FT STK) as complementary for jet fuel. Although becoming green helps the environment, it will cost operators economically. The FT STK is approximately ten times more expensive than the jet fuel; therefore, fuel cost will rise by 90% [89].

20.6 Disposal Cost

Assuming a lifetime of around 20 years, the first airplanes of Chaka MRJ family will be out of service around 2050. By then, the significance of environmental considerations will have probably made disposal and recycling (D&R) a must. Parking will no longer be an option since it will only bring about a waste of space and resources. Therefore, in this section, disposal and recycling will be discussed.

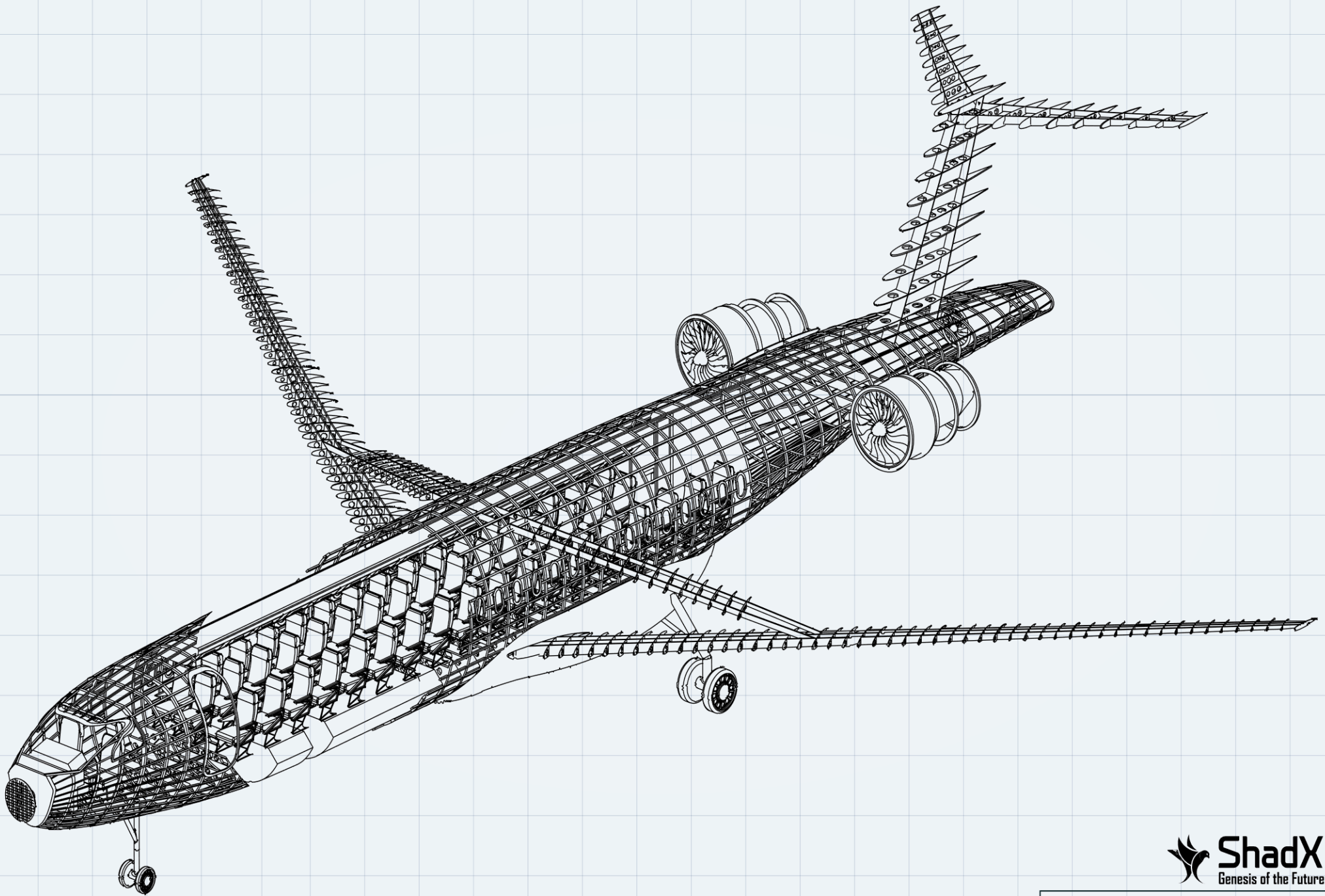
The most stimulative factors in terms of recycling are the following five: Firstly, aircraft going through their End-of-Life period contain components and materials possessing residual value, which should be restored. Secondly, secondhand materials obtained from recycling could be reused in aviation or used for other purposes instead of raw materials in order to save natural resources. Thirdly, recycling secondhand materials, such as carbon and aluminum, is also economically beneficial. It costs less, saves energy, and is environmentally advantageous, diminishing the amount of emissions into the water, air, and soil. Fourth, abatement in industrial waste which leads to the fifth aspect, requiring fewer landfills [90].

According to the literature [91] [92], disposal cost is around 10% of the aircraft’s purchase price or 1% of its total Life Cycle Cost. the disposal cost of the Chaka regional jet family is shown in Table 82.

Table 82- Disposal cost of total Chaka MRJ family program

Parameter	Chaka-50	Chaka-76
Disposal cost of total program	8.1527 B\$	3.7810 B\$

If the aircraft is in good shape, it could be resold, and, after being refurbished and recertified, it can be used as a freighter aircraft. In the disposal and recycling procedure, reusable components such as engines, landing gear, and avionics could be retained, after disassembly, and used in other compatible aircraft. Some components, such as some parts of the airframe, can be used for alternative purposes. After being dismantled, the materials will be separated and sorted, and the appropriate procedure, according to the type of material, will be applied [91].





REFERENCES

1. *PLANESPOTTERS.NET*. Available from: <https://www.planespotters.net/>.
2. *Embraer market outlook 2019*. 2019.
3. *Embraer market outlook 2020*. 2020.
4. Sezer, O.B., M.U. Gudelek, and A.M. Ozbayoglu, *Financial time series forecasting with deep learning: A systematic literature review: 2005–2019*. *Applied Soft Computing*, 2020. **90**: p. 106181.
5. Brownlee, J., *Deep learning for time series forecasting: predict the future with MLPs, CNNs and LSTMs in Python*. 2018: Machine Learning Mastery.
6. Gunn, S., *Nuclear propulsion—a historical perspective*. *Space Policy*, 2001. **17**(4): p. 291-298.
7. Eppinger, S.D. and T.R. Browning, *Design structure matrix methods and applications*. 2012: MIT press.
8. Shekar, B., R. Venkataram, and B. Satish, *Managing complexity in aircraft design using design structure matrix*. *Concurrent Engineering*, 2011. **19**(4): p. 283-294.
9. Gur, O., J.A. Schetz, and W.H. Mason, *Aerodynamic considerations in the design of truss-braced-wing aircraft*. *Journal of Aircraft*, 2011. **48**(3): p. 919-939.
10. Nickol, C. and L. Mccullers, *Hybrid wing body configuration system studies*. in *47th AIAA aerospace sciences meeting including the new horizons forum and aerospace exposition*. 2009.
11. Bhatia, M., et al. *Structural design of a truss braced wing: potential and challenges*. in *50th AIAA/ASME/ASCE/AHS/ASC Structures, Structural Dynamics, and Materials Conference 17th AIAA/ASME/AHS Adaptive Structures Conference 11th AIAA No.* 2009.
12. Bradley, M.K., C.K. Droney, and T.J. Allen, *Subsonic ultra green aircraft research. phase ii-volume i; truss braced wing design exploration*. 2015.
13. Wolkovitch, J., *The joined wing-An overview*. *Journal of Aircraft*, 1986. **23**(3): p. 161-178.
14. Wai, J., W. Herling, and D. Muilenburg, *Analysis of a joined-wing configuration*. in *32nd Aerospace Sciences Meeting and Exhibit*. 1994.
15. Werner-Westphal, C., W. Heinze, and P. Horst, *Multidisciplinary integrated preliminary design applied to unconventional aircraft configurations*. *Journal of aircraft*, 2008. **45**(2): p. 581-590.
16. Lange, R.H., *Review of unconventional aircraft design concepts*. *Journal of Aircraft*, 1988. **25**(5): p. 385-392.
17. Schmitt, D., *Challenges for unconventional transport aircraft configurations*. *Air & Space Europe*, 2001. **3**(3-4): p. 67-72.
18. Nangia, R., M. Palmer, and C. Tilmann, *Unconventional high aspect ratio joined-wing aircraft with aft-and forward-swept wing-tips*. in *41st Aerospace Sciences Meeting and Exhibit*. 2003.
19. Peifeng, L., et al., *Aerodynamic design methodology for blended wing body transport*. *Chinese Journal of Aeronautics*, 2012. **25**(4): p. 508-516.
20. *NASA TRL Calculator Microcode*.
21. Sadraey, M.H., *Aircraft design: A systems engineering approach*. 2012: John Wiley & Sons.
22. Roskam, J., *Airplane Design, Part I: Preliminary Sizing of Airplanes*. 1985.
23. *OAG: Flight Database & Statistics | Aviation Analytics*. Available from: <https://www.oag.com>.
24. IAW, *Unified Lecture # 2 : the Breguet Range Equation*. Massachusetts Institute of Technology, 2008: p. 1-12.
25. Accordi, I.A. and A.A.D. Paula, *Optimum Seat Abreast Configuration for an Regional Jet*. 2015: p. 1-11.
26. Roskam, J., *Airplane Design, Part II: Preliminary Configuration Design and Integration of the Propulsion System*. 1985.
27. Roux, É., *Turbofan and turbojet engines: Database handbook*. 2007.
28. Susan Bushell (Compiler), D.W.C., Paul Jackson (Editor), *IHS Jane's All the World's Aircraft 2015-2016: Development & Production*. 2015-2016.
29. Aviation, G., *CF34-3 turbofan engine*.
30. *Regional Aircraft*. Bussines & Commercial Aviation, 2006.
31. Embraer, *E170 AIRPORT PLANNING MANUAL*. 2019.
32. Embraer, *EMB145 AIRPORT PLANNING MANUAL*. 2019.
33. Raymer, D., *Aircraft design: a conceptual approach*. 2012: American Institute of Aeronautics and Astronautics, Inc.
34. Roskam, J., *Airplane Design: Preliminary configuration design and integration of the propulsion system*. 1985: DARcorporation.
35. Youngblood, J. and T. Talay, *Solar-powered airplane design for long-endurance, high-altitude flight*. in *2nd International Very Large Vehicles Conference*. 1982.
36. Ross, H. *Fly around the world with a solar powered airplane*. in *The 26th Congress of ICAS and 8th AIAA ATIO*. 2008.
37. Verstraete, D. [cited 2020 10/20]; Available from: <https://theconversation.com/climate-explained-why-dont-we-have-electric-aircraft-123910>.
38. Verstraete, D. *Why don't we have electric aircraft? ; Electric cars, trains, trams and boats already exist. That logically leads to the question: why are we not seeing large electric aircraft? And will we see them any time soon?]*. Available from: <https://sbi.sydney.edu.au/why-dont-we-have-electric-aircraft/>.



39. Nojoumi, H., I. Dincer, and G. Naterer, *Greenhouse gas emissions assessment of hydrogen and kerosene-fueled aircraft propulsion*. International journal of hydrogen energy, 2009. **34**(3): p. 1363-1369.
40. Silberhorn, D., et al., *Assessment of Hydrogen Fuel Tank Integration at Aircraft Level*. Deutsche Luft-und Raumfahrtkongress, 2019.
41. Tudosie, A.-N. *Turboshaft-type APU For Aircraft As Controlled Object*. in *International Conference Scientific Research And Education In The Air Force-AFASES 2016*. 2016.
42. Steiner, H.-J., et al. *Multi-disciplinary design and feasibility study of distributed propulsion systems*. in *28th International Congress of the Aeronautical Sciences*. 2012.
43. Kim, H.D., *Distributed propulsion vehicles*. 2010.
44. Feng, C., et al. *Reliability evaluation for distribution system based on probabilistic model checking*. in *2017 Second International Conference on Reliability Systems Engineering (ICRSE)*. 2017. IEEE.
45. Diakakis, S., *Sustainable Aviation Fuels*. 2019.
46. Klauber, A., Benn, A., Hardenbol, C., Schiller, C., Toussie, I., & Valk, M, *Innovative Funding for Sustainable Aviation Fuel at U.S. Airports: Explored at Seattle-Tacoma International Rocky Mountain Institute*. 2017.
47. *CF34-8E turbofan propulsion*. Cincinnati, Ohio. p. 2.
48. *PW1200G Engine*. p. 2.
49. *AE 3007 Series Engines*. 2015: Indianapolis, Indiana, United States of America. p. 15.
50. *CF34-8 series engines*. 2020: Lynn, Massachusetts, United States of America. p. 20.
51. *Climate data: North America*. 2019 [cited 2019; Available from: <https://en.tutiempo.net/climate/north-america.html>].
52. Harris, C.D., *NASA supercritical airfoils: A matrix of family-related airfoils*. 1990.
53. Whitcomb, R.T., *Review of NASA supercritical airfoils*. 1974.
54. Scholz, D. and S. Ciornei, *Mach number, relative thickness, sweep and lift coefficient of the wing—an empirical investigation of parameters and equations*. Hamburg: HAW Hamburg University of Applied Sciences, DLRK. Paper, 2005.
55. De Resende, O., *The evolution of the aerodynamic design tools and transport aircraft wings at Embraer*. Journal of the Brazilian Society of Mechanical Sciences and Engineering, 2004. **26**(4): p. 379-389.
56. Kafyeke, F., F. Pépin, and C. Kho. *Development of high-lift systems for the Bombardier CRJ-700*. in *ICAS 2002 Congress*. 2002.
57. Goraj, Z. and A. Sieradzki, *Influence of power unit configuration layout of a regional jet on performance and direct operating cost*. 2016, International Council of the Aeronautical Sciences.
58. *Airfoil Tools: Tools to search, compare and plot airfoils*. Available from: <http://airfoiltools.com/>.
59. Roskam, J., *Airplane Design. Part III: Layout Design of Cockpit, Fuselage, Wing, and Empennage: Cutaways and Inboard Profiles*. 1985.
60. Harrison, N.A., et al. *Development of an Efficient M= 0.80 Transonic Truss-Braced Wing Aircraft*. in *AIAA Scitech 2020 Forum*. 2020.
61. Droney, C., N. Harrison, and G. Gatlin. *Subsonic ultra-green aircraft research: transonic truss-braced wing technical maturation*. in *31st Congress of the International Council of the Aeronautical Sciences, Belo Horizon, Brazil*. 2018.
62. Torenbeek, E., *Synthesis of subsonic airplane design*. 1982.
63. Gudmundsson, S., *General aviation aircraft design: applied methods and procedures*. 2014: Oxford, UK : Butterworth-Heinemann.
64. Roskam, J., *Airplane Design*. 1985: DARcorporation.
65. Roskam, J., *Airplane Design. Part IV: Layout Design of Landing Gear and Systems*. 1985.
66. Stengel, R.F., *Flight Dynamics*. 2004.
67. McLean, D., *Aircraft flight control systems*. 1999.
68. Anderson, E., T. Fannin, and B. Nelson. *Levels of Aviation Autonomy*. in *2018 IEEE/AIAA 37th Digital Avionics Systems Conference (DASC)*. 2018. IEEE.
69. Sampedro, C., et al., *A fully-autonomous aerial robot for search and rescue applications in indoor environments using learning-based techniques*. Journal of Intelligent & Robotic Systems, 2019. **95**(2): p. 601-627.
70. *GAZEBO*. Available from: <http://gazebo.org/>.
71. Sutton, R.S. and A.G. Barto, *Reinforcement learning: An introduction*. 2018: MIT press.
72. *ROS*. Available from: <http://wiki.ros.org/ROS/Tutorials>.
73. Reynish, W. *Regional Jet Cockpits-Now and in the future*. 2004; Available from: <https://www.aviationtoday.com/2004/04/01/regional-jet-cockpits-now-and-in-the-future/>.
74. *Primus Epic*. 2021; Available from: <https://aerospace.honeywell.com/en/learn/products/cockpit-systems-and-displays/primus-epic>.
75. *Primus 1000 Integrated Avionics System*. 2021; Available from: <https://aerospace.honeywell.com/en/learn/products/cockpit-systems-and-displays/primus-1000>.
76. *Garmin G5000*. 2021; Available from: <https://buy.garmin.com/en-US/US/p/90821>.
77. *G5000® INTEGRATED FLIGHT DECK RETROFIT*. 2017; Available from: https://www8.garmin.com/aviation/brochures/G5000_Beechjet400A_Hawker400XP.pdf.



78. *Primus® Epic 2.0 Avionics System :The Advanced Flight Deck for the Dornier Seastar*. 2016; Available from: <https://aerospace.honeywell.com/content/dam/aero/en-us/documents/learn/products/cockpit-systems-and-displays/brochures/A60-1369-000-000-PrimusCockpitDornierSeastar-bro.pdf>.
79. Duncan, J.S., *Pilot's handbook of aeronautical knowledge*. 2016.
80. FlyEmbraer. *Emergency Information*. Instructions For Ground Fire Extinguishing And Rescue; Available from: https://www.flyembraer.com/irj/go/km/docs/download_center/Anonymous/Ergonomia/Home%20Page/Documents/ERJ145_Family_IGFER1136.pdf.
81. Bombardier. *CRJ Flight Crew Operational Manual*. ICE AND RAIN PROTECTION SYSTEM; Available from: https://www.smartcockpit.com/docs/CRJ-00_and_00-Ice_and_Rain_Protection.pdf.
82. Lan, E., and Roskam, J. , *Airplane Aerodynamics and Performance*. Roskam Aviation. 1980.
83. Saarlans, M., . *Aircraft Performance*.
84. Anderson, J.D., *Aircraft Performance and Design*. 1999.
85. Sadraey, M.H., *Aircraft Performance An Engineering Approach*. 2017.
86. Roskam, J., *Airplane design. Part VIII: Airplane Cost Estimation: Design, Development, Manufacturing And Operating*. 1985.
87. *US Inflation Forecast*.
88. *Jet Fuel Price Forecast*. Available from: https://www.eia.gov/outlooks/aeo/excel/aeotab_12.xlsx.
89. *Sustainable aviation fuels guide*. p. 66.
90. Chao, H., et al. *A model of aircraft retirement and acquisition decisions based on net present value calculations*. in *17th AIAA Aviation Technology, Integration, and Operations Conference*. 2017.
91. Zhao, X., W.J. Verhagen, and R. Curran, *Disposal and recycle economic assessment for aircraft and engine end of life solution evaluation*. Applied Sciences, 2020. **10**(2): p. 522.
92. Ribeiro, J.S. and J. de Oliveira Gomes, *Proposed framework for end-of-life aircraft recycling*. Procedia CIRP, 2015. **26**: p. 311-316.